5-2021

Visualization and Quantification of the Laser-Induced Art of TiO2 by Photoexcitation of Adsorbed Dyes

Daniela (Labadini) Graf Stillfried Barreto

VISUALIZATION AND QUANTIFICATION OF THE LASER-INDUCED ART OF TiO_2 BY PHOTOEXCITATION OF ADSORBED DYES

A Thesis Presented

by

Daniela (Labadini) Graf Stillfried Barreto

Submitted to the Office of Graduate Studies,
University of Massachusetts Boston,
in partial fulfillment of the requirements for the degree of

MASTER OF SCIENCE

May 2021

Chemistry Program

VISUALIZATION AND QUANTIFICATION OF THE LASER-INDUCED ART OF TiO_2 BY PHOTOEXCITATION OF ADSORBED DYES

A Thesis Presented

by

Daniela (Labadini) Graf Stillfried Barreto

Approved as to style and content by:

_____

Michelle Foster, Associate Professor
Chairperson of Committee

_____

Jonathan Rochford, Associate Professor
Member

_____

Jason Evans, Associate Professor
Member

_____

Jason Evans and Jonathan Rochford
Co-Graduate Program Directors
Chemistry Program

_____

Michelle Foster, Chair
Chemistry Department

ABSTRACT

VISUALIZATION AND QUANTIFICATION OF THE LASER-INDUCED ART OF TiO_2 BY PHOTOEXCITATION OF ADSORBED DYES

May 2021

Daniela (Labadini) Graf Stillfried Barreto
B.S., Universidad Simón Bolívar, Caracas, Venezuela
M.S., University of Massachusetts Boston

Directed by Professor Michelle Foster

The work presented in this thesis was published as:

Labadini, D.; Hafiz, S. S.; Huttunen, P. K.; Wolff, E. P.; Vasilakis, C.; Foster, M. Visualization and Quantification of the Laser-Induced ART of TiO2 by Photoexcitation of Adsorbed Dyes. Langmuir 2020, 36, 1651–1661.[1]

Dye-pretreated anatase TiO_2 films, commonly used as photoanodes in dye sensitized solar cells (DSSC), were utilized as a model system to investigate the laser-induced anatase to rutile phase transformation (ART), using N719 dye, N749 dye, D149 dye, and MC540 dye as photo-sensitizers. The visible lasers (532 and 785 nm) used for Raman spectroscopy were able to transform pure anatase into rutile at the laser spot when excitation of the dye sensitizer

caused an electron injection from the excited state of the dye molecule into the conduction band of the TiO_2. The three dyes with carboxylic acid anchor groups (N719, N749 and D149 dyes) experienced ART upon dye excitation; diffuse reflectance infrared Fourier transform (DRIFTS) and Raman spectra validated that these dyes were chemisorbed to the semiconductor surface. The MC540 dye with a sulfonic acid anchor group did not experience ART and the DRIFTS and Raman spectra were inconclusive about the chemisorption of this dye to the TiO_2. A TiO_2 calibration curve and percent rutile contour plots developed for this project are able to quantify the amount of rutile created at the surface of the samples. These improved chemical images which map rutile concentration help to visualize how ART propagates from the center of the laser spot to the surroundings. Factors such as visible light absorption and anchor groups that covalently bind to the semiconductor play a key role in effective laser induced ART.

DEDICATION

This work is dedicated to my baby Manuel, my husband Chris, and my family. Thank you for your endless support.

ACKNOWLEDGEMENTS

First and foremost, I would like to thank my advisor and mentor, Prof. Michelle "Shelley" Foster, for her endless support and guidance throughout all the years I have been at UMass Boston. She was able to teach me how to be an independent scientist, developing innovative projects, and focusing on the fundamental aspects of the research. Thank you, Shelley, for your constant motivation, patience, and support, that helped me grow as a better person.

I would also like to acknowledge my thesis committee: Prof. Jason Evans and Prof. Jonathan Rochford for their constant support ever since I started my graduate studies in the chemistry department, as well as for all the time and feedback throughout my Master's degree.

I would like to express my gratitude to all the present and past members of the Foster group including Sumeyra Gokalp, Paul Huttunen, Dr. Sabrina Hafiz, Dr. Maria Kipreos, Nelson Bello, and all the undergraduate students. You went from being "lab mates" to friends very quickly and I could not be happier to have been part of such an amazing group. We not only supported each other during the PhD/Masters, but also during the hard times in our personal life, and that is how we became like a family.

I especially want to thank my parents, Ada and Raimund, and my siblings, Gabriela and Ernesto, for their endless support and encouragement that gave me the motivation to keep going and finishing my Master's degree. Last but not least, I would like to acknowledge my husband and best friend, Chris, for his endless encouragement, love, and support throughout all these years that kept me sane and centered. Without him, this would not have been possible.

We now have a bigger challenge, which is welcoming our baby boy Manuel into the world and starting our journey as parents. I know that we will figure things out together, with much love and support from our families, and will raise him to be a great person, and maybe another scientist.

TABLE OF CONTENTS

CHAPTER PAGE

CHAPTER PAGE

LIST OF TABLES

Table Page

LIST OF FIGURES

Figure Page

Figure Page

LIST OF ABBREVIATIONS

Actual percent composition of anatase……x_a

Actual percent composition of rutile……x_r

Anatase relative integrated intensity……A_a

Anatase-rutile standards…….AR-standards

Anatase to rutile phase transformation……...…….ART

Anatase volume fraction……...……...V_a

Diffuse Reflectance Infrared Fourier Transform Spectroscopy……...……..DRIFTS

5-[[4-[4-(2,2-Diphenylethenyl)phenyl]-1,2,3-3a,4,8b-hexahydrocyclopent[b]indol-7-yl]methylene]-2-(3-ethyl-4-oxo-2-thioxo-5-thiazolidinylidene)-4-oxo-3-thiazolidineacetic acid……...……..D149 purple dye

Di-tetrabutylammonium cis-bis(isothiocyanato) bis(2,2′-bipyridyl-4,4′-dicarboxylato)ruthenium(II)…….N719 dye

Dye-sensitized solar cells……...DSSC

Pulsed Laser Deposition……...……PLD

Rutile relative integrated intensity……...A_r

Rutile volume fraction…….……V_r

5-[(3-sulfopropyl-2(3H)-benzoxazolylidine)-2-butenylidene]-1,2-dibutyl-2-thiobarbituric acid…….……..……..MC540 dye

Titanium Dioxide……...……TiO_2

Tris(N,N,N-tributyl-1-butanaminium)[[2,2″6′,2″-terpyridine]-4,4′,4″-tricarboxylato(3-)-N1,N1′,N1″]tris(thiocyanato-N)hydrogen ruthenate(4-)…..N749 black dye

CHAPTER 1

1. INTRODUCTION

1.1 Renewable energy and metal oxides

In the United States, non-renewable feedstocks, i.e., petroleum, natural gas, coal and nuclear, represent 90% of the country's energy source. Petroleum, being the largest, takes up 37% of the country's energy consumption. It is predicted, that by the year 2050, petroleum and its derivatives will still be utilized as a major source of energy in the United States. Renewable energy is expected to grow fast by 2050, including solar, wind and hydrothermal energy. Therefore, the need of making this industry more efficient and less expensive is highly attractive for researchers in the field (www.eia.gov/outlooks/aeo).

The desire to find an efficient and feasible energy alternative to fossil fuels has been the focus of much research, especially in the last decades.[2] Possible substitutions include photovoltaic devices, such as dye-sensitized solar cells (DSSC), which convert solar energy into electricity.[3–5] The main components of a DSSC are a photoanode, typically nanocrystalline semiconductor materials and a covalently bonded dye sensitizer to it, an electrolyte, and a counter electrode.[3–5] Conventional wisdom states that when the dye molecule gets excited by the sunlight, there should be a spontaneous electron injection from the excited state of the dye molecule into the conduction band of the semiconductor.[3–5]

The interest of using metal oxides nanoparticles as photocatalyst materials has increased in the past few decades. Metal oxides are readily available, stable, cost efficient and, the feature that makes them so attractive, their morphological and electrical

characteristics are tunable to the specifics of the final product.[6,7] Metal oxide nanoparticles are used as semiconductors, catalysts and photocatalysts, in DSSC, as biosensors, etc.… Advantages such as higher photocatalytic activity, mostly due to the high surface areas in nanoparticles, is appealing for making photocatalytic reactions simpler and more efficient, while achieving the same products with little to no solvent use and very few by-products as conventional processes.[6,7] Also, these nanoparticles can be easily recycled, maintaining their catalytic properties intact, compared to their bulk counterparts.[6,7]

1.2 TiO_2: the model metal oxide

Titanium dioxide (TiO_2) has been vastly investigated, as it is the preferred material as a catalyst and photocatalyst for the generation of hydrogen from water splitting, CO_2 reduction in presence of water, air and water purification, in DSSC, gas sensors and many other applications.[8–12] All these applications depend on the specific crystalline phase, morphology and chemical properties of the TiO_2 used, and fine tuning such properties for specific applications has become of great interest.[2] TiO_2 can be found as anatase, rutile and brookite crystalline phases.[2,8,11,12] The rutile phase of TiO_2 is thermodynamically more stable, but anatase is more photoactive.[8,12,13] Typically, a mixture of both anatase and rutile TiO_2 is used, due to the enhancement in the photocatalytic activity provided by the synergistic effect of combining both crystalline phases.[8,14] DeGussa P25, composed of 80% anatase and 20% rutile, is a commercially available mixture of these phases of TiO_2 and is being used in much of the documented research.[3,15]

1.3 ART: Anatase to rutile phase transformation

It is well known, that anatase transforms irreversibly into rutile at elevated temperatures; however, the transition temperature is highly affected by the nature of the sample, the synthesis method and impurities or defects found at the surface.[8,16] In most cases, anatase converts into rutile around 600°C in air, but in the literature, it has been reported that the transition temperature can be anywhere between 400 – 1200°C.[8,17] At these elevated temperatures, the metastable anatase phase collapses and readily converts into rutile, the thermodynamically more stable phase of TiO_2. The anatase to rutile phase transformation (ART) typically occurs by the coalescence of neighboring anatase grains, and the transformation into rutile highly depends on the initial nanoparticle size, chemical surroundings (defects and oxygen vacancies), impurities or dopants, as well as the reaction atmosphere.[16,18,19]

Several studies have shown that the phase change is dependent on the quality of the surface of the prepared TiO_2, where oxygen vacancies influence the ART by lowering the transition temperature to 600°C.[18,19] However, if the TiO_2 films are prepared on materials that might incorporate impurities in the TiO_2 lattice, the ART temperature can be affected, such as the study reported by Nakaruk *et al.*, where traces of silicon from the quartz surface upon which the TiO_2 films were prepared, elevated the ART temperature to 800-850°C.[20] Dopants, such as noble metals (Ag) and transition metals (Cu, Fe and Co), are known to lower the transition temperature and mixed anatase and rutile TiO_2 samples can be prepared without requiring such elevated temperatures.[21–25] In fact, doping TiO_2 with Ag nanoparticles lowered the ART temperature to 400°C, but if higher concentrations of Ag are incorporated,

AgCl clusters are formed, which in turn inhibit the ART.[26] Therefore, doping of TiO_2 requires the optimization of the concentration of the dopant, in order to achieve the desired characteristics of the thin films.

ART can also be achieved with the use of high-power lasers. Several studies report the transformation of pure anatase films into amorphous TiO_2, mixed anatase-rutile, and pure rutile by irradiating the sample with high-power lasers under vacuum or in an inert environment.[16,27,28] All studies attribute this ART to the destabilization of the TiO_2 surface, with its inherent native defects and oxygen vacancies, by the laser inducing the consequential coalescence of neighboring anatase grains into either amorphous or rutile TiO_2.[16,27,28] When the same samples were irradiated under ambient conditions in air, anatase did not transform into either amorphous or rutile TiO_2, even when irradiated with the highest laser power.[16,27,28] Additionally, amorphous TiO_2, typically prepared using the sol-gel method, is able to crystallize into anatase in air by irradiating the samples with high power lasers in the UV-visible range, as in the pulsed laser deposition (PLD) technique.[22,29–31] Nevertheless, during irradiation with high-power lasers, ART can be induced, as has been reported vastly in the literature.[21,22,29–31] Benavides *et al.* were able to control the specific crystalline phase of the TiO_2 thin film after irradiation with different laser powers, resulting in pure anatase, mixed anatase-rutile and pure rutile thin films, as the laser power increased the highest rutile concentration was achieved.[31]

1.4 Raman spectroscopy and ART

Raman spectroscopy using a Raman confocal microscope is a powerful technique for investigating both PLD and laser-induced ART since it has a high-power option for the laser to induce crystallization of amorphous TiO_2 films, as in PLD, while probing the results with a low-power setting of the laser.[22] One study using Raman spectroscopy reported the effect of doping TiO_2 samples with Fe and Al, showing that the Fe-doped TiO_2 samples irradiated by a ultraviolet laser (325 nm) induced ART, while the Al-doped TiO_2 samples inhibited ART.[24] These findings were compared with pure TiO_2 samples, where the ART was achieved after 5 hours of laser irradiation with the highest laser power of 20 mW. Doping TiO_2 samples with carbon nanotubes has also exhibited laser-induced ART.[24] The addition of dopants enables TiO_2 to absorb visible light and achieve ART.[17,21,25,32]

1.5 Surface chemistry of dye pretreated TiO_2

Dye molecules, bound to the TiO_2 surface, can also enable visible light absorbance in TiO_2 thin films, as seen in DSSC. In fact, Parussulo *et al*. reported that ART can be achieved using a Raman spectrometer on a P25 TiO_2 sample pretreated with the well-known N3-Ruthenium dye.[33] The Raman spectra verified that the ART propagated from the center of the laser spot, where there was a visible hole, to the surroundings, covering a few microns. Parussulo *et al*. conclude that the dye adsorbed on the TiO_2 thin film gets electronically excited by the visible laser, followed by an increase in temperature that decomposes the dye molecule and induces the ART in their P25 substrate.[33] However, this study did not report the temperature at the laser spot or how much rutile was created or its evolution from the center

of the hole to the surroundings. Alternatively, conventional wisdom in DSSC states that, when the dye molecule is excited by the sunlight, there is a spontaneous electron injection from the excited state of the dye molecule into the conduction band of the semiconductor.[3,4,34] This electron subsequently travels to the counter electrode of the DSSC, converting solar light into electricity. However, if just the dye-TiO_2 interface is probed with Raman spectroscopy, the electron injection, as expected from DSSC, can cause instability in the anatase TiO_2 and possibly induce a structural transformation. The unsatisfied dye molecule does not get regenerated by the redox mediator, like in a DSSC, and it most likely photo-decomposes.

1.6 Research Objective

To gain further insight into the laser-induced ART of dye-pretreated TiO_2 samples, popular Ruthenium dyes, N719 and N749 (black dye), and organic dyes, D149 (purple dye) and Merocyanine 540 (MC540) are used to attempt laser-induced ART on pure anatase TiO_2 samples. The Ruthenium dyes have been reported to experience a high efficiency of converting solar energy into electricity; however, due to the high cost and difficult purification processes of these Ruthenium dyes, recent research has focused on using metal-free organic dyes, which could provide competitive efficiencies for DSSC.[5,34–36] The binding method of these dyes to the TiO_2 surface, by either carboxylates (N719, N749 and D149 dyes)[5,37–39] or sulfonates (MC540 dye)[40,41] are probed with vibrational spectroscopy. Beyond exploring the ability of these dyes to induce ART, one highlight of this study is the development of a TiO_2 calibration curve, which allows quantification of the rutile created

from laser-induced ART. A few studies have attempted to quantify the rutile TiO_2 created from laser-induced ART using Raman spectroscopy;[24,25,42] however, those studies report results as rough estimates of the amount of rutile found at the surface. This study will quantify and allow visualization of the laser-induced ART of dye-pretreated TiO_2 films, by developing percent rutile contour plots, or calibrated Raman chemical mapping images.

CHAPTER 2

2. EXPERIMENTAL SECTION

2.1 Materials

Anatase TiO_2 with an average particle size of 20-30 nm was purchased from Inframat Advanced Material. Rutile TiO_2 with an average particle size of 30 nm was purchased from US Research Nanomaterial, Inc. The Di-tetrabutylammonium cis-bis(isothiocyanato) bis(2,2′-bipyridyl-4,4′-dicarboxylato)ruthenium(II) or N719 dye, the Tris(N,N,N-tributyl-1-butanaminium)[[2,2″6′,2″-terpyridine]-4,4′,4″-tricarboxylato(3-)-N1,N1′,N1″]tris(thiocyanato-N)hydrogen ruthenate(4-) or N749 black dye, the 5-[[4-[4-(2,2-Diphenylethenyl)phenyl]-1,2,3-3a,4,8b-hexahydrocyclopent[b]indol-7-yl]methylene]-2-(3-ethyl-4-oxo-2-thioxo-5-thiazolidinylidene)-4-oxo-3-thiazolidineacetic acid or D149 purple dye and the 5-[(3-sulfopropyl-2(3H)-benzoxazolylidine)-2-butenylidene]-1,2-dibutyl-2-thiobarbituric acid or MC540 dye were all purchased from Sigma-Aldrich, Inc. Ethanol (200 proof) was purchased from Pharmaco-Aaper. 18mm × 18mm borosilicate Corning® cover glass was purchased from Sigma-Aldrich, Inc. The Ti-nanoxide HT/SP, a titanium paste for UV-Vis experiments, was purchased from Solaronix. All the materials were used as received. The anatase and rutile TiO_2 crystallinity, as purchased, were confirmed with Raman spectroscopy and X-Ray powder diffraction and the corresponding spectra can be seen in figure 1.

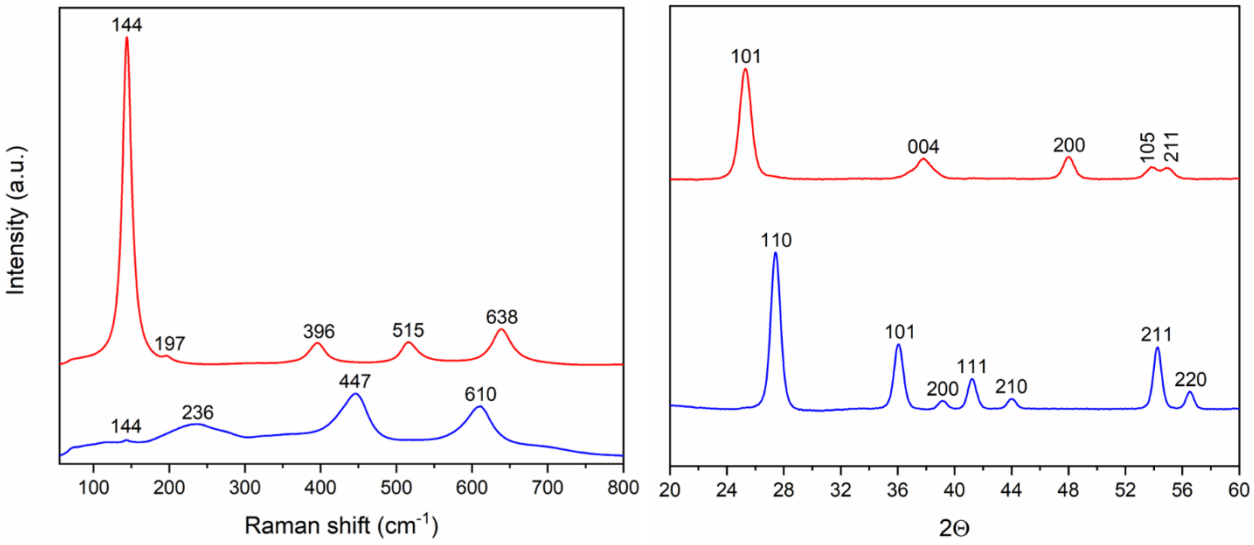

Figure 1. Raman and PXRD spectra of pure anatase (red) and rutile (blue) TiO_2 used for the dye-pretreated TiO_2 films. Both spectra clearly indicate pure anatase and rutile TiO_2.[18,19,43–45] The PXRD data was collected at room temperature using a dual source Bruker D8 Venture single-crystal diffraction system, IμS microfocus Copper source, equipped with a XRD2 plug-in for work with powders and APEX2 software.

2.2 Methods

2.2.1 TiO_2 films preparation

TiO_2 films were prepared by mixing 0.1 g of TiO_2 nanoparticles with enough spectroscopic grade ethanol in a mortar and pestle to form a homogeneous paste. The paste was smeared as a square on a borosilicate cover glass using a razor blade and Scotch® MagicTM tape. The TiO_2 film was then calcined for 30 minutes at 450°C, in order to remove the solvent. For the UV-Vis experiments, the same procedure was performed, but the Solaronix titanium paste, containing terpineol and organic binders, was used to create a

transparent film. Dye solutions were all $6x10^{-4}$ mM in ethanol. The TiO_2 films were submerged overnight in the dye solutions and rinsed three times with ethanol before any experimentation.

2.2.2 UV-Vis experiments

UV-Vis spectra of the dyes adsorbed onto the TiO_2 transparent film were collected on a Cary 5000 high performance UV-Vis-NIR spectrophotometer from Agilent Technologies using a double beam set up and a PbSmart detector, in the range of 350-900 nm, with a spectral band width of 2 nm, scanning for 0.1 s in every nanometer, and a scan rate of 600 nm/min.

2.2.3 DRIFTS experiments

Diffuse reflectance infrared Fourier transform (DRIFTS) spectra of the pure dyes on KBr and the dyes adsorbed onto the TiO_2 were collected using a liquid nitrogen cooled Nicolet iS 50 FT-IR spectrometer (128 scans, 2 cm^{-1} resolution, MCT-High D* detector) equipped with a Praying Mantis diffuse reflectance accessory (Harrick Scientific). The Praying Mantis was situated inside the sample compartment of the FTIR, and samples were purged with N_2 in the sample compartment for 20 minutes prior to collection of the spectra, in order to decrease the moisture in the sample.

2.2.4 Raman spectroscopy experiments

Raman spectra of pure TiO_2, anatase-rutile standards (AR-standards), pure dyes and dyes adsorbed onto the TiO_2 were collected with a Bruker SENTERRA confocal Raman Microscope in air using a green (532 nm) and a red (785 nm) laser, with 9-15 cm^{-1} resolution. A 2 mW laser power, 3 coadditions at 3 seconds each for the 532 nm laser was used to characterize the TiO_2 crystalline phases, as well as the dye features. To induce the ART with the 532 nm laser, a 1 second laser pulse of 20 mW, the highest available laser power, was used. For the 785 nm laser-induced ART, a 1 second laser pulse with 25 mW, the closest option available similar to the one used with the 532 nm laser, was used. For all experiments, the light was focused to a spot size of approximately 2 μm in diameter, using a 50x objective and a slit aperture of 50x1000 μm. Spectra were collected in the wavenumber range of 45-4450 cm^{-1}. Neutral density filters inside the Raman spectrometer were used to alter the laser power.

A thermocouple was used to check the temperature during the experiment. The laser was first focused on the thermocouple itself, and only a temperature change of about 15°C was seen. During the laser-induced ART experiment, the thermocouple was placed as near as possible to the laser spot on the dyed TiO_2 sample and a temperature change of only 5°C was seen, suggesting that the temperature increase caused by the photo-decomposition of the dye is minimal and thus not responsible for the phase change seen during the laser-induced ART.

2.3 Data Analysis

2.3.1 Curve fitting

AR-standards for an anatase and rutile TiO_2 calibration curve were prepared with pure anatase and rutile nanoparticles ranging from 0-100% rutile by weight ratio. Individual spectra for each AR-standard were fitted to a Voigt curve, a mixture between a Gaussian and a Lorentzian curve, which works well for fitting the asymmetric peaks of TiO_2.[46,47] Figure 2 shows a curve fitting example from a 50% rutile AR-standard. Two theoretical peaks were fit under each of the characteristic peaks used in this analysis, for anatase (515 cm^{-1}) and rutile (447 cm^{-1}), due to the asymmetric character of these features. The green curves in figure 2 represent the fit curves for the rutile peak, the blue curves for the anatase peak, and the orange curve is for another anatase peak at 396 cm^{-1}, which is not used for calibration. For each curve fitting, an R^2 value of at least 0.998 or higher was achieved.

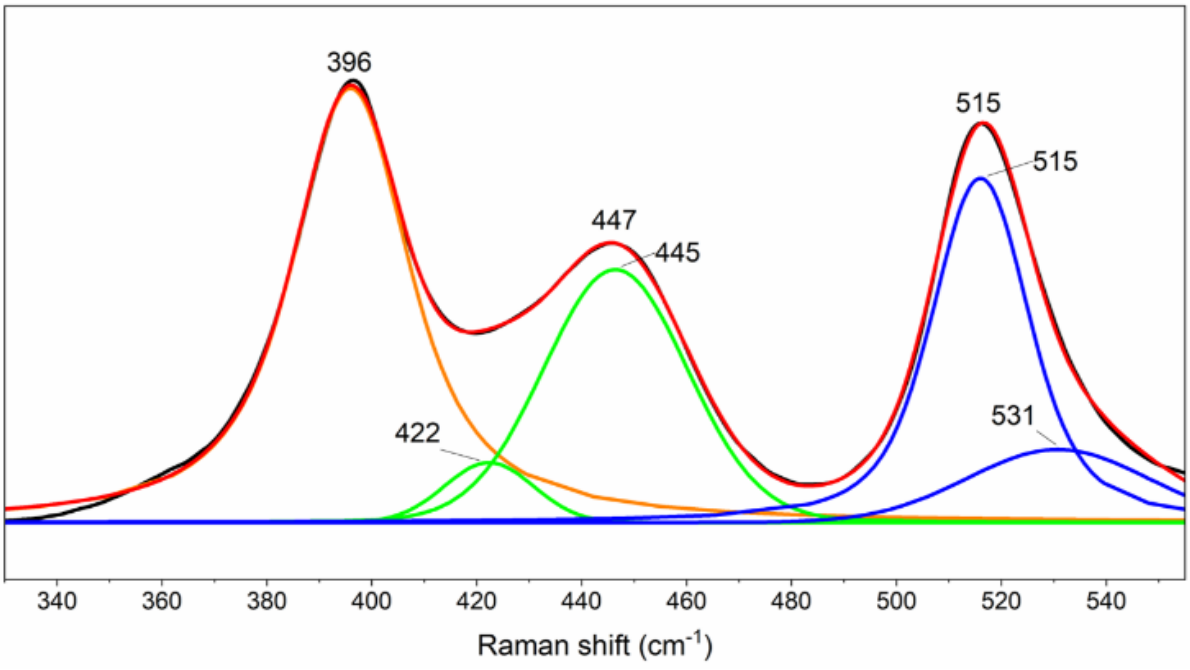

Figure 2. Raman curve fitting example for a 50% rutile AR-standard. The black curve is the experimental data, green curves are the fit peaks for the rutile 447 cm^{-1} peak, blue curves are the fit peaks for the anatase 515 cm^{-1} peak, the orange curve is the fit curve for the anatase 396 cm^{-1} peak, and the red curve is the result curve from the entire fitting.

The wavenumber range for the curve fitting includes both anatase peaks at 396 cm^{-1} and 515 cm^{-1} and the rutile peak at 447 cm^{-1}. This section of the spectrum was chosen for all curve fittings performed for this study. The anatase peak at 396 cm^{-1} was included in the curve fitting, due to the overlap between this peak and the 447 cm^{-1} rutile peak. The two peaks fit for each of the characteristic anatase (515 cm^{-1}) and rutile (447 cm^{-1}) were added together to form the relative integrated intensity for the respective anatase and rutile peaks. The following peak ratio formulas were considered for calculating either the anatase or the rutile volume fractions (V_a and V_r respectively) in each AR-standard:

$$V_a = \frac{A_a}{A_a + A_r} \quad \text{(Eq. 1)}$$

$$V_r = \frac{A_r}{A_a + A_r} \quad \text{(Eq. 2)}$$

where A_a and A_r represent the respective relative integrated intensity, i.e., the area under each of the anatase or rutile peaks.[48] Equations 1 and 2 assume that anatase and rutile TiO_2 are the only crystalline phases in the sample and their respective volume fractions add up to 1 ($V_a + V_r = 1$). The areas of the peaks fit for the rutile 447 cm^{-1} peak (green curves in figure 2) were added together to form the total relative integrated intensity for that rutile peak. The same was done for the anatase 515 cm^{-1} peak. Using equations 1 and 2, the volume fractions for each crystalline phase were obtained. For the example shown in figure 2, using this method, the volume fractions were found to be 0.44 for rutile and 0.56 for anatase. When all 16 of the 50% rutile AR spectra were analyzed, the average volume fractions were found to be 0.4995 for rutile and 0.5005 for anatase.

2.3.2 Calibration curve

Standard mixtures for an anatase and rutile TiO_2 calibration curve were prepared with pure anatase and rutile nanoparticles ranging from 0-100% rutile by weight ratio. Figure 3 shows the resulting Raman spectra of these AR-standard as the weight % of rutile is increased by increments of 10%.

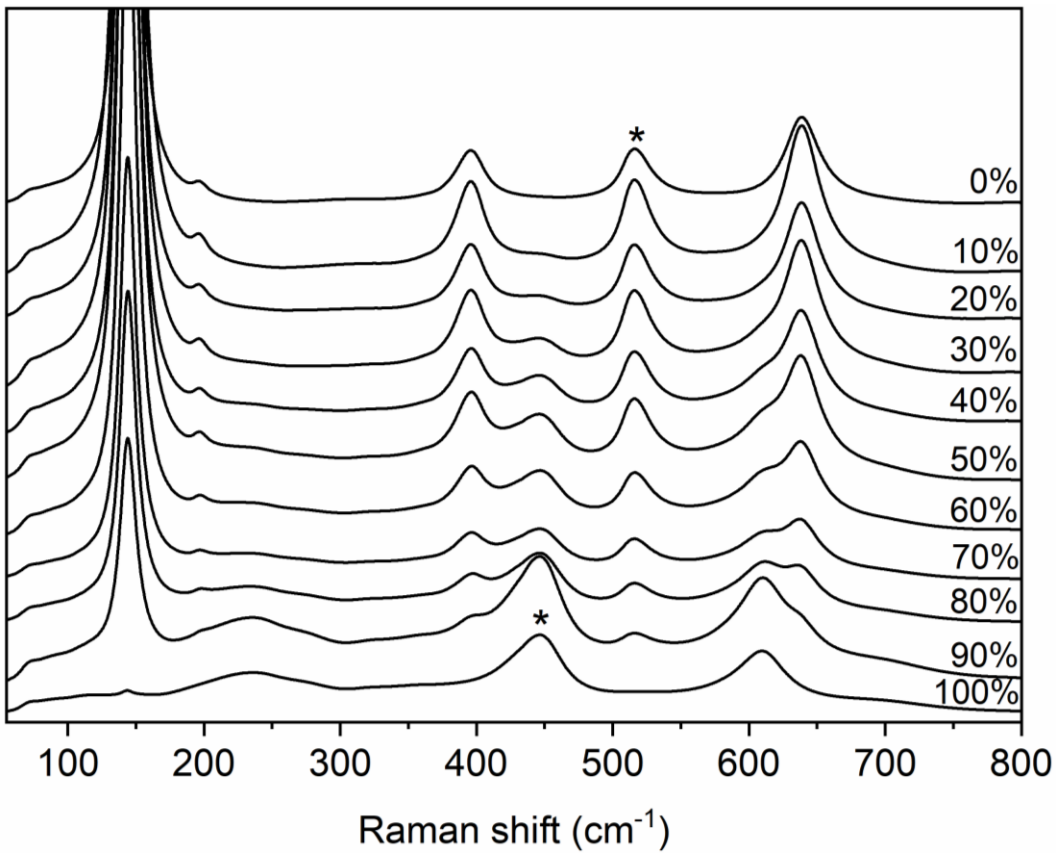

Figure 3. Average Raman spectra for each AR-standard. The average of 16 different spectra for each of the AR-standards were used for the anatase and rutile TiO_2 calibration curve. The number indicates percentages of rutile present in each AR-standard. The asterisks indicate the characteristic anatase (515 cm^{-1}) and rutile (447 cm^{-1}) peaks used for the analysis.

A quantitative analysis is possible since the anatase and rutile TiO_2 have very distinct Raman spectra and the isolated band intensities for each anatase and rutile peak are proportional to the respective concentration in the sample.[48] To calculate spectroscopically the concentration of anatase and rutile in one sample, specific and isolated peaks from each TiO_2 crystalline phase were considered and are marked with an asterisk in figure 3. For anatase the peak at 515 cm^{-1} and for rutile the peak at 447 cm^{-1} were chosen because those

peaks are the first to appear when either anatase or rutile are present in a sample at very low concentration (< 10%). The anatase peak at 144 cm^{-1}, being the most prominent anatase peak, could be an appropriate choice of peak to select for the calibration curve; however, the intensity trend does not illustrate the consistent growth expected as the anatase concentration increases.[49] Therefore, the anatase peak at 515 cm^{-1}, which is comparable in intensity with the other anatase peaks and even with the rutile peaks, better represents the actual percent composition of that crystalline phase in a sample using this methodology. Figure 3 illustrates the gradual development of each phase, i.e., as the intensity of the anatase peak at 515 cm^{-1} decreases, so does the concentration of anatase in the sample.

Raman spectra of the AR-standards were collected at sixteen points on the surface and the resulting spectra were averaged to provide each AR-standard spectrum presented in figure 3. Individual spectra for each AR-standard were fitted to a Voigt curve and the average relative integrated intensity and average volume fraction from this quantitative analysis for each AR-standard are listed in Table 1, and the results are plotted in the calibration curve shown in figure 4. The x-axis is the known concentration of rutile TiO_2 in each AR-standard, and the y-axis is the average volume fraction calculated. The error bars in each point in figure 4 are the standard deviations from the average volume fractions for each AR-standard.

Table 1. Calculated relative integrated intensities and volume fractions for the anatase and the rutile calibration curve.

% Rutile in AR-standard	Average rutile integrated intensity (A_r)	Average rutile volume fraction (V_r)	standard deviation of V_r	Average anatase integrated intensity (A_a)	Average anatase volume fraction (V_a)	standard deviation of V_a
100	264838.05	1	0	0	0	0
90	388205.01	0.9165	0.0175	35563.22	0.0835	0.0175
80	205083.71	0.8283	0.0250	42478.62	0.1717	0.0250
70	131315.73	0.6879	0.0380	60232.11	0.3121	0.0380
60	192239.39	0.5795	0.0378	141034.33	0.4205	0.0378
50	181040.41	0.4995	0.0410	181255.79	0.5005	0.0410
40	142979.73	0.3895	0.0193	224430.62	0.6105	0.0193
30	137833.11	0.3036	0.0108	315699.97	0.6964	0.0108
20	50334.64	0.1713	0.0352	242081.68	0.8287	0.0352
10	21025.15	0.0629	0.0075	314508.03	0.9372	0.0075
0	0	0	0	236183.89	1	0

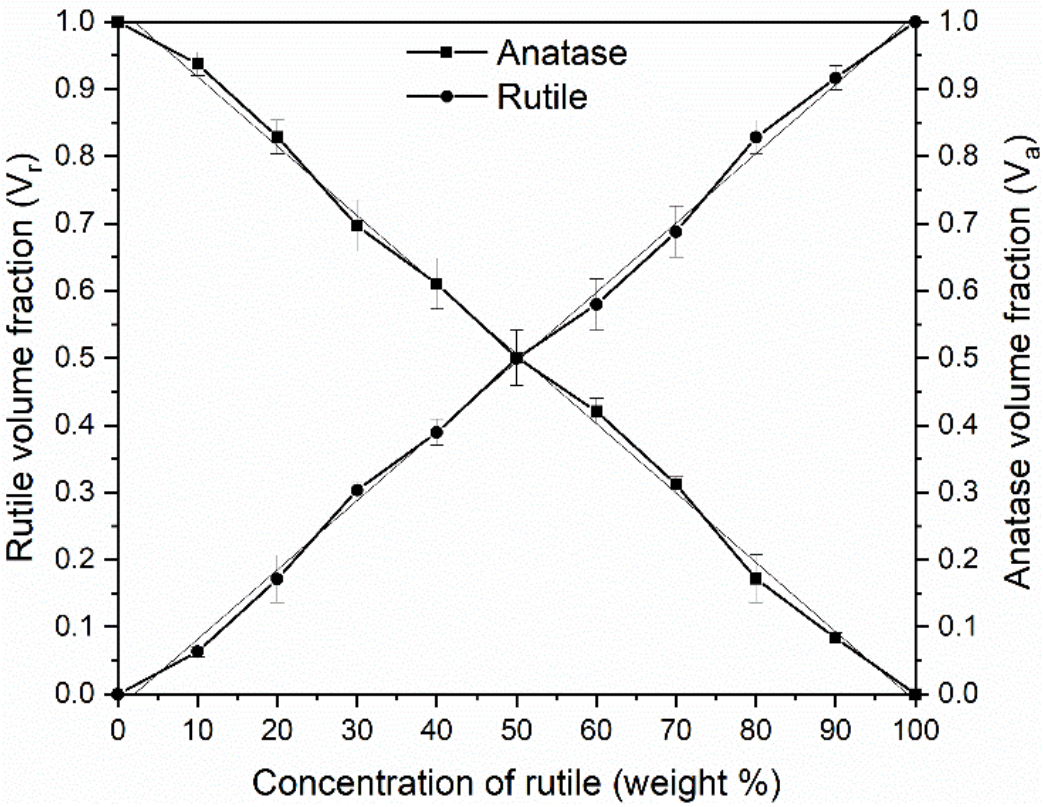

Figure 4. Calibration curve with error bars and linear fit for rutile (circle) and anatase (square) TiO_2 using AR-standards. The plot shows the progression to a higher content of rutile and a lower content of anatase.

Linear regression was performed on the calibration curve to provide a relationship of the volume fraction of rutile (V_r) and the actual percent composition (x_r) in any analyzed sample. The same would go for the anatase phase, with the difference that the percent composition calculated of anatase (x_a) would be $x_a = 100 - x_r$. From the linear fit, the following equations were obtained:

$$V_r = 0.01031x_r - 0.0212 \text{ (Eq. 3)}$$

$$V_a = -0.01031x_a + 1.0212 \text{ (Eq. 4)}$$

where V_r and V_a represent the volume fractions of rutile and anatase determined from the curve fit and x_r and x_a the actual percent composition of rutile and anatase in any sample. This linear fit had a R^2 value of 0.998. Since the volume fraction from anatase or rutile depends on the data collected for any unknown sample, it is logical to rearrange equations 3 and 4 to the following formulas:

$$x_r = 96.993\, V_r + 2.056 \text{ (Eq. 5)}$$

$$x_a = 99.049 - 96.993\, V_a \text{ (Eq. 6)}$$

Once the volume fraction of anatase and rutile of the sample is determined from the spectrum; then equations 5 and 6 can be solved to determine the actual percent composition of anatase and rutile in the sample.

2.3.3 Contour plots

The entire bleached area the laser induced ART experiment was considered for this analysis and was scanned in the Raman spectrometer with a low laser power (2 mW) and high spatial resolution (1 μm between each scan spot). An approximately 25μm × 25μm analysis grid was selected to cover the entire bleached area, and each point was scanned three times for three seconds each. The resulting spectra were inspected for rutile features, and only those spectra containing rutile were chosen to determine the rutile propagation area, which is roughly 11μm × 11μm in size. Each graph in this region was analyzed as described, and values for the rutile volume fractions were obtained using equation 2, converted to percent rutile using equation 5, and plotted in figure 5. The contour plot is a spatial and percent composition analysis, using a data matrix of 11 × 11 data points, of the sample. Each

point represents a value for percent rutile and all the points are separated by 1 µm, indicated by the tick marks on the contour plot in figure 5. Origin Lab Pro 2019b software generated this image by correlating each point in a linear fashion. The contour plot goes from 0%-100% rutile, and each color represents a percent composition as seen in the scale bar. The lines inside the contour plot are simply indicators of 5% increments. Dark purple represents 100% rutile, whereas dark red 0% rutile.

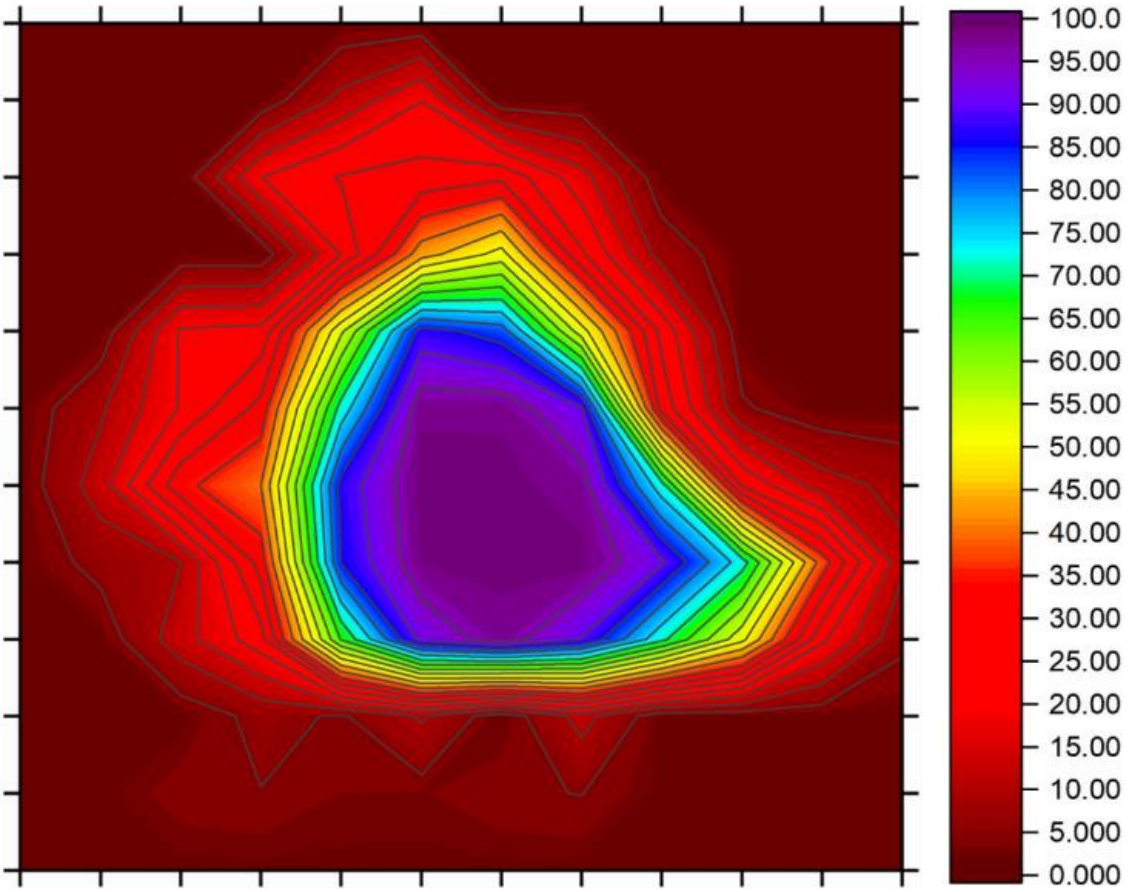

Figure 5. Contour plot of the percent rutile analyzed on a N719 dye pretreated anatase TiO_2 film. The color distribution goes from 100% rutile in dark purple to 0% rutile in dark red.

CHAPTER 3

3. RESULTS AND DISCUSSION

3.1 N719 dye pretreated TiO_2 films using 523 nm laser

Pure anatase TiO_2 films pretreated with the N719 dye were probed with Raman spectroscopy using a 532 nm green laser at 20 mW. After 1 s, the surface of the dyed TiO_2 film changed from a dark red, uniform appearance (figure 6A) to a bleached spot (figure 6B). After bleaching, the films were analyzed with a low laser power (2 mW) to obtain the Raman spectra from different positions within the bleached area, from point 1 in figure 6B, until reaching the center of the laser spot at point 4. Figure 6 shows the Raman spectrum at each point indicated in figure 6B. The spectrum from point 1 on the outer boundary of the hole, shows a typical Raman spectrum of anatase TiO_2, with the five characteristic phonon peaks of this phase, indicated by the letter "a" in figure 1, at 144 (E_g), 197 (E_g), 396 (B_{1g}), 515 (A_{1g}, B_{1g}) and 638 (E_g) cm^{-1}.[43,44] Additionally, there are features in the spectrum that are due to the dye molecules. The N719 dye is comprised of a Ruthenium metal center, surrounded by two bipyridine molecules and two thiocyanate groups.[37] The bipyridine molecules each have two carboxylic acid groups with which it can anchor, or bind, to the TiO_2 substrate.[37] Representative Raman modes of the N719 dye appear at higher wavenumbers, designated by a letter "d" in figure 6, around 1027, 1268, 1471, 1544 and 1609 cm^{-1}, indicative of the stretching modes of carbon-carbon, carbon-oxygen and carbon-nitrogen single or double bonds in the bipyridine rings and carboxylic acid anchor groups.[37,38,50,51] When the center of the bleached spot is analyzed via Raman spectroscopy, features known to be due to the rutile

phase of TiO_2, at 144 (B_{1g}), 236 (two phonon band/second-order effect), 447 (E_g) and 610 (A_{1g}) cm^{-1}, appear.[45,52,53] The spectrum collected at point 2 in figure 6, shows the typical anatase TiO_2 Raman modes, but in addition, at 447 cm^{-1} there is a characteristic rutile peak starting to grow in. At higher wavenumbers, there is no evidence of the dye features, suggesting that the dye has bleached or photo-decomposed.[33] The characteristic rutile peaks become more apparent as the points in figure 6B come closer to the center of the laser spot; in fact, the Raman spectrum of point 3 has a more accented 447 cm^{-1} rutile peak and the appearance of another rutile peak around 610 cm^{-1}. The spot where the laser irradiated the sample, point 4, has a much higher content of rutile, compared to points 3 and 2, and there is no evidence of any characteristic anatase peaks. Therefore, this Raman spectrum is representative of pure rutile TiO_2, where the distinctive peaks are labelled with a letter "r" in figure 6.

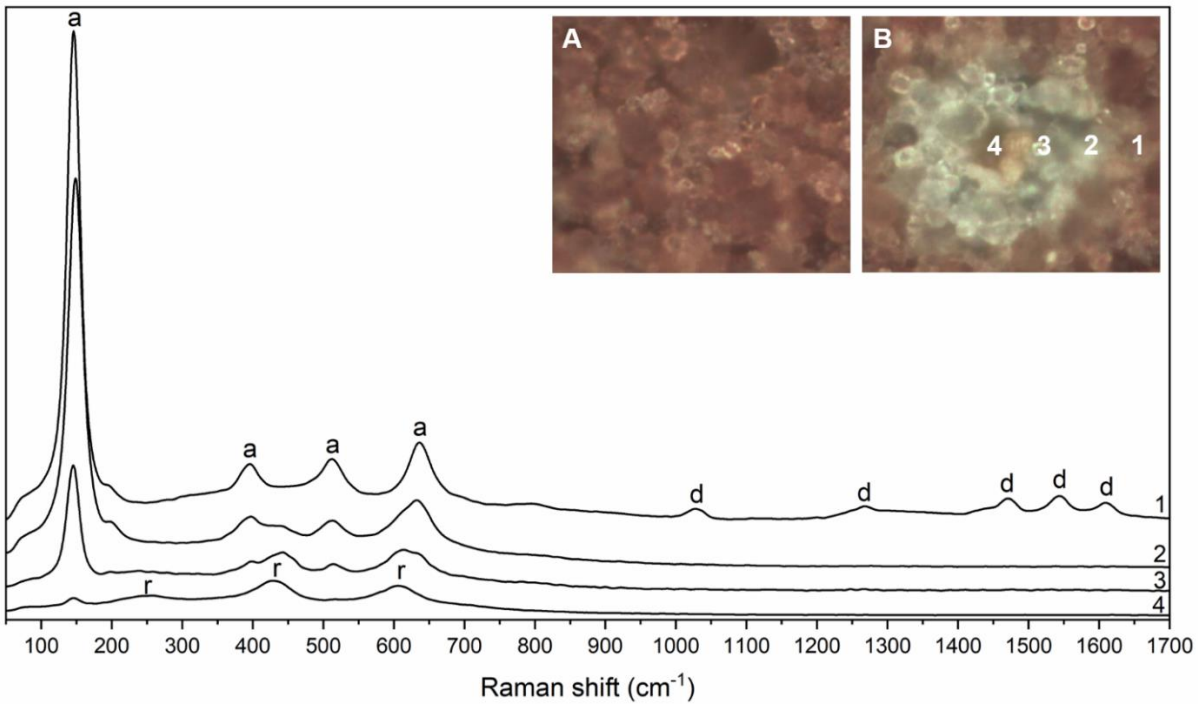

Figure 6. Raman spectra from different positions indicated from 1-4 after a 20 mW 532 nm laser pulse (1s) on the N719 dye pretreated pure anatase TiO_2 film. Figure insets A and B show the microscope image before and after the laser pulse. The letters on the graphs represent *a* for anatase, *r* for rutile, and *d* for N719 dye features.

The spectra seen in figure 6 illustrate the ART induced by the photoexcitation of the N719 dye with a green laser and show the rutile phase propagating across the area bleached by the laser pulse. The 2 mW green laser for 3 coadditions at 3 seconds used to analyze the sample surface caused a slight bleaching; however, no rutile was detected, as seen in figure 7. The ART, however, was not seen when irradiating a pure anatase TiO_2 film, with no dye present, with the same 20 mW green laser, as seen in figure 8.[16,27,28] Thus, rutile nucleation occurs where the laser irradiated the dye pretreated sample and propagates beyond the laser width of 2 µm, covering the entire bleached area (approximately a 25µm × 25µm area).[16,27,31]

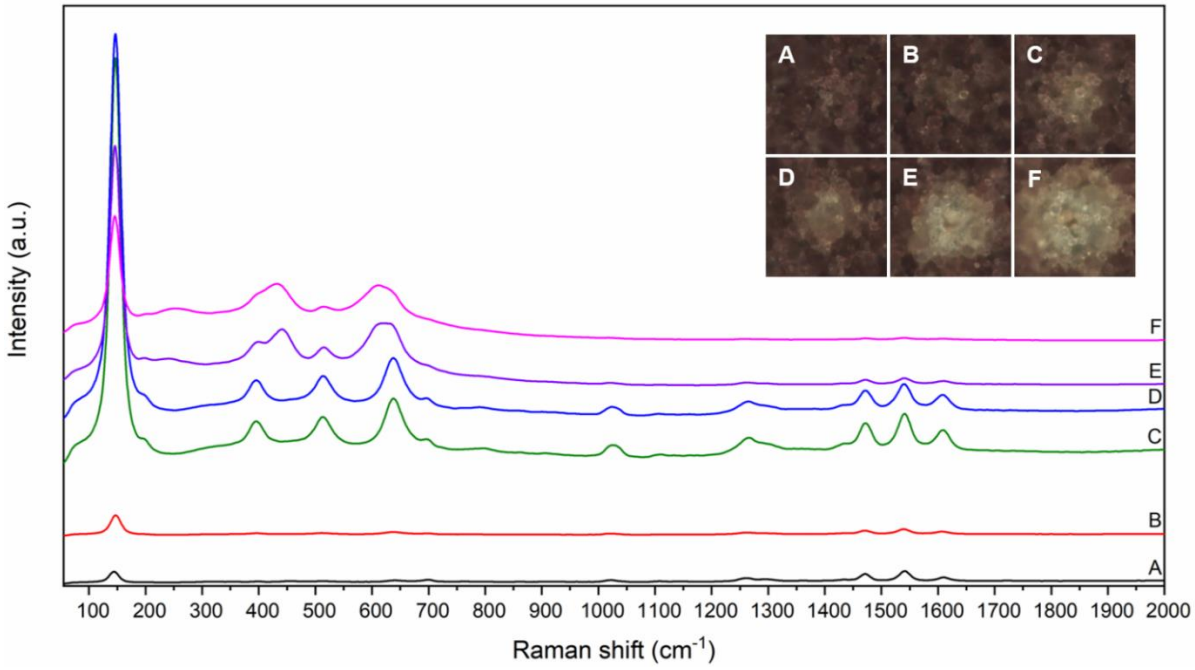

Figure 7. Raman spectra and microscope images of the irradiation of the N719 dye-pretreated TiO_2 film with different laser powers of the green (532 nm) laser. A) 1 second with 0.2 mW; B) 1 second with 2 mW; C) 3 coadditions at 3 seconds each with 2 mW (this set up was used to characterize the samples after the laser-induced ART experiment, and the irradiation caused faint bleaching; no rutile was detected); D) 1 second with 5 mW (the irradiation caused faint bleaching; no rutile was detected); E) 1 second with 10 mW (~ 70% rutile was found at the laser spot); F) 1 second with 20 mW (this set up was used to induce the ART).

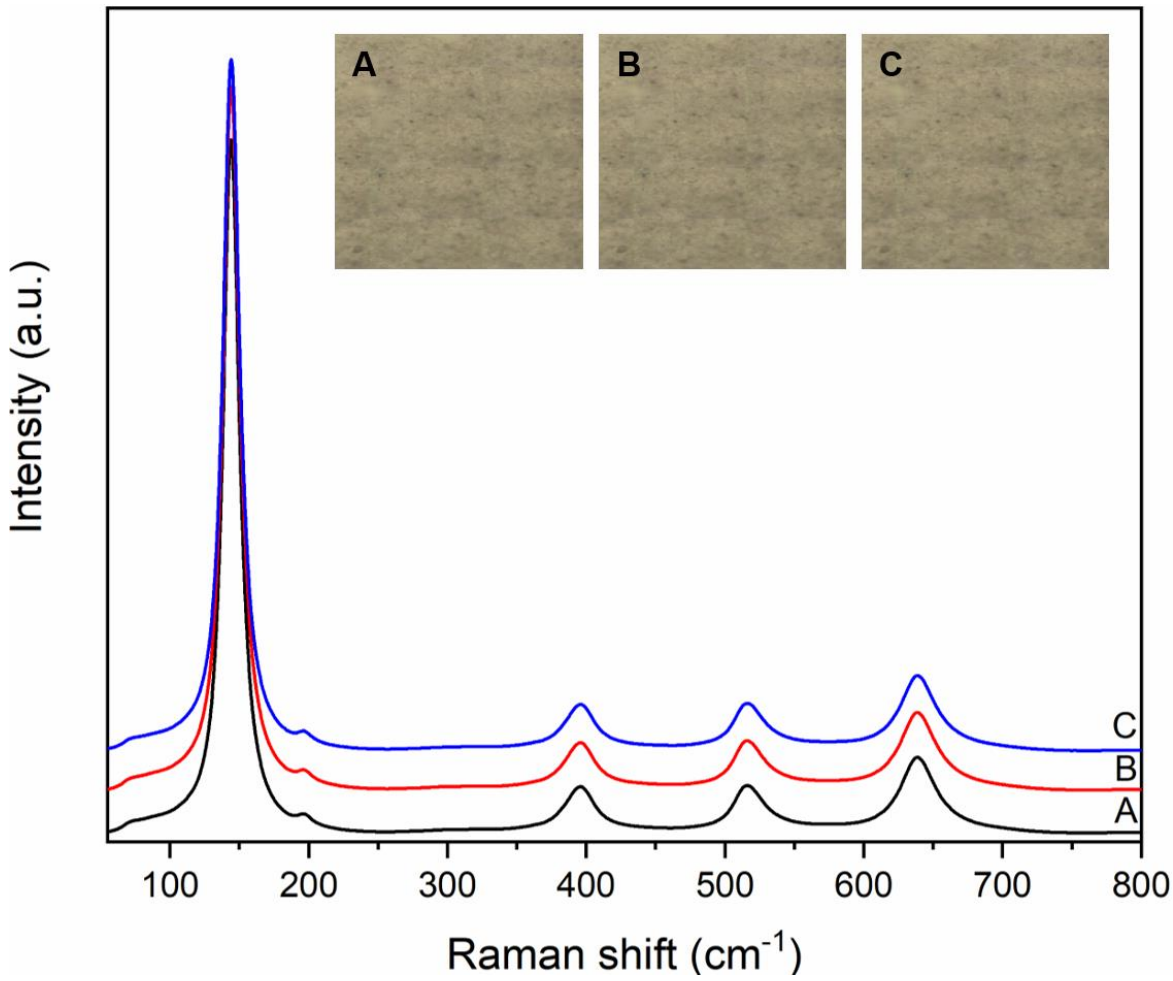

Figure 8. Raman spectra and microscope images of pure anatase TiO_2 films before (A), after irradiation with the green laser (532 nm) at 20 mW for 1 second (B), and after irradiation with the red laser (785 nm) at 25 mW for 1 second (C). The surface experienced no change and there was no rutile detected.[16,27,28]

Figures 7 and 8 show that the optical parameters chosen for the Raman analysis of the dye pretreated samples (3 coadditions at 3 seconds each with 2 mW) did not affect the results from the laser-induced ART (1 second with 20 mW). The results seen in figures 7 and 8 also serve to verify at what laser power the rutile phase starts appearing in the samples (figure 8),

and clearly indicate that a dye molecule is needed to be present in order for the sample to experience ART, since no rutile was found in pure TiO_2 samples irradiated with the highest laser power (figure 7).

3.2 N719 dye pretreated TiO_2 contour plot using 532 nm laser

The N719 dye pretreated TiO_2 film irradiated with a 20 mW 532 nm green laser for one second to induce ART was analyzed in detail to quantify the amount of rutile created on the surface and was plotted as a contour plot as shown in figure 9. The contour plot goes from 0%-100% rutile, and each color represents a percent composition as seen in the scale bar. The lines inside the contour plot are simply indicators of 5% increments. Dark purple represents 100% rutile, whereas dark red 0% rutile.

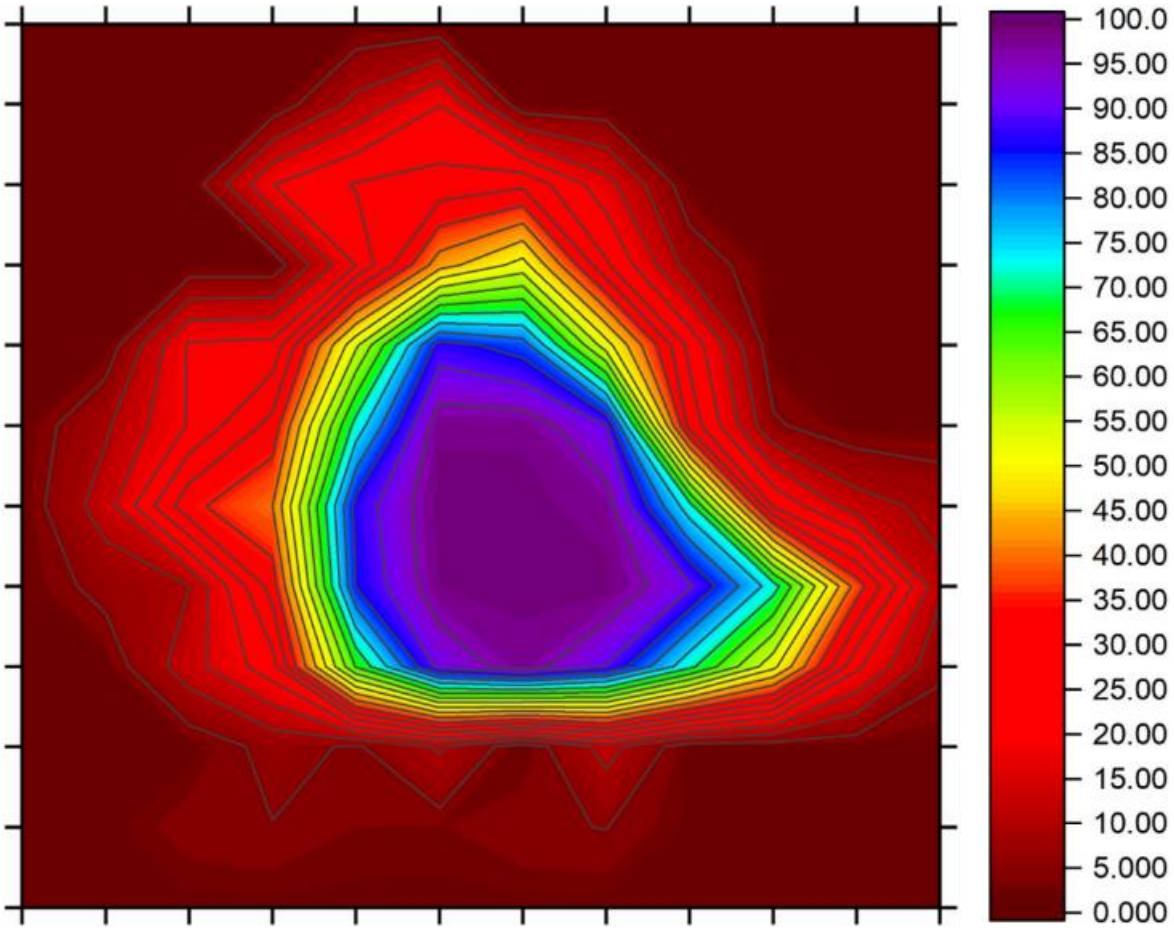

Figure 9. 11µm × 11µm contour plot of the percent rutile analyzed on a N719 dye pretreated anatase TiO_2 film irradiated for 1s with a 20 mW 532 nm laser. The color distribution goes from 100% rutile in dark purple to 0% rutile in dark red.

The contour plot in figure 9 presents how pure anatase TiO_2 coated in N719 dye is converted into rutile after irradiation with a 20 mW 532 nm laser for 1s. The phase transformation propagates from the center, where the laser impinged upon the sample which has the highest concentration of rutile, to the surroundings, where the rutile concentration gradually drops to zero. This phenomena clearly illustrates the nucleation and propagation of the laser-induced ART even beyond the area of laser excitation.[16,27,31] Spectra from the

different positions in the dark purple area show pure rutile, with characteristic peaks at 144, 236, 447 and 610 cm^{-1}, and no sign of any anatase peaks, as illustrated in the spectrum of point 4 in figure 6. This area represents percentages of rutile that are >95%, and the highest was found to be 99%. Between 5%-95% rutile in the scale bar, the Raman spectra of the different positions show a mixture of anatase and rutile phases, where the characteristic rutile peak at 447 cm^{-1} decreases, as the anatase peak at 515 cm^{-1} increases, as illustrated in points 2 and 3 in figure 6. As the rutile concentration approaches 0%, the rutile peak at 447 cm^{-1} disappears and the dye features at higher wavenumbers appear in the Raman spectrum, exemplified by point 1 in figure 6.

The experiment with the N719 dye pretreated anatase TiO_2 film irradiated with a 20 mW 532 nm laser illustrates how pure anatase is transformed into pure rutile. Figure 10 shows the UV-Vis absorption spectra for the N719 dye adsorbed on TiO_2.

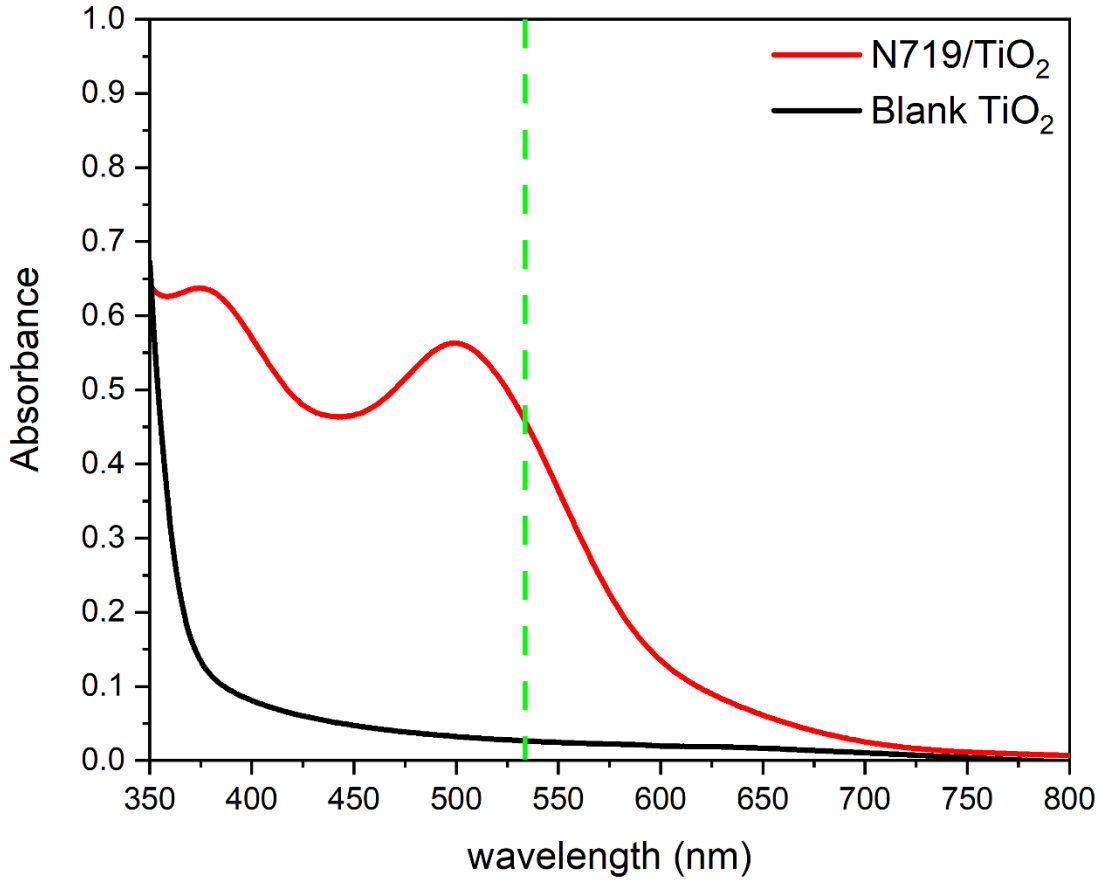

Figure 10. UV-vis spectrum of N719 dye adsorbed onto a TiO_2 film. The dotted line shows the wavelength of the green laser used for this series of experiments.

Typically, Ruthenium dyes show strong electronic transitions in the visible region of the spectrum, representing the singlet metal-to-ligand charge-transfer excitations from the Ruthenium center into the bipyridine rings.[54,55] The N719 dye adsorbed on TiO_2 in this experiment shows two peaks at 375 and 499 nm, representing these intense electronic transitions. The latter transition at 499 nm is close to the wavelength of the green laser used for the experiment, 532 nm. It is likely that when the N719 dye is excited by the 532 nm laser there is a transfer of an electron from the excited electronic state of the dye into the

TiO_2 conduction band which destabilizes the anatase phase and consequently induces the ART, similar to the process seen in DSSC.[16,27,28] However, since there is no counter electrode or a redox mediator, it is only natural for the dye to photo-decompose.[33] Clearly, the dye plays a key role in the laser-induced ART, since pure anatase TiO_2 did not create ART, even at long irradiation times, as seen in figure 8.

3.3 N749, D149 and MC540 dye pretreated TiO_2 contour plots using 532 nm laser

To further investigate, the same experiment of pretreating a pure anatase TiO_2 film with a dye and irradiating it with a green laser (532 nm) was performed with three other dyes commonly used as photosensitizers, namely the N749 dye, the D149 dye and the Merocyanine 540 dye.[5,37–41,56–58] Figure 11 shows the UV-vis absorption spectrum of the dyes adsorbed onto a TiO_2 film.

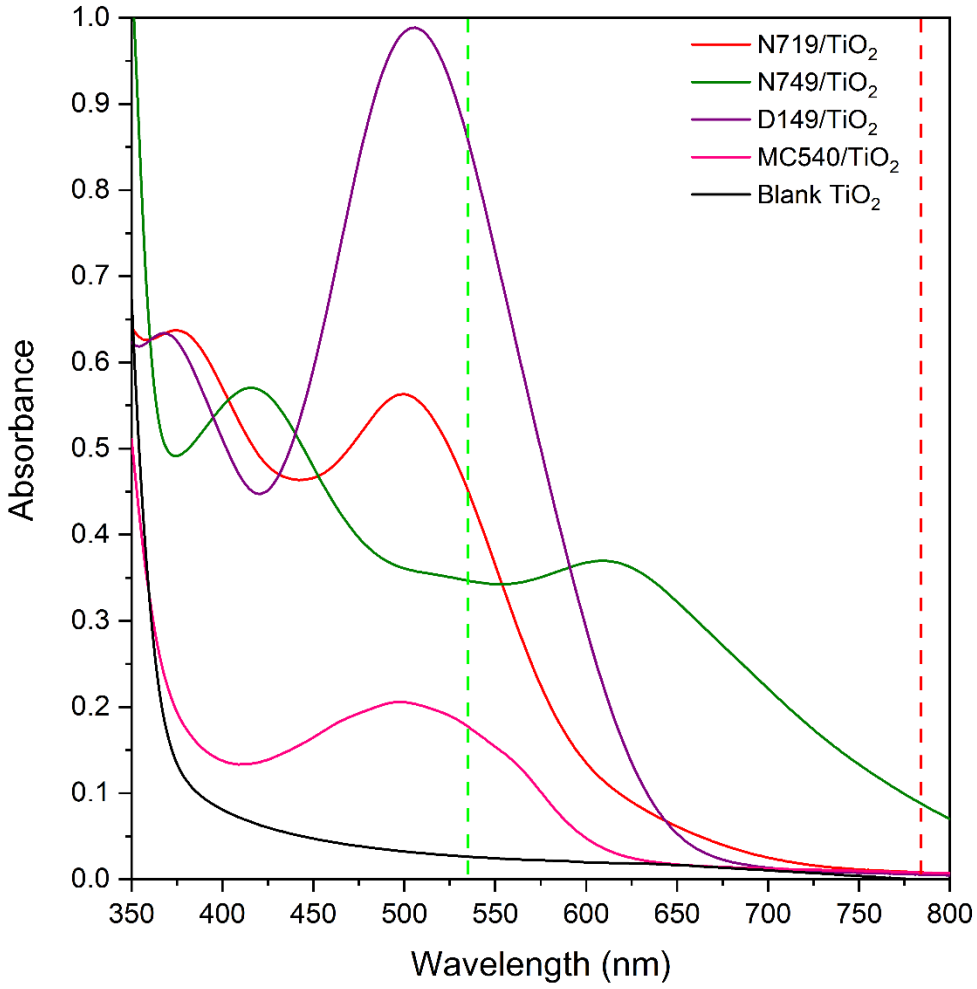

Figure 11. UV-vis spectrum of N719, N749 dye, D149 dye and MC540 dye adsorbed onto TiO_2 films. The dotted lines show the wavelength of the green and red lasers used for this series of experiments.

All dyes experience electronic transitions in the visible region; the N749 dye shows two peaks at 416 nm and 609 nm; the D149 dye also shows two peaks at 368 nm and 506 nm; and the MC540 dye only shows a single broad peak around 499 nm. The maximum absorbance peak in the visible range for all the dyes is between the wavelengths of 500 nm-600 nm, indicating that they absorb a significant amount of light at the 532 nm wavelength of

the green laser used for the experiment. Therefore, it is expected that when the dyed TiO_2 films are irradiated with the green laser, ART should be induced.

In all cases, pure anatase TiO_2 films were pretreated with dyes with identical concentrations, followed by a 1s of a 20 mW laser irradiation with the 532 nm green laser from the Raman spectrometer. The resulting spectra from each dye experiment were subjected to the same analysis performed on the N719 dye pretreated film, to create contour plots representing the percent of rutile transformation in the bleached area, as seen in figure 12. The contour plot for the N719 dye pretreated TiO_2 film is also included in figure 12(A) to better compare all the dyes.

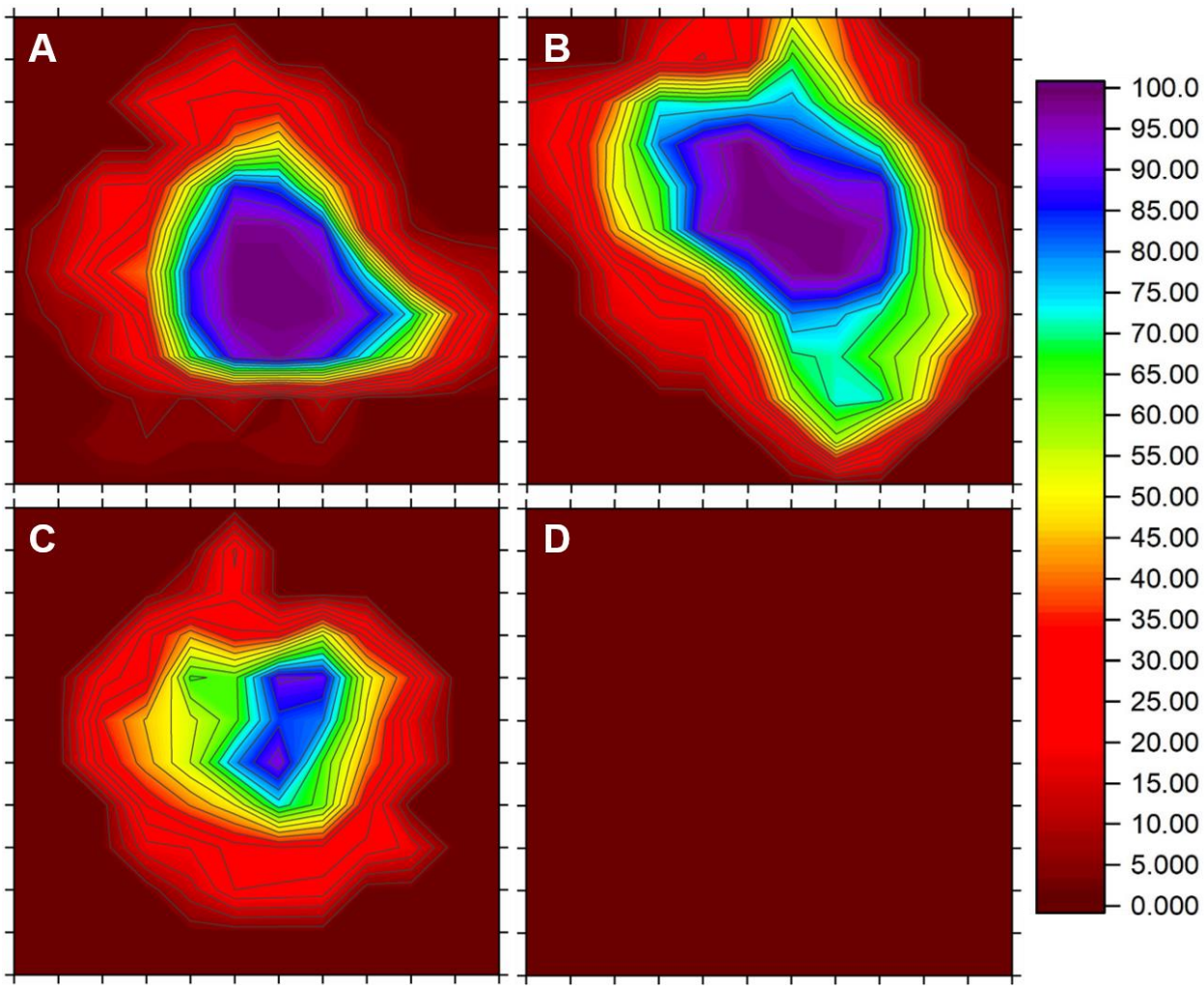

Figure 12. Percent rutile contour plot of dye pretreated pure anatase TiO_2 films irradiated with a 20 mW 532 nm laser for 1s. A) N719 dye; B) N749 dye; C) D149 dye; D) MC540 dye. The color distribution goes from 100% rutile in dark purple to 0% rutile in dark red. All the contour plots are 11µm × 11µm in size and the color scale bar goes from dark red, representing 0% rutile, to dark purple, representing 100% rutile, with 5% increments indicated by the fine black lines inside the contour plots.

From figure 12, it is evident that only three dyes, namely the N719 dye, N749 dye and D149 dye, induced the ART after laser irradiation. The MC540 dye showed no sign of

rutile being formed at the surface. In fact, the microscope image after irradiation with the 532 nm laser showed no bleaching or decomposition of the dye. One way to compare the ability of different dyes to transform the TiO_2 substrate from anatase to rutile is to look at the highest percentages of rutile found at the laser spot. For TiO_2 films dyed with the Ruthenium dyes 99% rutile was found in the dark purple area in both contour plots, meaning that pure anatase was converted into pure rutile (figure 12A and B). However, for the D149 pretreated TiO_2 film, the highest concentration of rutile found in the sample is 93%, represented by the light purple in the contour plot (figure 12C). This result follows the trend seen in the literature, where Ruthenium dyes show higher efficiency as compared to the organic dyes, when used as a photosensitizer or in DSSC.[34,36]

3.4 N719, N749, D149 and MC540 dye pretreated TiO_2 contour plots using 785 nm laser

To validate the argument that it is the electronic excitation of the dye due to absorption of the green light which leads to an electron injection from the excited state of the dye into the conduction band of the TiO_2 film that induces the ART, the same experiment was carried out by irradiating the dye pretreated TiO_2 film with a 785 nm laser. Figure 11 shows the UV-Vis absorption spectra of the dyes adsorbed into the TiO_2, and in all cases absorbance at 785 nm is significantly lower than the absorbance at 532 nm; thus, there should be minimal light absorption by the dye molecules and therefore little to no ART. The four dye-pretreated TiO_2 films were subjected to a 25 mW 785 nm 1s pulse in an attempt to induce ART. Figure 13 shows the contour plots that were generated for TiO_2 films pretreated with each dye, after the quantitative analysis was implemented. These plots were generated

following the same analysis performed on the dye pretreated TiO_2 films, as shown in figure 12.

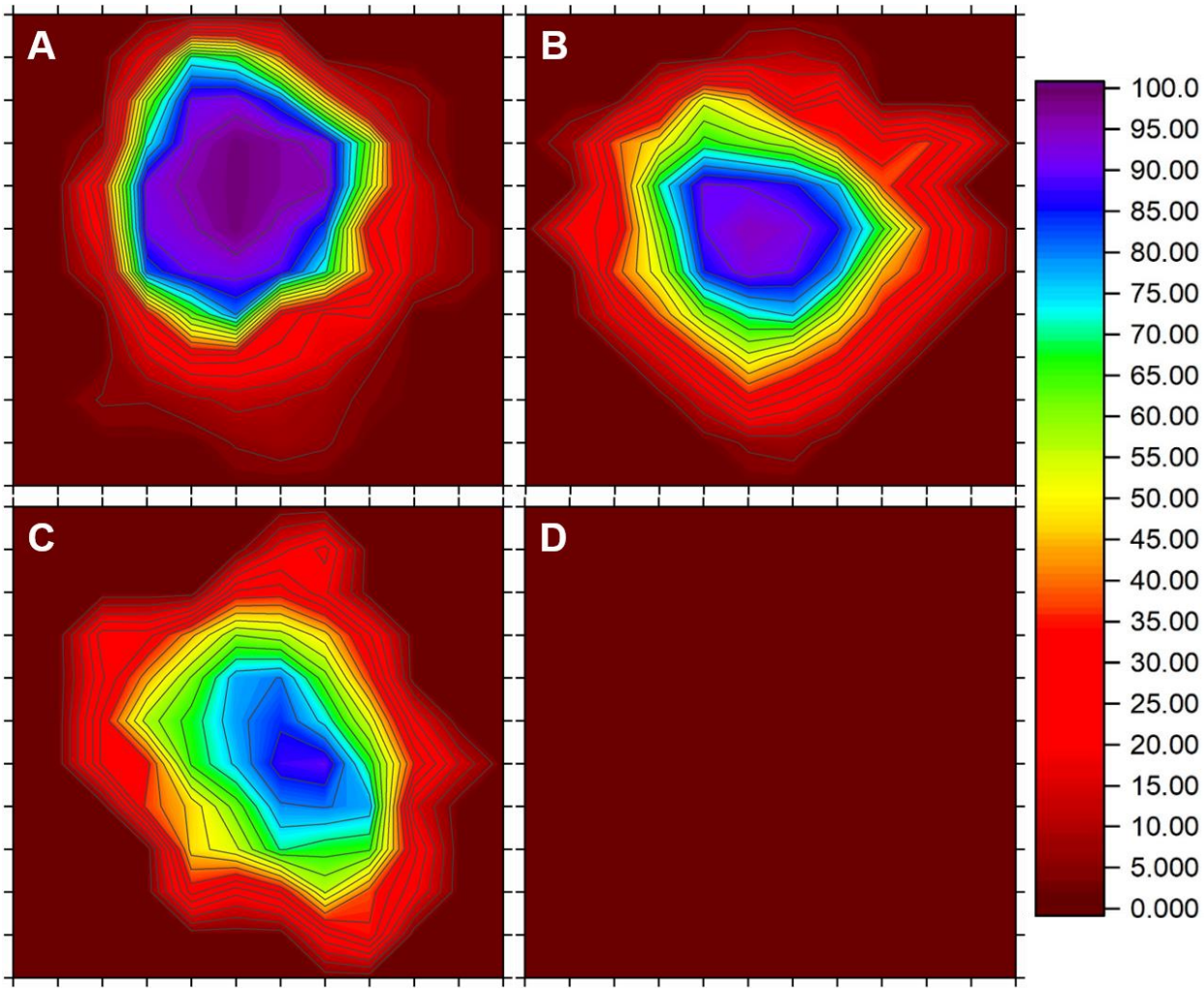

Figure 13. Percent rutile contour plot of dye pretreated pure anatase TiO_2 films irradiated with a 25 mW 785 nm red laser for 1 s. A) N719 dye; B) N749 dye; C) D149 dye; D) MC540 dye. The color distribution goes from 100% rutile in dark purple to 0% rutile in dark red. All the contour plots are 11μm × 11μm in size and the color scale bar goes from dark red, representing 0% rutile, to dark purple, representing 100% rutile, with 5% increment indicated by the fine black lines inside the contour plots.

Similar to the results with the 532 nm laser, figure 13 shows that the N719, N749 and D149 dyes induced the ART after laser irradiation with the 785 nm laser. The MC540 dye continues to show no sign of rutile transformation. Since none of these dyes strongly absorb at this wavelength, the ART is quite curious. To better understand the extent of the transformation, the highest percent rutile was compared between the samples. For the N719 dyed film, anatase was completely converted into rutile, showing 99%. In the case of the N749 dye and the D149 dye experiments, the highest percent rutile found was 95% and 90%, respectively. For this experiment with the red laser and minimal light absorbance, the Ruthenium dyes still show a higher percent rutile than the organic dye (D149), continuing to follow the trend that the Ruthenium dyes show higher efficiency than the organic dyes.[34,36] One way to compare the ability of different dyes to transform the TiO_2 substrate from anatase to rutile is to look at the area of rutile propagation, where there is between 50%-100% rutile in the contour plots, since most of the rutile created at the surface is contained within that range. Comparing the results obtained from the experiments of dyed TiO_2 films irradiated with the two different lasers, anatase was converted into rutile when N719 dye, N749 dye and D149 dye were used to pretreat the TiO_2 films. All these dye-pretreated TiO_2 films experience a visible change at the surface after laser irradiation, bleaching and the appearance of a hole at the laser spot are found during both experiments. The MC540 dye pretreated TiO_2 film did not experience visible change at the laser spot and no ART was seen during either laser experiment. For the laser-induced ART using the 532 nm laser the N719 dye pretreated TiO_2 film experienced a rutile propagation area of 36 μm^2. For the N749 dye pretreated TiO_2 film a significantly larger rutile propagation area was found, namely 72 μm^2,

twice as large with the N749 dye as with N719. The D149 dye pretreated TiO_2 film has a rutile propagation area of only 20 μm^2 after irradiation. The results using the 785 nm laser were expected to be less or nonexistent compared to the results using the 532 nm laser since all the dyes absorb visible light at 785 nm at a much lower intensity than at 532 nm. Interestingly, both the N719 dye and D149 dye pretreated TiO_2 films experience a larger rutile propagation area when using the red (785 nm) laser, namely 42 μm^2 and 39 μm^2 respectively. The slight increase in the rutile propagation area, compared to the areas obtained from the green laser experiment, might be due the increased laser power of the red laser available to us (25 mW as opposed to 20 mW for the green laser). For the N749 dye pretreated TiO_2 film, the results are as expected, and the rutile propagation area is 36 μm^2, half as small when irradiating with the 785 nm laser compared to the 532 nm laser. The MC540 dye pretreated TiO_2 film is the only dye from this experiment that did not show any ART, even though it absorbs light in the visible range in the UV-vis spectrum (figure 11). These results indicate that the dyes absorbing light near the given wavelength of the laser is not the only factor leading to ART, since using the 785 nm laser with its minimal light absorbance by the dyes ART was still achieved with similar rutile propagation areas. The fact that the MC540 dye does not induce ART begs the question of how this dye is different from the others.

3.5 DRIFTS and Raman spectra of pure dyes and dye pretreated TiO_2 films

To investigate the absorption mechanisms of the dyes to the TiO_2 films, all the samples where studied using DRIFTS and Raman spectroscopy. Both Ruthenium dyes have

carboxylic acid anchor groups. The dye molecules will bind to the TiO_2 through the carboxylic acid anchor groups and form surface carboxylates.[5,37–39] The other two commercial dyes, D149 and MC540, are categorized as organic dyes and are large, highly conjugated molecules. Like the Ruthenium dyes, the D149 has a carboxylic acid anchor group. However, the MC540 dye has a sulfonic acid anchor group, which should form a surface sulfonate when bound to the TiO_2 surface, the same way as the dyes containing carboxylic acid groups form surface carboxylates and bind to the nanoparticle surface.[40,41] Figure 14 presents the Raman and DRIFTS spectra of the pure N719 (figure 14A) and N749 (figure 14B) dyes and the dyes adsorbed onto the anatase TiO_2 surface.

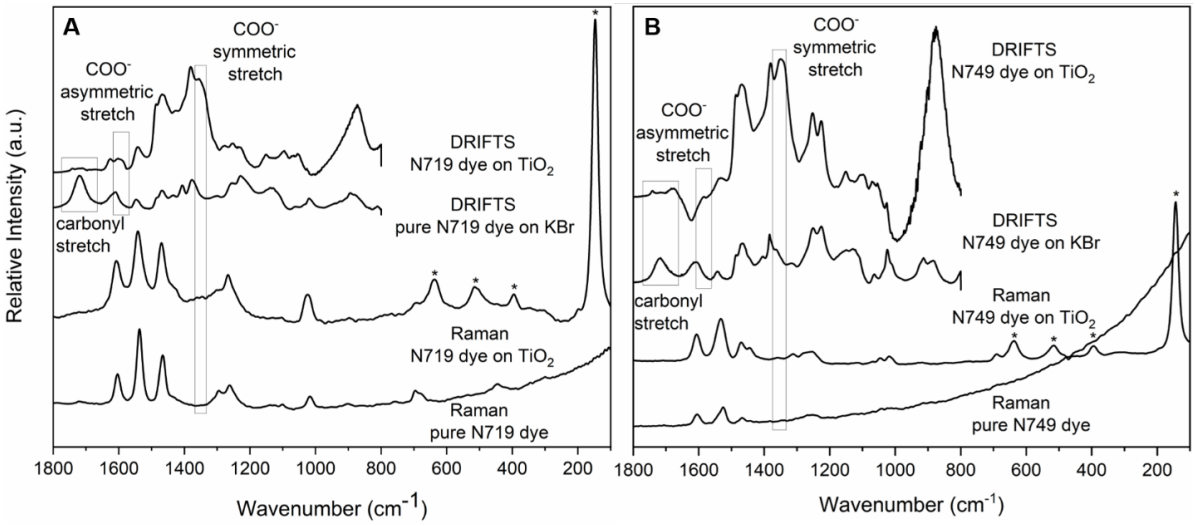

Figure 14. DRIFTS and Raman spectra of the N719 (A) and N749 (B) dyes, before and after being adsorbed to anatase TiO_2. The asterisks represent the characteristic anatase Raman peaks. The light grey squares represent the carbonyl and carboxylate regions.

The DRIFT spectra of the pure N719 (figure 14A) and N749 (figure 14B) dyes indicate the following characteristic IR bands for the carboxylic acid anchor group: at 1720 and 1717 cm^{-1} for the double bonded C=O stretching mode, at 1230 and 1250-1226 cm^{-1} for

the single bonded C-O stretching mode and at 1135 and 1130 cm^{-1} for the C-O-H bending mode, respectively.[33,37,59] In addition, peaks at 1610 and 1377 cm^{-1} for the N719 dye (figure 14A) and peaks at 1608 and 1365 cm^{-1} for the N749 dye (figure 14B) are correlated to asymmetric and symmetric stretching modes of the $–COO^-$, respectively.[33,37,59] This is an indication that both protonated and deprotonated carboxylic acid groups are present in the spectra of the pure dyes.[33,37,59] The DRIFT spectra change when the dyes are adsorbed onto the TiO_2 surface. The most prominent changes are the loss of the carbonyl peaks and the slight shift of the asymmetric and symmetric stretching modes of the carboxylate peaks found at 1599 and 1356 cm^{-1} for the N719 dye (figure 14A) and 1583 and 1349 cm^{-1} for the N749 dye (figure 14B), suggesting that the dyes are covalently bonded to the TiO_2 surface.[33,37,59] Raman shifts at 1365 and 1359 cm^{-1} indicating the symmetric stretch of the carboxylate group of the N719 (figure 14A) and N749 (figure 14B) respectively, further support the conclusion that these dyes are chemisorbed to the TiO_2.[33,37,59] The asymmetric stretch of the carboxylate is hard to recognize in the Raman spectra, due to the overlap with the pyridine Raman shifts.[37,59,60] The peak associated with the C-O-H bending was also absent when the dyes are bound to the TiO_2, further confirming the chemisorption of the dyes.[33,37,59]

Figure 15 presents the DRIFT spectra of the pure D149 (figure 15A) and MC540 (figure 15B) dyes and when the dyes are adsorbed onto the TiO_2 surface. Raman spectra were not possible to collect for these dyes, due to high fluorescence experienced during the analysis. As discussed previously, the Ruthenium dyes both show chemisorption to the substrate in the form of loss of the carbonyl peak and shift of the symmetric and asymmetric

carboxylate features. The D149 dye has a carboxylic anchor group and should present similar stretching modes characteristic of the carboxylate features, as seen with the Ruthenium dyes.

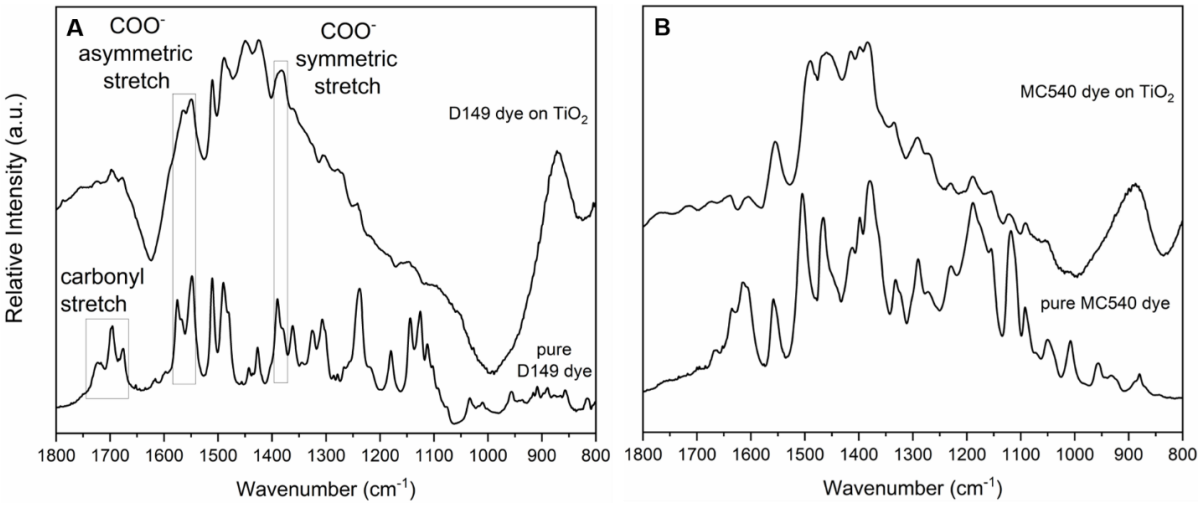

Figure 15. DRIFTS spectra of the D149 (A) and MC540 (B) dyes, before and after being adsorbed to anatase TiO_2. The light grey squares represent the carbonyl and carboxylate regions.

Similar to the Ruthenium dyes, the DRIFT spectrum of the pure D149 dye (figure 15A) presents the following characteristic peaks associated to the protonated and deprotonated carboxylic acid anchor group: at 1723-1677 cm^{-1} for the double bonded C=O stretching mode, at 1238 cm^{-1} for the single bonded C-O stretching mode, at 1144-1125 cm^{-1} for the C-O-H bending mode, and at 1548 and 1389 cm^{-1} for asymmetric and symmetric stretching modes of the $–COO^-$.[33,37,58,59] The DRIFT spectrum of the dye adsorbed onto TiO_2 (figure 15A) changes as expected for a chemisorbed molecule, namely partial loss of the carbonyl peak and the slight shift of the asymmetric and symmetric stretching modes of the carboxylate feature at 1564 and 1382 cm^{-1}, respectively.[33,37,58,59] The characteristic feature of the C-O-H bending is also absent in the spectrum of the dye adsorbed to the TiO_2. Therefore,

the D149 dye is covalently bonded to the TiO_2 surface.[33,37,58,59] The MC540 dye has a sulfonic acid group that will form a sulfonate when covalently bound to the TiO_2.[40,41] Characteristic features of the protonated and deprotonated sulfonic acid in the DRIFT spectrum (figure 15B) appear at 1413-1380 and 1092 cm^{-1} for the symmetric and asymmetric S=O stretching mode, and at 1188 and 1118 cm^{-1} for the asymmetric and symmetric stretching modes of the $–SO_3$.[61–64] However, the DRIFT spectrum of the MC540 dye adsorbed onto the TiO_2 (figure 15B) presents similar peaks, strongly suggesting that dye is physisorbed and not covalently bound to the TiO_2.

The main differences between the four dyes being tested is both the number and type of anchoring group available on the molecule. For the N719 dye, N749 dye and D149 dye, the molecules all have carboxylic acid anchor groups. Both Ruthenium dyes have three (N749 dye) or four (N719 dye) anchor groups and the organic dye D149 has one. The Ruthenium dyes showed a complete loss of the carbonyl peak as seen in the DRIFT spectra (figure 14), and experienced a full conversion of anatase into rutile, while the D149 dye still had evidence of the carbonyl peak in the DRIFT spectra of the adsorbed D149 dye (figure 15A), indicating only a partial loss of this feature. This might explain why this dye converted pure anatase into 93% rutile, and not a complete transformation. The MC540 dye only has one sulfonic acid anchor group, and the DRIFT spectrum (figure 15B) was inconclusive about the chemisorption of this dye to the TiO_2 surface, which could explain why this dye did not undergo ART. Alternatively, the sulfonic acid anchor group on the MC540 dye might not allow effective electron injection from the electronically excited dye into the TiO_2

conduction band.[3,4,34,35,65] Either way, no ART is seen when the TiO_2 film is pretreated with MC540.

CHAPTER 4

4. CONCLUSION

4.1 Summary

The assumption that the electronic excitation of the dyes leads to an electron injection into the conduction band of the TiO_2, which induces the ART, is expected for the experiment with the 532 nm laser but is surprisingly also witnessed when using the 785 nm laser. The fact that when using the 785 nm laser for all three dyes with a carboxylic acid anchor group the rutile propagation area is comparable in size introduces the idea that independent of the absorption intensity at a specific wavelength, as long as the dye is covalently bound to the substrate and the complex is able to absorb at the given frequency, there will be energy available to cause ART, since the transfer would only be possible through the bond formed between the dye molecules and the TiO_2.[3,4,34]

The induced ART due to the photoexcitation of the dyes chemisorbed to the TiO_2 films using either of the lasers showed a larger rutile propagation area when the Ruthenium dyes were used than when the D149 dye was used, following the trend that Ruthenium dyes experience higher efficiency over organic dyes.[34,36] Anatase is transformed to rutile due to the electron injection from the excited state of the dye into the conduction band of the TiO_2 through the covalent bond formed at the surface with the dye molecule.[3,34,65] Both Ruthenium dyes have more carboxylic acid anchor groups, compared to the D149 dye which only has one; thus, the likelihood of forming covalent bonds with the TiO_2 surface is higher for the

Ruthenium dyes. For the case of the MC540 dye, no rutile was found at the surface, and no clear evidence was found that this dye is chemisorbed to the TiO_2. This leads to the conclusion that MC540 has no electron injection mechanism under the conditions of this simplified experiment. The results obtained from this study agrees with the literature about the efficiency of the anchor groups that bind to the TiO_2 surface and allow electron injection from the dye molecule to the substrate, namely that carboxylic acid anchor groups are the preferred moiety in dyes over sulfonic acid anchor groups for this purpose.[3,4,34,35,65]

The system investigated in this work, the interface of a dye molecule chemisorbed to a TiO_2 film, somewhat resembles the interface found in DSSC. Conventional wisdom in DSSC states that, when the dye molecule is excited by the sunlight, there should be a spontaneous electron injection from the excited state of the dye molecule into the conduction band of the semiconductor.[3,4,34] However, this is only possible when the dye is covalently bound to the TiO_2 surface.[3,4,34] In a DSSC, the electron that was transferred into the TiO_2 conduction band subsequently travels to the counter electrode, thus converting solar light into electricity. The simplified system investigated here can be considered half a DSSC, where only the dye-TiO_2 interface is considered. Like in a DSSC, the dye chemisorbed onto the TiO_2 will get electronically excited by the high-power laser irradiation, and as expected, there will be a spontaneous electron injection from the excited state of the dye molecule into the TiO_2. However, without a counter electrode there is no place for that electron to go, so the energy instead is dissipated into a phase change.[16,27,28,31,33] Laser-induced ART was only seen when the dyes were covalently bound to the substrate via a surface carboxylate, namely in the films pretreated with the N719, N749 and D149 dyes. The electron injection induces

the ART and causes the dye to photo-decompose, since there is no counter electrode to transfer the electrons and generate electricity and no redox mediator to regenerate the dye molecule. The Raman spectrometer for this experiment was very useful in probing the dyed TiO_2 films with high power lasers to induce ART and then analyze the surface with low laser power. For that reason, a Raman spectrometer could be convenient to use as a test for scientists developing dyes for DSSC; if the sample experiences ART upon high power laser irradiation, then the electron injection necessary for a successful DSSC was achieved. [22]

4.2 Conclusions

Anatase TiO_2 was converted into rutile by irradiation with a visible laser when the TiO_2 film was pretreated with dyes commonly used in DSSC (N719 dye, N749 dye and D149 dye). When the samples were irradiated with a 532 nm or a 785 nm laser, all the dyes were electronically excited, injecting an electron from the excited state of the dye molecule into the conduction band of the TiO_2, as seen in a DSSC. This electron injection destabilizes the anatase TiO_2, which induces ART. Since there is no counter electrode or redox mediator the dye photo-decomposes, as evidenced by a bleaching at the laser spot. Contour plots, uniquely designed for this study, helped to visualize, and quantify the laser-induced ART. Raman and DRIFTS spectra verified that these three dyes were chemisorbed to the surface of the TiO_2, allowing for the efficient electron injection through surface carboxylates. The MC540 dye, with a sulfonic acid anchor group, did not induce ART with either laser and the DRIFT spectrum was inconclusive about the chemisorption of this dye to the TiO_2, illustrating that the sulfonic acid anchor group is not efficient in the electron injection process. Factors such

as visible light absorbance and chemisorption of the dye to the semiconductor are the major sources of the efficient electron injection that induced the ART. This experiment shows a simple method to test dyes used for DSSC and confirm the electron injection from the excited state of the dye into the conduction band of the TiO_2, by examining the ART. The more ART that occurs, the more efficient said dye will be for use in DSSCs. The overall results from this study follow the trends in the literature, where Ruthenium dyes show higher performance in DSSC over the organic dyes, as well as the carboxylic acid anchor groups are the preferred moiety in dyes.[3,34,65]

5. EPILOGUE

Elucidating the photocatalytic oxidation of acetaldehyde with the dual-cocatalyst Ag-FeOx-TiO_2 nanocomposite

Oral qualifying exam proposal developed by Daniela (Labadini) Graf Stillfried Barreto

5.1 Significance

Currently, Americans spend most of their time indoors, approximately 90% of their day.[66,67] Indoor air is 10% more contaminated with volatile organic compounds (VOCs) than outdoor air.[68] Heterogeneous photocatalysis, also called photocatalytic oxidation (PCO), is a clean technology with the capacity to photodegrade VOCs into carbon dioxide (CO_2) and water (H_2O) at room temperature.[67,69–71] Titanium dioxide (TiO_2) is considered one of the most promising photocatalysts and has been vastly investigated for PCO, due to its chemical stability, non-toxicity, and low cost.[72–74] The general working principle of PCO begins with the activation of the photocatalyst with light of sufficient energy followed by the generation of photogenerated electron-hole pairs which drive the surface reactions.[75–78] The major drawbacks of TiO_2 PCO is the fast recombination of the electron-hole pairs and that it can only be activated with UV light, which is no more than 5% of sunlight.[13,79,80] Therefore, it is of extreme importance to synthesize TiO_2-based visible-light absorbing photocatalysts that efficiently photodegrade indoor VOCs.

Strategies for developing visible-light absorbing TiO_2-based photocatalysts include doping TiO_2 nanoparticles with compounds such as noble metals, metal oxides, carbonaceous materials, etc.[80,81] Noble metal dopants can act as electron sinks and provide effective proton

reduction sites, making them a reduction cocatalyst; in addition, some noble metals (Au and Ag) can enhance the visible light absorbance of TiO_2.[81–85] Colored metal oxides, such as iron oxide (FeOx) also absorb visible light, due to their narrower band gap energy.[86,87] Most metal oxide dopants act as oxidation cocatalysts since they capture photogenerated holes.[81] In order to maximize PCO using TiO_2-based nanocomposites, incorporating more than one cocatalyst serves to combine the properties of both reduction and oxidation cocatalysts, such as better separation of the photogenerated electron-hole pairs, visible light absorbance, and an increase in active sites.[81]

In this study, Ag and FeOx dopants, acting as reduction and oxidation cocatalysts, respectively, will be used to synthesize visible-light absorbing Ag-FeOx-TiO_2 nanocomposites for the PCO of a model indoor air VOC, acetaldehyde. The surface chemistry of the Ag-FeOx-TiO_2 nanocomposites will be investigated before, during, and after the PCO of acetaldehyde using *in situ* surface analytical techniques. This research project will provide insightful information about the role of surface hydroxyls and active surface species on the dual-cocatalyst-nanocomposites during the PCO of acetaldehyde. It is important to understand how these surface active sites and hydroxyls relate to the formed surface intermediates, products, and by-products. Ultimately, this information will help determine a clear reaction mechanism for the PCO of VOCs using visible light absorbing TiO_2-based photocatalysts. The main goal of this study will be to determine the optimal TiO_2-to-dopant ratio to maximize the visible light absorbance and efficiently photodegrade a model VOC, acetaldehyde.

5.2 Research aims

1. Synthesis and characterization of Ag-TiO_2, FeOx-TiO_2, and Ag-FeOx-TiO_2 nanocomposites, including composition, size, surface area, crystallinity, and analysis of surface hydroxyls and active sites, to determine the optimal TiO_2-to-dopant ratio to maximize visible light absorption.
2. Elucidate surface chemistry of the optimal TiO_2 nanocomposites during the reaction with acetaldehyde in the dark and as a function of relative humidity.
3. Elucidate surface chemistry of the optimal TiO_2 nanocomposites during the photocatalytic oxidation of acetaldehyde under visible light and as a function relative humidity.

5.3 Background

5.3.1 Indoor air quality and acetaldehyde

Typically, Americans spend 90% of the day indoors. Therefore, indoor air will impact people's health, comfort, and productivity. Long-term exposure to indoor air pollutants can be detrimental to human health, causing "sick building syndrome" (headaches and dizziness), and in some extreme cases, cancer.[88,89] Volatile organic compounds (VOCs), nitrogen oxides (NO_x), carbon monoxide (CO), and particulate matter are known to be the main indoor air pollutants. The main sources of VOCs come from combustion by-products (e.g., stove or oven), building and furniture materials, office equipment (printers and computers), and consumer products (e.g., cleaning products). Technologies to remove indoor air pollutants include adsorption,[90] condensation,[91] plasma combined with catalysis,[92–94] incineration and thermic combustion,[91] and ozonation.[95] All these methods are known to generate large

quantities of toxic by-products and solid intermediates that linger on the surface of the photocatalyst. The working principle of these methods is basically a transfer of the VOCs from the gas-phase into a liquid/solid phase, i.e., moving the VOCs from one place to another. The VOCs are therefore not broken down into simpler and less toxic molecules. Acetaldehyde is an important indoor pollutant released by some building materials (polyurethane foams), cigarettes, adhesives, coatings and inks.[96] Aldehyde concentrations are higher indoors than outdoors, which can lead to "sick building syndrome".[96,97] The effect to human health is dependent on the amount of aldehyde present, as well as length and frequency of exposure. In general, acetaldehyde can irritate the human respiratory system by inhalation, adversely affect the cardiovascular system, irritate skin and eyes upon contact, and it is classified as a carcinogen.[98] Acetaldehyde concentration in indoor air is typically found at levels of parts per billion (ppb), but higher concentrations, 25-200 parts per million (ppm), have been found to cause eye and upper respiratory tract irritation.[98] Therefore, for indoor air quality purposes, it is important to efficiently remove acetaldehyde from the environment.

5.3.2 Heterogeneous photocatalytic oxidation

Heterogeneous photocatalytic oxidation, also known as PCO is a process where light is used to activate a solid photocatalyst in order to reduce air pollution. PCO technology has attracted great attention for removal of gaseous pollutants at low concentrations (ppb level) owing to its superior features over traditional methods, including room temperature operation, activity towards various contaminants and the ability to photodegrade them to

benign products, such as CO_2 and H_2O. Depending upon the photocatalyst used for the PCO, there are typically no significant by-products generated and the reactions occur without the use of solvents.[67] When using PCO for indoor air pollution abatement purposes, the reaction is a heterogeneous photocatalytic reaction, where the amount of water is limited and varies with different humidity levels. TiO_2 is one of the preferred materials to be used as a photocatalyst and has been vastly investigated for PCO reactions of dyes, water contaminants and VOCs.[2,12,76,78,99] TiO_2 can be found as anatase, rutile and brookite crystalline phases.[2,8,11,75] Of all the crystalline phases, rutile is considered the more thermodynamically stable, while anatase is more photoactive.[8,13,75] In most of the studies, TiO_2 is used as a mixture of anatase and rutile crystalline phases, where the typical ratio is 80% anatase and 20% rutile. This mixture can be found commercially as P25. Researchers prefer P25 over pure rutile or pure anatase TiO_2 mostly due to the increase in the photocatalytic activity owed to the synergistic effect provided by the combination of the two crystalline phases.[8,14] In addition, due to the defective nature of TiO_2, which include oxygen vacancies, or Ti^{3+} and Ti^{4+} interstitials, it can readily react with water in the environment, forming surface hydroxyls in order to satisfy the defect sites.[100] The surface hydroxyls play a vital role in the reactivity of TiO_2, aiding in the adsorption of molecules to the TiO_2 surface, or reacting with adsorbates to create surface intermediates or products.[100]

The PCO reaction is initiated by activating the photocatalyst with light of sufficient energy, i.e., UV light with pure TiO_2. Electrons in the valence band are excited to the conduction band, leaving holes in the valence band. Typically, these electron-hole pairs migrate to the photocatalyst surface, where they initiate redox reactions with adsorbed VOCs.

One concern is that the majority of the photogenerated electron-hole pairs will recombine in the bulk or at the surface which would affect the photocatalytic activity. However, for heterogeneous PCO, adsorption of organic compounds on the surface of the photocatalyst is often mentioned as a prerequisite for photocatalytic reactions, and thus the photogenerated electrons and holes can directly react with the adsorbed VOCs.[12,71,77,78] Therefore, it is important to study the surface reactions between the photocatalyst and the VOCs in the dark and during visible light irradiation, in order to decipher the reaction mechanism.

5.3.3 Dopants/Cocatalysts

The practical application of TiO_2-based photocatalysis is restricted by the rapid recombination of photogenerated charge carriers and narrow light response range.[81] Therefore, there is a need to find visible-light absorbing photocatalysts that effectively photodegrade the VOCs using sunlight, providing enhanced photocatalytic activity by efficiently separating photogenerated electrons and holes. Dopants, or cocatalysts, are considered enhancement/reinforcement materials that can lower the electron-hole recombination and thus improve the photocatalytic activity (increase the number of active sites) and stability of the main photocatalyst, and most importantly extend the light absorbance into the visible range.[81] Cocatalysts are categorize into reduction and oxidation cocatalysts, meaning they capture either the photogenerated electrons or holes, respectively. Noble metals, such as Ag, are examples of reduction cocatalysts, and metal oxides, such as FeOx, are considered oxidation cocatalysts.

It is thought that incorporating noble metals like Ag into TiO_2 improves the visible light absorption of the photocatalyst.[101] In addition, silver nanoparticles facilitate the separation of photogenerated electron-hole pairs when integrated into TiO_2.[102] One study showed that a system incorporating silver nanoparticles on TiO_2 as dopants up to 5 wt% was able to photodegrade formaldehyde more efficiently than pure TiO_2. The Ag-doped photocatalyst showed an absorption peak around 450 nm in the UV-Vis spectrum, allowing the photocatalyst to absorb in the visible range. The photocatalyst doped with 5 wt% of Ag, therefore indicated an improvement in the photocatalytic activity of the photocatalyst both by absorbing in the visible range, and reducing the electron-hole recombination.[101] However, in this study, increasing the silver nanoparticles content in the photocatalyst above 5 wt% decreased the photocatalytic activity of the substrate.

Similar to the silver nanoparticles, FeOx nanoparticles incorporated on the TiO_2 are also thought to promote the charge separation of photogenerated electrons and holes.[103,104] More importantly, FeOx nanoparticles are considered photocatalysts on their own and present a lower band gap than TiO_2 nanoparticles, which allows them to absorb light in the visible range. Therefore, introducing FeOx into the co-catalytic system will provide more active sites, allow for better charge separation, and enhance the visible light absorbance, thus improving the overall photocatalytic activity of the FeOx-doped TiO_2 photocatalysts. One study reported that adding up to 1.8 wt% FeOx nanoparticles to TiO_2 significantly improved the visible light absorbance by showing an absorption peak around 540 nm in the UV-vis spectrum, however, when testing the photocatalyst for the photocatalytic oxidation of acetaldehyde, 0.1 wt% of iron oxide nanoparticles showed the best performance.[104] This

indicates that more iron content improves the visible light absorbance, but also can decrease the photocatalytic activity, since the FeOx nanoparticles are bigger in size, which has been proven to facilitate the electron-hole recombination.[87,103,104]

Thus, adding Ag or FeOx nanoparticles to TiO_2 has been shown to enhance visible light absorbance and decrease electron-hole recombination, thus improving the photocatalytic efficiency of doped TiO_2 photocatalysts. Ag or FeOx doped TiO_2 photocatalysts have been shown to be more efficient in photodegrading dyes or water-contaminants in solution, compared to pure TiO_2.[103–107] However, few studies report the PCO of VOCs using doped-TiO_2 photocatalysts.[105,106] In addition, there is very little information about combining Ag and FeOx nanoparticles to create the dual cocatalyst Ag-FeOx-TiO_2 nanocomposite and use it for the PCO of VOCs. One study reports the photocatalytic oxidation of pentoxifylline, a recalcitrant vasodilator drug, using TiO_2-based nanocomposites doped with Ag and Fe.[106] Researchers demonstrated that incorporating 1.5 wt% of Ag and iron-containing clay beads with TiO_2 resulted in a Ag-Fe-TiO_2 photocatalyst with high photocatalytic efficiency; it enhanced visible light absorbance and increased the photocatalytic activity, compared to pure TiO_2 and Ag-TiO_2. Similar to much of the research performed on doped-TiO_2, this study carried out PCO of the drug in solution; therefore, there is a missing hole in the literature, studying novel Ag-FeOx-TiO_2 nanocomposites for the PCO of VOCs found in indoor air. Previous studies published on Ag-TiO_2 or FeOx-TiO_2 nanocomposites for the PCO of VOCs, investigate how these photocatalysts efficiently photodegrade the molecules found in indoor air with visible light, but the results are heavily focused how much CO_2 was formed and using this data to calculate the photocatalytic efficiency of the photocatalyst.[103–105,108] Typical

experiments are performed in photocatalytic reactors with a gas chromatogram (GC) used to identify products and by-products. Very little information is known about the surface chemistry before, during, and after PCO of VOCs and how this influences the formation of the products. Therefore, the fundamental surface science investigation proposed here will provide insight about the surface intermediates that play a vital role in the PCO of acetaldehyde by the novel visible light absorbing dual cocatalyst Ag-FeOx-TiO_2.

5.3.4 PCO of acetaldehyde with pure and doped TiO_2

The PCO of acetaldehyde on TiO_2 has been studied extensively, either on its own or through the PCO of ethanol on TiO_2, where acetaldehyde is the main intermediate.[97,109–121] There is some disagreement on which intermediates are formed from acetaldehyde and how they are finally converted into CO_2. Typically, anatase or P25 TiO_2 were used as photocatalysts, and the PCO was performed in different types of photoreactors with UV-light irradiation, where the outlet gases were analyzed by GC. Most studies on acetaldehyde photodegradation report that the main intermediate is acetic acid, which then photo-oxidizes into CO_2.[97,109,114–118] One of these studies was able to identify other surface intermediates, such as formaldehyde and formic acid, when they analyzed the TiO_2 surface with FTIR-ATR after the PCO reaction.[97] Other authors studied the PCO of ethanol and found that the main surface intermediate is acetaldehyde.[110–112,119–121] Consequently, the studies show that once acetaldehyde is formed at the surface, it further photo-oxidizes to acetic acid, to produce formaldehyde, formic acid and finally CO_2.[111] Another group found that acetaldehyde is transformed into a mixture of formic acid and formaldehyde, which further photo-oxidizes

into formic acid and CO_2.[111] *In situ* FTIR studies validate the presence of acetates and formates, evidenced by the symmetric and asymmetric carboxylate (COO^-) stretches between 1300-1500 cm^{-1}, and carbonyl peaks around 1700 cm^{-1}. These surface features have the potential to lead to the formation of acetic acid, formaldehyde, and formic acid as surface intermediates during the PCO of acetaldehyde over TiO_2.[96,122,123] The FTIR studies agreed that the main intermediate for the PCO of acetaldehyde is surface bound acetate, with the potential of forming acetic acid, but they differ with the following intermediates involved in the formation of CO_2.

There is still disagreement on the different photocatalytic pathways present in the PCO of acetaldehyde on TiO_2. Most of the studies report similar intermediates; however, some studies do not report any intermediates and say that acetaldehyde is photo-oxidized directly into H_2O and CO_2. Diffuse reflectance infrared Fourier transform spectroscopy (DRIFTS) is a powerful technique able to investigate surface intermediates involved in the PCO of acetaldehyde.[101,102] In fact, this tool has led to the discovery of key surface intermediates of various PCO reactions of VOCs using TiO_2 based photocatalysts, which have ultimately influenced the proposed reaction mechanism of studies that did not use this surface characterization technique.[124]

The PCO of formaldehyde has been investigated with Ag-doped TiO_2 photocatalysts using *in situ* DRIFTS. It was found that incorporating up to 5 wt% of Ag into the TiO_2 enhanced the visible light absorption and improved the photocatalytic activity.[101] Formaldehyde was photo-oxidized into H_2O and CO_2, which was verified by combining the GC data with DRIFTS. DRIFTS data showed that Ag nanoparticles facilitated the

photodegradation of formaldehyde by visible light irradiation, evidenced by the formation of formate species on the surface. The same experiment was done with pure TiO_2, and no formate features were seen in the DRIFTS spectra, showing that pure TiO_2 cannot be activated by visible light, and thus indicating that Ag plays a key role for visible light absorbance. Another study incorporated 0.1 wt% of FeOx nanoparticles into TiO_2, which resulted in the highest photocatalytic efficiency for the oxidation of acetaldehyde while enhancing visible light absorbance.[104] Transmission FTIR data during the PCO reaction showed surface bound acetate features as an intermediate during the PCO of acetaldehyde.

These studies were able to identify surface intermediates during the visible light PCO of VOCs on doped TiO_2 substrates. Unfortunately, there is missing information on evaluating DRIFTS or FTIR data by incorporating more than one dopant and varying the percentage of each dopant in the photocatalyst. In addition, monitoring the relative intensity of the characteristic IR bands of the surface intermediates as a function of irradiation time will lead to a better understanding of how the PCO reaction is progressing. Ultimately, this will give insight to develop a realistic reaction mechanism of the PCO of VOCs using visible light. It is likely that the oxidation reaction happens either through the photogenerated electrons or holes, active surface sites from the dopants or the TiO_2, or surface hydroxyls. DRIFTS will allow the monitoring of surface intermediates and surface hydroxyls on the photocatalyst surface and evaluate the role they play in PCO reactions. Additionally, transmission FTIR studies of the headspace over the photocatalyst will allow the observation of IR-active gas-phase products and by-products of the PCO of VOCs using visible light. In fact, one study of the PCO of ethanol over TiO_2 nanoparticles with UV-light attempted the simultaneous FTIR

analysis of the surface and gas-phase reactions, by connecting a DRIFTS setup with a transmission FTIR gas cell together.[125] Researchers found that adsorbed ethanol quickly transformed into acetate features upon UV-light irradiation, and characteristic bands for CO_2 and acetaldehyde were seen in the gas-phase spectra as the formed products of the PCO of ethanol. Thus, this setup of monitoring the surface and gas-phase reactions will provide insightful information about the reaction mechanism of the PCO reactions.

This proposal outlines a fundamental *in situ* surface science investigation of visible-light-absorbing Ag-FeOx-TiO_2 nanocomposites, with varying compositions of Ag and FeOx, from 0-5%. These nanocomposites will be used for the PCO of acetaldehyde using visible light as a model indoor air VOC. An intensive characterization of the Ag-FeOx-TiO_2 nanocomposites will be performed using diffuse reflectance ultraviolet-visible spectroscopy (DR-UV-Vis), Raman spectroscopy, powder X-ray diffraction (PXRD), scanning electron microscopy with elemental analysis (SEM, EDX), surface area analysis, X-ray photoelectron spectroscopy (XPS), and DRIFTS. Once characterization is complete, the PCO of acetaldehyde by the Ag-FeOx-TiO_2 nanocomposites will be investigated via DRIFTS under visible light irradiation by varying relative humidity, dopant concentration and visible light density, in order to determine the effect each has on the PCO reaction. The information obtained from these in-depth *in situ* studies of the surface chemistry of Ag-FeOx-TiO_2 nanocomposites will allow researchers to use these inexpensive nanocomposites effectively and efficiently for the PCO of indoor air VOCs using visible light.

5.4 Research Plan

5.4.1 Aim 1

Synthesis and characterization of Ag-TiO_2, FeOx-TiO_2, and Ag-FeOx-TiO_2 nanocomposites, including composition, size, surface area, crystallinity, and analysis of surface hydroxyls and active sites, to determine the optimal TiO_2-to-dopant ratio to maximize visible light absorption.

Pure TiO_2, Ag-TiO_2, FeOx-TiO_2 and Ag-FeOx-TiO_2 photocatalysts will be synthesized to conduct the proposed research. TiO_2 nanoparticles will be the main component of the nanocomposites, namely a mixture of anatase and rutile, similar to P25, which has shown excellent photocatalytic properties.[8,14] FeOx and Ag nanoparticles will be used as dual-cocatalysts, in order to extend the light absorption of the TiO_2 into the visible range. TiO_2 nanoparticles will be prepared by a well-established precipitation technique using titanium isopropoxide as a precursor.[126] The doped TiO_2 nanocomposites will be synthesized similarly, by adding ferric nitrate ($Fe(NO_3)_3$) and silver nitrate ($AgNO_3$) to the TiO_2 precursor solution.[127] The Fe and Ag salts are combined in the desired proportion, ranging from 0 to 5 wt%, and the doped TiO_2 samples are allowed to precipitate. The nanoparticles are then calcined at 450°C for up to four hours. This method should result in nanocomposites that contain a mixture of anatase and rutile TiO_2 with Ag and/or FeOx incorporated within the framework of the compound, and will be designated as TiO_2, Ag(1-5)-TiO_2, FeOx(1-5)-TiO_2, and Ag(1-5)-FeOx(1-5)-TiO_2. Sample preparation is key in this step, since anatase is capable of transforming into rutile at high temperatures (around

600°C).[8,17] In fact, Fe is known to lower the anatase-to-rutile phase transformation (ART) temperature.[21,22,24,25]

Therefore, it is expected that the nanocomposites with higher Fe-oxide content will also have higher content of rutile which can ultimately affect the photocatalytic activity of the nanocomposite, since rutile is less photoactive than anatase.[8,12,13] The goal is to have silver and iron be well dispersed as dopants on the TiO_2.

Once all of the nanocomposites have been synthesized, they must be characterized, not only to verify that the correct nanoparticles have been created, but also to achieve a better understanding of the visible light absorption, structure, composition, and surface features of the nanocomposites. These properties will be monitored both in the bulk and on the surface, before and after photocatalytic reactions, to determine if there are any significant changes to the crystallinity or the number of active surface sites on the substrate.

5.4.1.1 Visible light absorption of the nanocomposites

Pure TiO_2 is only capable of absorbing UV light, and therefore it is of extreme importance to determine which of the synthesized Ag(0-5)-FeOx(0-5)-TiO_2 nanocomposites will absorb in the visible. During this phase of the research, the nanocomposites will be analyzed with diffuse reflectance UV-Vis spectroscopy (DR-UV-Vis), in order to collect the absorption spectrum. DR-UV-Vis is a very suitable technique to study opaque powdered samples and determine their spectral characteristics.[128] DR-UV-Vis will determine which combination of the Ag(0-5)-FeOx(0-5)-TiO_2 nanocomposites are optimal to maximize visible light absorption. Studies show that higher content of Ag or FeOx usually translates into more

dopants nanoparticles within the TiO_2, which maximizes the visible light absorption properties in the photocatalysts.[101,104,106] A recent study showed that the presence of both Ag nanoparticles and iron containing clay beads on TiO_2 presented enhanced visible light absorption compared to pure TiO_2 and Ag-TiO_2.[106] Therefore, it is expected that the synthesized Ag(1-5)-FeOx(1-5)-TiO_2 nanocomposites will experience higher intensity peaks in the visible region of the DR-UV-Vis spectra, over the pure TiO_2, Ag(1-5)-TiO_2 and Fe(1-5)-TiO_2 nanocomposites.

5.4.1.2 Crystallinity of the Ag-FeOx-TiO_2 nanocomposites

All the possible combinations of the different Ag(0-5)-FeOx(0-5)-TiO_2 nanocomposites that absorb light in the visible region (400-750 nm) will be chosen for the further characterization experiments. Raman spectroscopy will be utilized to identify the characteristic crystalline phases of the different nanocomposites. It is expected, that the photocatalysts will contain both anatase and rutile TiO_2, and the spectra for those titania polymorphs are well documented.[43,44] The characteristic Raman phonon peaks of anatase TiO_2 (144, 197, 396, 515 and 638 cm^{-1}) are very distinct from those of rutile TiO_2 (144, 236, 447 and 610 cm^{-1}).[1] In fact, a recent publication developed a mechanism to determine the percent composition of each crystalline phase in a sample.[1] With the help of this calibration method, it will be possible to determine the amount of anatase and rutile present in the nanocomposites. The Ag and FeOx content in the photocatalysts will be very low (0-5 wt%), and the Raman spectra of the doped-TiO_2 samples are expected to remain unchanged. However, in the case of higher content of the dopants, some peaks might appear in the

Raman spectra, especially for the FeOx, with Raman-active phonon peaks around 226, 245, 292, 299, 411, 498 and 612 cm^{-1}.[129] Some of the Raman peaks of the FeOx overlap with the characteristic peaks for anatase and rutile TiO_2, and due to the high content of TiO_2 the presence of the FeOx nanoparticles in the Raman spectrum might be difficult to identify. The peaks around 226-299 cm^{-1} are the most likely to be identified in the Raman spectra of the FeOx doped-TiO_2 samples. In the case of the Ag nanoparticles present in the nanocomposites, no peaks are likely to appear in the Raman spectra, since it is expected that these Ag nanoparticles are composed of elemental Ag and not AgOx.[101]

Similar to Raman spectroscopy, powdered x-ray diffraction (PXRD) can further verify the crystallinity of the doped-TiO_2 nanocomposites. Monitoring the crystal structure of the selected Ag-FeOx-TiO_2 photocatalysts as the amount of Ag and FeOx is increased from 0-5 wt% will provide valuable structural information for the system. It is expected that PXRD peaks characteristic to anatase (101, 004, 200, 105 and 211) and rutile (110, 101, 200, 111, 210, 211, 220) will appear in the spectrum of the synthesized TiO_2 nanocomposites.[19,26,76] Typically, the PXRD of doped-TiO_2 should remain unchanged since the dopant's concentrations are so low. However, in nanocomposites with high content of Ag and FeOx, some peaks characteristic of metallic Ag and FeOx nanoparticles might show up in the spectrum.[101,106] Additionally, using the Scherrer equation with the PXRD data from the Ag-FeOx-TiO_2 nanocomposites, it is possible to calculate the size of the nanoparticles, if the peaks are not broadened by the dopants.[104]

To further characterize the Ag-FeOx-TiO_2 nanocomposites, the surface area and pore size of the photocatalysts will be determined with a Brunauer-Emmett-Teller (BET) surface

area analyzer. These values are important for photocatalytic reactions because the higher the surface area the more active surface sites will be available for the photo-reactions to occur. It is expected that the pore size and surface area will change only slightly after co-precipitating the Ag and FeOx nanoparticles.[101] However, there is a chance that the dopants will be located inside the pore, which could interfere with the surface area and pore size. The topography and particles size of the Ag-FeOx-TiO_2 can also be observed and determined with the use of scanning electron microscopy (SEM). This analysis will provide insightful information on how the synthesized nanocomposites look and their size, complementing the PXRD data. It is more likely that Ag and FeOx nanoparticles will be distinguished from TiO_2 nanoparticles by SEM when the content of the dopants is higher, since the nanoparticles will be bigger in size compared to the lower concentration nanocomposites. However, the use of elemental analysis (EDX) in the SEM will help identify the presence of Ag and Fe in the samples. Even when the dopant's concentration is minimal, the EDX can identify it. In addition, elemental mapping can provide insightful information on how well dispersed the Ag and FeOx cocatalysts are dispersed in the nanocomposites.[104]

5.4.1.3 Surface activity of the Ag-Fe-TiO_2 nanocomposites

To verify the composition of the Ag-FeOx-TiO_2 nanocomposites and to analyze the oxidative states present on the surface, x-ray photoelectron spectroscopy (XPS) will be utilized. The XPS of TiO_2 typically shows peaks characteristic to the Ti^{4+} and O^{2-} states.[101,104,106] Studies of doped-TiO_2 with either Ag or FeOx show the appearance of peaks associated with the dopants. XPS is capable of identifying if the Ag present in the cocatalyst

is metallic silver or silver oxide, as well as distinguishing Fe(II) from Fe(III) in FeOx.[104,106] It is possible that the appearance of the peaks in the XPS spectra will be very broad and of low S/N, adding some difficulty to the identification of the oxidative states of the dopants. Most publications just report the XPS spectra of the synthesized nanoparticles, and it would be of great interest to determine the XPS spectra of the nanocomposites under visible light irradiation. Monitoring the changes of the XPS peaks of the as-synthesized nanocomposites while shining visible light might provide valuable information if the oxidative states of the components change or peaks disappear.

A series of studies has attempted to characterize the Ag-TiO_2, FeOx-TiO_2, or Ag-TiO_2 incorporated in Fe-containing beads nanocomposites using PXRD, XPS, and SEM.[101,102,104,106] However, there has been no attempt to identify the native features present on the surface, such as surface hydroxyls, which can play such a vital role in the surface chemistry during photocatalytic reactions. Therefore, a thorough DRIFTS study will allow for the identification of these features while adding much needed clarity to the identity and quantity of active sites present on the Ag-FeOx-TiO_2 composites. During this phase of the research project, close attention will be paid to the hydroxyl region of the DRIFTS spectrum (wavenumbers between 3750-3300 cm^{-1}) of the Ag-FeOx-TiO_2 composites to identify the possible hydroxyl reactive sites on the surface. On TiO_2 nanoparticles, surface hydroxyls are known to play a vital role in surface reactions.[100] In addition, they are known to facilitate the adsorption of the VOCs on the photocatalyst surface. Characterizing the surface hydroxyls that are bound to the surface of the Ag-FeOx-TiO_2 nanocomposites is a major step in understanding the active sites on the photocatalyst.

After characterizing the initial native surface hydroxyls on the surface of the as synthesized Ag-FeOx-TiO_2 nanocomposites, the next goal will be to characterize the hydroxyl features most affected by visible light irradiation by observing the shifts in band energies or intensities as a function light exposure. Observing these changes will provide insight about which hydroxyl features, if any, are removed from the surface by the visible light and in turn considered the most reactive sites. In the case that any surface hydroxyls were removed completely from the substrate, water vapor will be introduced at low pressures to re-hydroxylate the surface allowing the observation of the order in which the active sites of the nanocomposites react with water. Understanding the stability and reproducibility of the hydroxyl groups bound to the surface of the Ag-FeOx-TiO_2 nanocomposites while being exposed to light will clarify the properties of active surface sites.

5.4.2 Aim 2

Elucidate surface chemistry of the optimal TiO_2 nanocomposites during the reaction with acetaldehyde in the dark and as a function of relative humidity.

5.4.2.1 In situ DRIFTS surface chemistry investigation

Once the selected Ag-FeOx-TiO_2 nanocomposites are well characterized, the next aim of this research proposal will be to analyze their reaction with acetaldehyde in the dark. DRIFTS is frequently used to identify surface bound intermediates by observing fine details of the spectrum.[124] In addition, oxygen containing hydrocarbons are easy to differentiate via IR. During this surface chemistry investigation, the acetaldehyde will be introduced to the

reaction chamber containing the Ag-FeOx-TiO_2 nanocomposites at low pressures between 0.01-0.1 torr and allowed to equilibrate. While equilibrium is reached DRIFTS spectra will be collected frequently to observe the chemistry taking place on the surface of the nanocomposites. Identification of intermediate states formed on the surface occurs by monitoring the vibrational bands associated with functional groups present in the intermediate molecules.[124] Identifying the active sites, where the acetaldehyde molecule binds, will also be possible through the analysis of the DRIFTS spectrum, and as a result it is possible to state if the acetaldehyde is physisorbing or chemisorbing to the surface.

Some studies on the reaction of acetaldehyde with TiO_2 have claimed that it first reacts with the surface through the carbonyl group of the acetaldehyde. This is evidenced by a shift in the frequency of the characteristic carbonyl peak in the DRIFTS spectrum, which is usually around 1700 cm^{-1}. Then, the carbonyl peak disappears, and new bands are formed. Some studies report that acetaldehyde undergoes an aldol condensation on the TiO_2 surface, evidenced by the formation of 2-butenal i.e., crotonaldehyde.[130–132] Crotonaldehyde is formed by the dehydrogenation of intermediate 3-hydroxybutanal, which has also been reported in the FTIR spectrum of the reaction of acetaldehyde with TiO_2.[132,133] For the formation of crotonaldehyde, two adjacent acetaldehyde molecules are needed to be adsorbed on TiO_2 surface, which then react via an aldol condensation.[134] However, indoor air concentrations are too low to saturate the surface and the reaction between two adjacent acetaldehyde molecules is very unlikely. In the literature it is also proposed that acetaldehyde can be oxidized by defects on the TiO_2 surface and create a surface acetate species.[130–132] In the DRIFTS spectrum this can be seen as the presence of symmetric and asymmetric carboxylate

features, typically found in the wavenumbers between 1500-1300 cm^{-1}. Some studies suggest the formation of ethoxy species, which are a product of reduction of acetaldehyde on the TiO_2 surface through proton abstraction from a surface OH group.[135]

Clearly, there is varied information on how acetaldehyde reacts with TiO_2. Interestingly enough, in the studies performed on the PCO of ethanol with acetaldehyde as an intermediate, there is no evidence of acetaldehyde undergoing an aldol condensation, and the formation of crotonaldehyde on the surface of TiO_2. For studies proposed in this research proposal with Ag-FeOx-TiO_2 nanocomposites, similar surface species are expected to be found as on bare TiO_2. Because of the presence of the dopants, these features might be enhanced on specific surface sites, or might not appear at all.[135,136]

5.4.2.2 Transmission FTIR investigation

The reaction of acetaldehyde in the dark with the Ag-FeOx-TiO_2 nanocomposites will be performed in a gas cell to verify if any gas-phase products arise from the oxidation of acetaldehyde with surface active sites of the nanocomposites. The Ag-FeOx-TiO_2 nanocomposites will rest in a layer on the bottom of the transmission cell with the FTIR beam passing through, sampling the headspace above the photocatalyst. FTIR spectra will be collected frequently during introduction of acetaldehyde to identify any gas phase, IR active products as the reaction proceeds. It is expected that the acetaldehyde features in the gas-phase will decrease as the acetaldehyde adsorbs onto the surface of the nanocomposites. However, much acetaldehyde is likely to remain in the gas-phase.

5.4.2.3 Effect of relative humidity

Indoor air can be affected by external factors (air conditioning, rain, heat), which impact the relative humidity. It is therefore important to simulate the different relative humidity levels found indoors, where 5% being the lowest (dry conditions) and 70% the highest (damp conditions), during the reaction of acetaldehyde with the Ag-FeOx-TiO_2 nanocomposites. The characterization studies in Aim 1 will have allowed the understanding of the nature of the Ag-FeOx-TiO_2 nanocomposites hydroxylated surface. This knowledge can be used to selectively hydroxylate the substrate to mimic different relative humidity levels found in indoor air and monitor the surface *via in situ* DRIFTS when acetaldehyde is introduced into the reaction chamber. Since water is present in most photocatalytic oxidation reactions, it is important to understand the role of water during the reaction of acetaldehyde with the nanocomposites in the dark, in order to have initial information to compare it to when the PCO occurs.[100,137] It is thought that surface hydroxyls are important binding sites for the molecules, by which they can hydrogen bond to the surface and subsequently react with surface active sites. However, too much water can actually be disadvantageous, where water would take all the active sites by physisorbing or chemisorbing to the surface, leaving significantly fewer active sites for the adsorbates.[122,138] The monitoring of different levels of relative humidity will also be observed via transmission FTIR, to further understand any changes the reaction of acetaldehyde with the Ag-FeOx-TiO_2 nanocomposites undergoes as a function of the presence of water vapor.

After the meticulous surface characterization of the reaction of the Ag-FeOx-TiO_2 nanocomposites with acetaldehyde in the dark and as a function of relative humidity is well

understood, conclusions can be drawn about the influence Ag and FeOx nanoparticles, and relative humidity have on the acetaldehyde adsorption to the nanocomposite's surface, and the role each plays during the reaction in the dark. The results obtained during this stage of the research proposal are of extreme importance and will provide a reference point for the PCO of acetaldehyde under visible light.

5.4.3 Aim 3

Elucidate surface chemistry of the optimal TiO_2 nanocomposites during the photocatalytic oxidation of acetaldehyde as a function of visible light density and relative humidity.

5.4.3.1 In situ DRIFTS surface chemistry investigation

Once the reaction of acetaldehyde with the Ag-FeOx-TiO_2 nanocomposites in the dark is well characterized, visible light from white LEDs will be introduced to the system through a quartz window on the reaction chamber. Visible light has the potential to generate electrons and holes, as well as to activate the surface hydroxyl groups in the Ag-FeOx-TiO_2 nanocomposites, which are suggested to be a driving force of photocatalytic reactions.[71,75,77] The effect these photogenerated electrons and holes have on the PCO of acetaldehyde will be determined by observing the changes to the DRIFTS spectrum as the system is exposed to visible light of known energies for set amounts of time. Acetaldehyde will be introduced to the reaction chamber at low pressures between 0.01-0.1 torr and allowed to equilibrate. Once acetaldehyde has reacted with the surface in the dark and reached equilibrium, the white

LEDs will be turned on, and DRIFTS spectra will be collected until there are no more changes in the spectra. Ideally, H_2O and CO_2 are the only products of any PCO reaction. Bound CO_2 is typically found around 2300 cm^{-1} in the DRIFTS spectrum if it does not desorb from the surface. In the case of water, it can be recognized as physisorbed or chemisorbed water in the region of the OH stretching in the DRIFTS spectrum, around 3600-3000 cm^{-1}, and in the region of the HOH bend around 1600 cm^{-1}.[100] However, it is very likely that as the PCO progresses, the surface hydroxyls rearrange as they react with the adsorbed acetaldehyde, as well as the surface intermediate species that are formed from the PCO. Studies suggest the formation of acetic acid, formic acid, and formaldehyde as intermediates in the PCO of acetaldehyde over TiO_2, confirmed by GC or temperature programmed desorption (TPD). Based on this information, a study attempted to follow the reaction at the surface of TiO_2 and decipher the surface intermediates that lead to acetic acid, formic acid, and formaldehyde.[96] Upon UV light irradiation, FTIR spectra presented characteristic peaks of monodentate and bidentate formate features, evidenced by the symmetric and asymmetric stretches of COO^- peaks between 1500-1300 cm^{-1}.[72,96] Similarly, characteristic peaks for bidentate acetate features can be seen in the form of symmetric and asymmetric COO^- peaks between 1500-1400 cm^{-1}. In the case of formaldehyde, studies have shown that is an intermediate in the PCO of ethanol and is therefore expected to be an intermediate in the PCO of acetaldehyde. Hauchecorne et al. found unassigned monodentate formate features in the FTIR spectra during the PCO of acetaldehyde on TiO_2, namely symmetric and asymmetric COO^- around 1500-1300 cm^{-1}.[96] Ultimately, the authors confirmed that these formate features corresponded to adsorbed formaldehyde in the form of dioximethylene

(DOM). DOM is an intermediate in the adsorption mechanism of formaldehyde on TiO_2 and formate features in the form of symmetric and asymmetric COO^- are typically found around 1500-1300 cm^{-1}.[110,111,121] Hauchecorne et al. proposed a photocatalytic reaction mechanism, as seen in figure 2, where the initial surface intermediates, surface bound formate and acetate, were further photo-oxidized into monodentate formate. Ultimately, all surface formate features were photo-oxidized to CO_2.[96]

It is expected, that the PCO of acetaldehyde using the Ag-FeOx-TiO_2 nanocomposites with visible light irradiation will follow similar trends to the experiments found in the literature with pure TiO_2 and UV-light irradiation. In addition, doping the TiO_2 with Ag and FeOx nanoparticles should enhance the total mineralization of acetaldehyde under visible light irradiation. In general, there is mixed information on how acetaldehyde is photo-oxidized on the surface of pure TiO_2 in the literature. Surface species like acetates and formates are formed and, based on GC data or TPD, most studies suggest that common intermediates which desorb during the PCO of acetaldehyde are acetic acid, formic acid, and formaldehyde. The thorough DRIFTS analysis at this stage of the research proposal will provide a better understanding of the surface reactions occurring during the PCO of acetaldehyde with Ag-FeOx-TiO_2 during visible light irradiation. In addition, following the trend of variation of the intensity of characteristic bands of adsorbed acetaldehyde and the formed surface intermediates as a function of irradiated time, can give important information to propose a photocatalytic reaction mechanism and correlate the surface intermediates to formed products or by-products.

5.4.3.2 Transmission FTIR investigation

As in Aim 2, transmission FTIR investigations of the system during visible light irradiation will monitor the headspace over the photocatalysts for formation of IR-active products and by-products desorbed during the PCO of acetaldehyde using Ag-FeOx-TiO_2 nanocomposites under visible light irradiation. *In situ* FTIR papers refers to all the formed molecules as intermediates and GC data validates that those intermediates desorb from the surface. Therefore, these intermediates should be considered by-products of the PCO of acetaldehyde. That is why transmission FTIR investigations will provide insightful information regarding the formation of products and by-products. Upon visible light irradiation, it is expected that CO_2 and H_2O appear in the FTIR-spectra, as well as any desorbed by-products/intermediates. In addition, following the trend of variation of the relative intensities of the characteristic bands of these products or by-products, and correlating them with the time-dependent study of the *in situ* DRIFTS investigations of surface intermediates, will further provide invaluable information and help build a realistic photocatalytic reaction mechanism.

5.4.3.3 Effect of relative humidity

As stated earlier in Aim 2, a thorough analysis of the PCO of acetaldehyde with Ag-FeOx-TiO_2 nanocomposites as a function of different relative humidity levels is important to replicate the various conditions found in indoor air. That is why the *in situ* DRIFTS and transmission FTIR investigations will be monitored for different relative humidity levels ranging from dry conditions (5% RH) to wet conditions (70% RH). For example, the PCO of

acetaldehyde over P25 TiO_2 under UV-light irradiation was benefited by the presence of water vapor (it was very low in the absence of water), whereas the photocatalytic oxidation of ethanol in the same study with the same photocatalyst showed the opposite trend.[138] However, it has also been shown that under high humidity conditions (approx. 50% RH), acetaldehyde will desorb from the TiO_2 surface and be replaced with water molecules.[122]

5.4.3.4 Post reaction characterization

During photocatalysis, the Ag-FeOx-TiO_2 nanocomposites can experience many structural changes as surface bound hydroxyls are consumed and new oxygen vacancies or reduced Ti^{3+} are created. Once all experiments have been completed, the Ag-FeOx-TiO_2 nanocomposites will undergo a complete re-characterization as outline in Aim 1 to identify any changes in the photocatalyst.

5.4.3.5 Optimized Ag-FeOx-TiO_2 nanocomposite

Combining all of the data provided by this research proposal an optimized Ag-FeOx-TiO_2 nanocomposite can be identified. This analysis will also offer fundamental information on the conditions that are most beneficial for the PCO of acetaldehyde on the surface of Ag-FeOx-TiO_2 nanocomposites. By focusing on analyzing the surface chemistry of these transformations as a function of visible light density and relative humidity it will be determined how these variables either promote or hinder the different reactive sites on the Ag-FeOx-TiO_2 nanocomposites. The information obtained from these *in situ* studies of the surface chemistry of Ag-FeOx-TiO_2 nanocomposites will allow for the effective and efficient

use of these inexpensive materials as photocatalysts to abate indoor air pollutants using sunlight.

5.5 Intellectual Merit

Photocatalytic oxidation of indoor VOCs has been studied with TiO_2-based photocatalysts using UV-light irradiation. However, the main drawbacks of TiO_2 photocatalysts is the fast electron-hole recombination and the activation with UV-light, which constitutes only 5% of the solar light. Therefore, there is a need to modify the TiO_2 to hinder as much a possible the electron-hole recombination and broaden the light absorbance capability into the visible light region. This research proposal targets these two variables by doping the TiO_2 with Ag and FeOx nanoparticles, to create the novel visible-light-absorbing Ag-FeOx-TiO_2 nanocomposites, where Ag and FeOx will allow for visible light absorption, enhance the electron-hole separation, and provide more reaction sites to ultimately better the photocatalytic activity. In addition, the thorough *in situ* surface investigation using DRIFTS in combination with transmission FTIR will help to fill the holes missing from the literature to better understand the reactions happening in the surface, as well as in the gas-phase, that will ultimately allow to propose realistic reaction mechanisms with the main goal of illustrating that efficient visible-light-absorbing photocatalysts are able to photodegrade VOCs found in indoor air.

5.6 Broader impacts of the proposed work

The novel Ag-FeOx-TiO_2 nanocomposites proposed in this research project are very cost-effective and able to phototactically oxidize many indoor air pollutants with visible light coming from the windows and indoor lights. These nanocomposites can be scaled up and produced in large quantities to be used in the treatment of air purification systems in industry, office spaces and even homes. By incorporating these nanocomposites as a layer over paints or furniture materials, for example, the versatile Ag-FeOx-TiO_2 nanocomposites will be able to photodegrade indoor air VOCs into harmless products, such as H_2O and CO_2. This has the potential to impact people's health, by making indoor environments safe from any harmful chemicals, so that people can be comfortable and breathe cleaner air.

REFERENCES

(1) Labadini, D.; Hafiz, S. S.; Huttunen, P. K.; Wolff, E. P.; Vasilakis, C.; Foster, M. Visualization and Quantification of the Laser-Induced ART of TiO2 by Photoexcitation of Adsorbed Dyes. *Langmuir* **2020**, *36*, 1651–1661.

(2) Kapilashrami, M.; Zhang, Y.; Liu, Y. S.; Hagfeldt, A.; Guo, J. Probing the Optical Property and Electronic Structure of TiO2 Nanomaterials for Renewable Energy Applications. *Chem. Rev.* **2014**, *114* (19), 9662–9707.

(3) Gong, J.; Liang, J.; Sumathy, K. Review on Dye-Sensitized Solar Cells (DSSCs): Fundamental Concepts and Novel Materials. *Renew. Sustain. Energy Rev.* **2012**, *16* (8), 5848–5860.

(4) O'Regan, B.; Grätzel, M. A Low-Cost, High-Efficiency Solar Cell Based on Dye-Sensitized Colloidal TiO2 Films. *Nature* **1991**, *353*, 737–739.

(5) Gierszewski, M.; Glinka, A.; Grądzka, I.; Gierczyk, B.; Ziółek, M. Testing New Concepts in Solar Cells Sensitized with Indoline Dyes - Alkoxysilyl Anchoring Group, Molecular Capping, and Cobalt-Based Electrolyte. *J. Phys. Chem. C* **2018**, *122* (45), 25764–25775.

(6) Mbonyiryivuze, A. Titanium Dioxide Nanoparticles Biosynthesis for Dye Sensitized Solar Cells Application: Review. *Phys. Mater. Chem.* **2015**, *3* (1).

(7) Thomas, S.; Mamour Sakho, E. H.; Kalarikkal, N.; Oluwafemi, O. S.; Wu, J. *Nanomaterials for Solar Cell Applications*; Elsevier: San Diego, UNITED STATES, 2019.

(8) Hanaor, D. A. H.; Sorrell, C. C. Review of the Anatase to Rutile Phase Transformation. *J. Mater. Sci.* **2011**, *46* (4), 855–874.

(9) Mosquera, A. A.; Albella, J. M.; Navarro, V.; Bhattacharyya, D.; Endrino, J. L. Effect of Silver on the Phase Transition and Wettability of Titanium Oxide Films. *Sci. Rep.* **2016**, *6* (July), 1–14.

(10) Ni, M.; Leung, M. K. H.; Leung, D. Y. C.; Sumathy, K. A Review and Recent Developments in Photocatalytic Water-Splitting Using TiO2 for Hydrogen Production. *Renew. Sustain. Energy Rev.* **2007**, *11* (3), 401–425.

(11) Thompson, T. L.; Yates, J. T. Surface Science Studies of the Photoactivation of TiO2 - New Photochemical Processes. *Chem. Rev.* **2006**, *106* (10), 4428–4453.

(12) Schneider, J.; Matsuoka, M.; Takeuchi, M.; Zhang, J.; Horiuchi, Y.; Anpo, M.; Bahnemann, D. W. Understanding TiO2 Photocatalysis : Mechanisms and Materials. *Chem. Rev.* **2014**, *114* (2014 Titanium Dioxide Nanomaterials), 9919–9986.

(13) Pelaez, M.; Nolan, N. T.; Pillai, S. C.; Seery, M. K.; Falaras, P.; Kontos, A. G.; Dunlop, P. S. M.; Hamilton, J. W. J.; Byrne, J. A.; O'Shea, K.; et al. A Review on the Visible Light Active Titanium Dioxide Photocatalysts for Environmental Applications. *Appl. Catal. B Environ.* **2012**, *125*, 331–349.

(14) Kafizas, A.; Carmalt, C. J.; Parkin, I. P. Does a Photocatalytic Synergy in an Anatase-Rutile TiO2 Composite Thin-Film Exist? *Chem. - A Eur. J.* **2012**, *18* (41), 13048–13058.

(15) Parussulo, A. L. A.; Bonacin, J. A.; Toma, S. H.; Araki, K.; Toma, H. E. Unravelling the Chemical Morphology of a Mesoporous Titanium Dioxide Interface by Confocal Raman Microscopy: New Clues for Improving the Efficiency of Dye Solar Cells and Photocatalysts. *Langmuir* **2009**, *25* (19), 11269–11271.
(16) Ricci, P. C.; Carbonaro, C. M.; Stagi, L.; Salis, M.; Casu, A.; Enzo, S.; Delogu, F. Anatase-to-Rutile Phase Transition in TiO2 Nanoparticles Irradiated by Visible Light. *J. Phys. Chem. C* **2013**, *117* (15), 7850–7857.
(17) Zhang, J.; Li, M.; Feng, Z.; Chen, J.; Li, C. UV Raman Spectroscopic Study on TiO2. I. Phase Transformation at the Surface and in the Bulk. *J. Phys. Chem. B* **2006**, *110* (2), 927–935.
(18) Mathpal, M. C.; Tripathi, A. K.; Singh, M. K.; Gairola, S. P.; Pandey, S. N.; Agarwal, A. Effect of Annealing Temperature on Raman Spectra of TiO 2 Nanoparticles. *Chem. Phys. Lett.* **2013**, *555*, 182–186.
(19) Tripathi, A. K.; Singh, M. K.; Mathpal, M. C.; Mishra, S. K.; Agarwal, A. Study of Structural Transformation in TiO2 Nanoparticles and Its Optical Properties. *J. Alloys Compd.* **2013**, *549*, 114–120.
(20) Nakaruk, A.; Lin, C. Y.; Perera, D. S.; Sorrell, C. C. Effect of Annealing Temperature on Titania Thin Films Prepared by Spin Coating. *J. Sol-Gel Sci. Technol.* **2010**, *55* (3), 328–334.
(21) Gaur, L. K.; Kumar, P.; Kushavah, D.; Khiangte, K. R.; Mathpal, M. C.; Agrahari, V.; Gairola, S. P.; Soler, M. A. G.; Swart, H. C.; Agarwal, A. Laser Induced Phase Transformation Influenced by Co Doping in TiO2 Nanoparticles. *J. Alloys Compd.* **2019**, *780*, 25–34.
(22) Camacho-López, M. A.; Vargas, S.; Arroyo, R.; Haro-Poniatowski, E.; Rodríguez, R. Raman Studies on Laser Induced Crystallization of Co(II) Doped Titania; Effect of the Dopant Concentration. *Opt. Mater. (Amst).* **2002**, *20* (1), 43–50.
(23) Byrne, C.; Moran, L.; Hermosilla, D.; Merayo, N.; Blanco, Á.; Rhatigan, S.; Hinder, S.; Ganguly, P.; Nolan, M.; Pillai, S. C. Effect of Cu Doping on the Anatase-to-Rutile Phase Transition in TiO2 Photocatalysts: Theory and Experiments. *Appl. Catal. B Environ.* **2019**, *246* (December 2018), 266–276.
(24) Vásquez, G. C.; Peche-Herrero, M. A.; Maestre, D.; Gianoncelli, A.; Ramírez-Castellanos, J.; Cremades, A.; González-Calbet, J. M.; Piqueras, J. Laser-Induced Anatase-to-Rutile Transition in TiO2 Nanoparticles: Promotion and Inhibition Effects by Fe and Al Doping and Achievement of Micropatterning. *J. Phys. Chem. C* **2015**, *119* (21), 11965–11974.
(25) Lee, H. Y.; Lan, W. L.; Tseng, T. Y.; Hsu, D.; Chang, Y. M.; Lin, J. G. Optical Control of Phase Transformation in Fe-Doped TiO2 Nanoparticles. *Nanotechnology* **2009**, *20* (31), 1–5.
(26) Mathpal, M. C.; Tripathi, A. K.; Kumar, P.; Balasubramaniyan, R.; Singh, M. K.; Chung, J. S.; Hur, S. H.; Agarwal, A. Polymorphic Transformations and Optical Properties of Graphene-Based Ag-Doped Titania Nanostructures. *Phys. Chem. Chem. Phys.* **2014**, *16* (43), 23874–23883.

(27) Stagi, L.; Carbonaro, C. M.; Corpino, R.; Chiriu, D.; Ricci, P. C. Light Induced TiO2 Phase Transformation: Correlation with Luminescent Surface Defects. *Phys. Status Solidi Basic Res.* **2015**, *252* (1), 124–129.
(28) Ricci, P. C.; Casu, A.; Salis, M.; Corpino, R.; Anedda, A. Optically Controlled Phase Variation of TiO2 Nanoparticles. *J. Phys. Chem. C* **2010**, *114* (34), 14441–14445.
(29) Long, H.; Yang, G.; Chen, A.; Li, Y.; Lu, P. Growth and Characteristics of Laser Deposited Anatase and Rutile TiO2 Films on Si Substrates. *Thin Solid Films* **2008**, *517* (2), 745–749.
(30) Zhao, L.; Han, M.; Lian, J. Photocatalytic Activity of TiO2 Films with Mixed Anatase and Rutile Structures Prepared by Pulsed Laser Deposition. *Thin Solid Films* **2008**, *516* (10), 3394–3398.
(31) Benavides, J. A.; Trudeau, C. P.; Gerlein, L. F.; Cloutier, S. G. Laser Selective Photoactivation of Amorphous " 2 Films to Anatase and/or Rutile Crystalline Phases. *ACS Appl. Energy Mater.* **2018**, *1* (8), 3607–3613.
(32) Chatterjee, A.; Wu, S. B.; Chou, P. W.; Wong, M. S.; Cheng, C. L. Observation of Carbon-Facilitated Phase Transformation of Titanium Dioxide Forming Mixed-Phase Titania by Confocal Raman Microscopy. *J. Raman Spectrosc.* **2011**, *42* (5), 1075–1080.
(33) Parussulo, A. L. A.; Huila, M. F. G.; Araki, K.; Toma, H. E. N3-Dye-Induced Visible Laser Anatase-to-Rutile Phase Transition on Mesoporous TiO2 Films. *Langmuir* **2011**, *27* (15), 9094–9099.
(34) Grätzel, M. Solar Energy Conversion by Dye-Sensitized Photovoltaic Cells. *Inorg. Chem.* **2005**, *44* (20), 6841–6851.
(35) Novir, S. B.; Hashemianzadeh, S. M. Computational Study of New Azo Dyes with Different Anchoring Groups for Dye-Sensitised Solar Cells. *Mol. Phys.* **2016**, *114* (5), 650–662.
(36) Robertson, N. Optimizing Dyes for Dye-Sensitized Solar Cells. *Angew. Chemie - Int. Ed.* **2006**, *45* (15), 2338–2345.
(37) Lee, K. E.; Gomez, M. A.; Elouatik, S.; Demopoulos, G. P. Further Understanding of the Adsorption Mechanism of N719 Sensitizer on Anatase TiO2 Films for DSSC Applications Using Vibrational Spectroscopy and Confocal Raman Imaging. *Langmuir* **2010**, *26* (12), 9575–9583.
(38) Pérez León, C.; Kador, L.; Peng, B.; Thelakkat, M. Characterization of the Adsorption of Ru-Bpy Dyes on Mesoporous TiO2 Films with UV-Vis, Raman, and FTIR Spectroscopies. *J. Phys. Chem. B* **2006**, *110* (17), 8723–8730.
(39) Stergiopoulos, T.; Bernard, M. C.; Hugot-Le Goff, A.; Falaras, P. Resonance Micro-Raman Spectrophotoelectrochemistry on Nanocrystalline TiO2 Thin Film Electrodes Sensitized by Ru(II) Complexes. *Coord. Chem. Rev.* **2004**, *248* (13–14), 1407–1420.
(40) Khazraji, A. C.; Hotchandani, S.; Das, S.; Kamat, P. V. Controlling Dye (Merocyanine-540) Aggregation on Nanostructured TiO2 Films. An Organized Assembly Approach for Enhancing the Efficiency of Photosensitization. *J. Phys. Chem. B* **1999**, *103* (22), 4693–4700.

(41) Benniston, A. C.; Matousek, P.; McCulloch, I. E.; Parker, A. W.; Towrie, M. Detailed Picosecond Kerr-Gated Time-Resolved Resonance Raman Spectroscopy and Time-Resolved Emission Studies of Merocyanine 540 in Various Solvents. *J. Phys. Chem. A* **2003**, *107* (22), 4347–4353.
(42) Clegg, I. M.; Everall, N. J.; King, B.; Melvin, H.; Norton, C. On-Line Analysis Using Raman Spectroscopy for Process Control during the Manufacture of Titanium Dioxide. *Appl. Spectrosc.* **2001**, *55* (9), 1138–1150.
(43) Zhang, Y.; Wu, W.; Zhang, K.; Liu, C.; Yu, A.; Peng, M.; Zhai, J. Raman Study of 2D Anatase TiO2 Nanosheets. *Phys. Chem. Chem. Phys.* **2016**, *18* (47), 32178–32184.
(44) Zhang, W. F.; He, Y. L.; Zhang, M. S.; Yin, Z.; Chen, Q. Raman Scattering Study on Anatase TiO2 Nanocrystals. *J. Phys. D. Appl. Phys.* **2000**, *33* (8), 912–916.
(45) Zhang, Y.; Harris, C. X.; Wallenmeyer, P.; Murowchick, J.; Chen, X. Asymmetric Lattice Vibrational Characteristics of Rutile TiO2 as Revealed by Laser Power Dependent Raman Spectroscopy. *J. Phys. Chem. C* **2013**, *117* (45), 24015–24022.
(46) Gouadec, G.; Colomban, P. Raman Spectroscopy of Nanomaterials: How Spectra Relate to Disorder, Particle Size and Mechanical Properties. *Prog. Cryst. Growth Charact. Mater.* **2007**, *53* (1), 1–56.
(47) Sundius, T. Computer Fitting of Voigt Profiles to Raman Lines. *Journal of Raman Spectroscopy*. 1973, pp 471–488.
(48) Muñoz Tabares, J. A.; Anglada, M. J. Quantitative Analysis of Monoclinic Phase in 3Y-TZP by Raman Spectroscopy. *J. Am. Ceram. Soc.* **2010**, *93* (6), 1790–1795.
(49) Zanatta, A. R. A Fast-Reliable Methodology to Estimate the Concentration of Rutile or Anatase Phases of TiO2. *AIP Adv.* **2017**, *7* (7).
(50) Nazeeruddin, M. K.; Zakeeruddin, S. M.; Humphry-Baker, R.; Jirousek, M.; Liska, P.; Vlachopoulos, N.; Shklover, V.; Fischer, C. H.; Grätzel, M. Acid-Base Equilibria of (2,2′-Bipyridyl-4,4′-Dicarboxylic Acid)Ruthenium(II) Complexes and the Effect of Protonation on Charge-Transfer Sensitization of Nanocrystalline Titania. *Inorg. Chem.* **1999**, *38* (26), 6298–6305.
(51) Greijer, H.; Lindgren, J.; Hagfeldt, A. Resonance Raman Scattering of a Dye-Sensitized Solar Cell: Mechanism of Thiocyanato Ligand Exchange. *J. Phys. Chem. B* **2001**, *105* (27), 6314–6320.
(52) Mazza, T.; Barborini, E.; Piseri, P.; Milani, P.; Cattaneo, D.; Li Bassi, A.; Bottani, C. E.; Ducati, C. Raman Spectroscopy Characterization of TiO2 Rutile Nanocrystals. *Phys. Rev. B - Condens. Matter Mater. Phys.* **2007**, *75* (4), 1–5.
(53) Merle, P.; Pascual, J.; Camassel, J.; Mathieu, H. Uniaxial-Stress Dependence of the First-Order Raman Spectrum of Rutile. I. Experiments. *Phys. Rev. B* **1980**, *21* (4), 1617–1626.
(54) Zhao, H. C.; Harney, J. P.; Huang, Y.-T.; Yum, J.-H.; Nazeeruddin, M. K.; Grätzel, M.; Tsai, M.-K.; Rochford, J. Evaluation of a Ruthenium Oxyquinolate Architecture for Dye-Sensitized Solar Cells. *Inorg. Chem.* **2012**, *51* (1), 1–3.
(55) De Angelis, F.; Fantacci, S.; Mosconi, E.; Nazeeruddin, M. K.; Grätzel, M. Absorption Spectra and Excited State Energy Levels of the N719 Dye on TiO2 in Dye-Sensitized Solar Cell Models. *J. Phys. Chem. C* **2011**, *115* (17), 8825–8831.

(56) Nazeeruddin, M. K.; Humphry-Baker, R.; Liska, P.; Grätzel, M. Investigation of Sensitizer Adsorption and the Influence of Protons on Current and Voltage of a Dye-Sensitized Nanocrystalline TiO2 Solar Cell. *J. Phys. Chem. B* **2003**, *107* (34), 8981–8987.
(57) Fakis, M.; Stathatos, E.; Tsigaridas, G.; Giannetas, V.; Persephonis, P. Femtosecond Decay and Electron Transfer Dynamics of the Organic Sensitizer D149 and Photovoltaic Performance in Quasi-Solid-State Dye-Sensitized Solar Cells. *J. Phys. Chem. C* **2011**, *115* (27), 13429–13437.
(58) Oum, K.; Lohse, P. W.; Flender, O.; Klein, J. R.; Scholz, M.; Lenzer, T.; Du, J.; Oekermann, T. Ultrafast Dynamics of the Indoline Dye D149 on Electrodeposited ZnO and Sintered ZrO2 and TiO2 Thin Films. *Phys. Chem. Chem. Phys.* **2012**, *14* (44), 15429–15437.
(59) Suto, K.; Konno, A.; Kawata, Y.; Tasaka, S.; Sugita, A. Adsorption Dynamics of the N719 Dye on Nanoporous Titanium Oxides Studied by Resonance Raman Scattering and Fourier Transform Infrared Spectroscopy. *Chem. Phys. Lett.* **2012**, *536*, 45–49.
(60) Bae, E.; Choi, W.; Park, J.; Shin, H. S.; Kim, S. Bin; Lee, J. S. Effects of Surface Anchoring Groups (Carboxylate vs Phosphonate) in Ruthenium-Complex-Sensitized TiO2 on Visible Light Reactivity in Aqueous Suspensions. *J. Phys. Chem. B* **2004**, *108* (37), 14093–14101.
(61) Stylidi, M.; Kondarides, D. I.; Verykios, X. E. Pathways of Solar Light-Induced Photocatalytic Degradation of Azo Dyes in Aqueous TiO2 Suspensions. *Appl. Catal. B Environ.* **2003**, *40* (4), 271–286.
(62) Bandara, J.; Mielczarski, J. A.; Kiwi, J. 1. Molecular Mechanism of Surface Recognition. Azo Dyes Degradation on Fe, Ti, and Al Oxides through Metal Sulfonate Complexes. *Langmuir* **1999**, *15* (22), 7670–7679.
(63) Bourikas, K.; Stylidi, M.; Kondarides, D. I.; Verykios, X. E. Adsorption of Acid Orange 7 on the Surface of Titanium Dioxide. *Langmuir* **2005**, *21* (20), 9222–9230.
(64) Bauer, C.; Jacques, P.; Kalt, A. Investigation of the Interaction between a Sulfonated Azo Dye (AO7) and a TiO2 Surface. *Chem. Phys. Lett.* **1999**, *307* (5–6), 397–406.
(65) Hagfeldt, A.; Boschloo, G.; Sun, L.; Kloo, L.; Pettersson, H. Dye-Sensitized Solar Cells. *Chem. Rev.* **2010**, *110* (11), 6595–6663.
(66) Abidi, M.; Assadi, A. A.; Bouzaza, A.; Hajjaji, A.; Bessais, B.; Rtimi, S. Photocatalytic Indoor/Outdoor Air Treatment and Bacterial Inactivation on CuxO/TiO2 Prepared by HiPIMS on Polyester Cloth under Low Intensity Visible Light. *Appl. Catal. B Environ.* **2019**, *259* (118074), 1–8.
(67) Mamaghani, A. H.; Haghighat, F.; Lee, C. Photocatalytic Oxidation Technology for Indoor Environment Air Purification: The State-of-the-Art. *Appl. Catal. B Environ.* **2017**, *203*, 247–269.
(68) Davamani, V.; Deepasri, M.; Parameswari, E.; Arulmani, S.; Sebastian, S. P.; Ilakia, T. Chemistry of Indoor Pollutants and Their Impacts on Human Health. *Int. Res. J. Pure Appl. Chem.* **2020**, *21* (9), 40–61.
(69) Escobedo, S.; Lasa, H. de. Photocatalysis for Air Treatment Processes: Current Technologies and Future Applications for the Removal of Organic Pollutants and Viruses. *Catalysts* **2020**, *10* (9), 1–38.

(70) Weon, S.; He, F.; Choi, W. Status and Challenges in Photocatalytic Nanotechnology for Cleaning Air Polluted with Volatile Organic Compounds: Visible Light Utilization and Catalyst Deactivation. *Environ. Sci. Nano* **2019**, *6* (11), 3185–3214.
(71) Ohtani, B. Photocatalysis A to Z-What We Know and What We Do Not Know in a Scientific Sense. *J. Photochem. Photobiol. C Photochem. Rev.* **2010**, *11* (4), 157–178.
(72) Hauchecorne, B.; Lenaerts, S. Unravelling the Mysteries of Gas Phase Photocatalytic Reaction Pathways by Studying the Catalyst Surface : A Literature Review of Different Fourier Transform Infrared Spectroscopic Reac. *J. Photochem. Photobiol. C Photochem. Rev.* **2013**, *14*, 72–85.
(73) Sang, L.; Zhao, Y.; Burda, C. TiO 2 Nanoparticles as Functional Building Blocks. **2014**.
(74) Kapilashrami, M.; Zhang, Y.; Liu, Y. S.; Hagfeldt, A.; Guo, J. Probing the Optical Property and Electronic Structure of TiO2nanomaterials for Renewable Energy Applications. *Chem. Rev.* **2014**, *114* (19), 9662–9707.
(75) Schneider, J.; Matsuoka, M.; Takeuchi, M.; Zhang, J.; Horiuchi, Y.; Anpo, M.; Bahnemann, D. W. Understanding TiO2photocatalysis: Mechanisms and Materials. *Chem. Rev.* **2014**, *114* (19), 9919–9986.
(76) Fujishima, A.; Zhang, X.; Tryk, D. A. TiO2 Photocatalysis and Related Surface Phenomena. *Surf. Sci. Rep.* **2008**, *63* (12), 515–582.
(77) Henderson, M. A. A Surface Science Perspective on TiO2 Photocatalysis. *Surf. Sci. Rep.* **2011**, *66* (6–7), 185–297.
(78) Guo, Q.; Zhou, C.; Ma, Z.; Yang, X. Fundamentals of TiO2 Photocatalysis: Concepts, Mechanisms, and Challenges. *Adv. Mater.* **2019**, *31* (50), 1–26.
(79) Hernández-Alonso, M. D.; Fresno, F.; Suárez, S.; Coronado, J. M. Development of Alternative Photocatalysts to TiO2: Challenges and Opportunities. *Energy Environ. Sci.* **2009**, *2* (12), 1231–1257.
(80) Wen, J.; Li, X.; Liu, W.; Fang, Y.; Xie, J.; Xu, Y. Photocatalysis Fundamentals and Surface Modification of TiO 2 Nanomaterials. *Chinese J. Catal.* **2015**, *36* (12), 2049–2070.
(81) Meng, A.; Zhang, L.; Cheng, B.; Yu, J. Dual Cocatalysts in TiO2 Photocatalysis. *Adv. Mater.* **2019**, *31* (1807660), 1–31.
(82) Wang, F.; Jiang, Y.; Lawes, D. J.; Ball, G. E.; Zhou, C.; Liu, Z.; Amal, R. Analysis of the Promoted Activity and Molecular Mechanism of Hydrogen Production over Fine Au-Pt Alloyed TiO2 Photocatalysts. *ACS Catalysis*. 2015, pp 3924–3931.
(83) Melvin, A. A.; Illath, K.; Das, T.; Raja, T.; Bhattacharyya, S.; Gopinath, C. S. M-Au/TiO2 (M = Ag, Pd, and Pt) Nanophotocatalyst for Overall Solar Water Splitting: Role of Interfaces. *Nanoscale* **2015**, *7* (32), 13477–13488.
(84) Shuang, S.; Lv, R.; Xie, Z.; Zhang, Z. Surface Plasmon Enhanced Photocatalysis of Au/Pt-Decorated TiO2 Nanopillar Arrays. *Sci. Rep.* **2016**, *6* (May), 1–8.
(85) Tanaka, A.; Nishino, Y.; Sakaguchi, S.; Yoshikawa, T.; Imamura, K.; Hashimoto, K.; Kominami, H. Functionalization of a Plasmonic Au/TiO2 Photocatalyst with an Ag Co-Catalyst for Quantitative Reduction of Nitrobenzene to Aniline in 2-Propanol Suspensions under Irradiation of Visible Light. *Chem. Commun.* **2013**, *49* (25), 2551–2553.

(86) Zhao, Y.; Tao, C.; Xiao, G.; Wei, G.; Li, L.; Liu, C.; Su, H. Controlled Synthesis and Photocatalysis of Sea Urchin-like Fe3O4@TiO2@Ag Nanocomposites. *Nanoscale* **2016**, *8* (9), 5313–5326.
(87) Liu, C.; Tong, R.; Xu, Z.; Kuang, Q.; Xie, Z.; Zheng, L. Efficiently Enhancing the Photocatalytic Activity of Faceted TiO2 Nanocrystals by Selectively Loading A-Fe2O3 and Pt Co-Catalysts†. *RSC Adv.* **2016**, *6* (35), 29794–29801.
(88) Nath, R. K.; Zain, M. F. M.; Jamil, M. An Environment-Friendly Solution for Indoor Air Puri Fi Cation by Using Renewable Photocatalysts in Concrete: A Review. *Renew. Sustain. Energy Rev.* **2016**, *62*, 1184–1194.
(89) Tai, X. H.; Lai, C. W.; Juan, J. C.; Lee, K. M. *Nano-Photocatalyst in Photocatalytic Oxidation Processes*; 2020.
(90) Matos, J.; Garcia, A.; Chovelon, J. M.; Ferronato, C. Combination of Adsorption on Activated Carbon and Oxidative Photocatalysis on TiO2 for Gaseous Toluene Remediation. *Open Mater. Sci. J.* **2010**, *4*, 23–25.
(91) Wang, M.; Lawal, A.; Stephenson, P.; Sidders, J.; Ramshaw, C. Post-Combustion CO2 Capture with Chemical Absorption: A State-of-the-Art Review. *Chem. Eng. Res. Des.* **2011**, *89*, 1609–1624.
(92) Aymen Amine, A.; Bouzaza, A.; Soutrel, I.; Petit, P.; Medimagh, K.; Wolbert, D. A Study of Pollution Removal in Exhaust Gases from Animal Quartering Centers by Combining Photocatalysis with Surface Discharge Plasma: From Pilot to Industrial Scale. *Chem. Eng. Process. Process Intensif.* **2017**, *111*, 1–6.
(93) Assadi, A. A.; Bouzaza, A.; Vallet, C.; Wolbert, D. Use of DBD Plasma, Photocatalysis, and Combined DBD Plasma/Photocatalysis in a Continuous Annular Reactor for Isovaleraldehyde Elimination – Synergetic Effect and Byproducts Identification. *Chem. Eng. J.* **2014**, *254*, 124–132.
(94) Maxime, G.; Amine, A. A.; Bouzaza, A.; Wolbert, D. Removal of Gas-Phase Ammonia and Hydrogen Sulfide Using Photocatalysis, Nonthermal Plasma, and Combined Plasma and Photocatalysis at Pilot Scale. *Environ. Sci. Pollut. Res.* **2014**, *21*, 13127–13137.
(95) Boeniger, M. F. Use of Ozone Generating Devices to Improve Indoor Air Quality. *Am. Ind. Hyg. Assoc. J.* **1995**, *56* (6), 590–598.
(96) Hauchecorne, B.; Terrens, D.; Verbruggen, S.; Martens, J. A.; Langenhove, H. Van; Demeestere, K.; Lenaerts, S. Elucidating the Photocatalytic Degradation Pathway of Acetaldehyde: An FTIR in Situ Study under Atmospheric Conditions. *Appl. Catal. B Environ.* **2011**, *106*, 630–638.
(97) Meroni, D.; Ardizzone, S.; Cappelletti, G.; Oliva, C.; Ceotto, M.; Poelman, D.; Poelman, H. Photocatalytic Removal of Ethanol and Acetaldehyde by N-Promoted TiO2 Films: The Role of the Different Nitrogen Sources. *Catal. Today* **2011**, *161*, 169–174.
(98) Lin, H.; Ye, Q.; Deng, C.; Zhang, X. Field Analysis of Acetaldehyde in Mainstream Tobacco Smoke Using Solid-Phase Microextraction and a Portable Gas Chromatograph. *J. Chromatogr. A* **2008**, *1198–1199*, 34–37.
(99) Guo, Q.; Ma, Z.; Zhou, C.; Ren, Z.; Yang, X. Single Molecule Photocatalysis on TiO2 Surfaces. *Chem. Rev.* **2019**, *119* (20), 11020–11041.

(100) Kipreos, M. D.; Foster, M. Water Interactions on the Surface of 50 Nm Rutile TiO2 Nanoparticles Using in Situ DRIFTS. *Surf. Sci.* **2018**, *677*, 1–7.
(101) Jiang, X.; Xu, W.; Yu, L. Photocatalytic Decomposition of Gaseous HCHO over Ag Modified TiO2 Nanosheets at Ambient Temperature. *Nanomaterials* **2019**, *9* (338), 1–14.
(102) Luna, M. D. G. De; Laciste, M. T.; Tolosa, N. C.; Lu, M. Effect of Catalyst Calcination Temperature in the Visible Light Photocatalytic Oxidation of Gaseous Formaldehyde by Multi-Element Doped Titanium Dioxide. *Environ. Sci. Pollut. Res.* **2018**, *25*, 15216–15225.
(103) Balbuena, J.; Carraro, G.; Cruz, M.; Gasparotto, A.; Maccato, C.; Pastor, A.; Sada, C.; Barreca, D.; Sanchez, L. Advances in Photocatalytic NOx Abatement through the Use of Fe2O3/TiO2 Nanocomposites. *RSC Adv.* **2016**, *6*, 74878–74885.
(104) Saqlain, S.; Cha, B. J.; Kim, S. Y.; Ahn, T. K.; Park, C.; Oh, J.-M.; Jeong, E. C.; Seo, H. O.; Kim, Y. D. Visible Light-Responsive Fe-Loaded TiO2 Photocatalysts for Total Oxidation of Acetaldehyde: Fundamental Studies towards Large-Scale Production and Applications. *Appl. Surf. Sci.* **2020**, *505* (144160), 1–9.
(105) Liu, Y.; Xu, G.; Lv, H. Ag Modified Fe-Doping TiO2 Nanoparticles and Nanowires with Enhanced Photocatalytic Activities for Hydrogen Production and Volatile Organic Pollutant Degradation. *J. Mater. Sci. Mater. Electron.* **2018**, *29*, 10504–10516.
(106) Bansal, P.; Verma, A. Applications of Sunlight Responsive Fe-Ag-TiO2 Composite Incorporating in-Situ Dual Effect for the Degradation of Pentoxifylline. *Mater. Sci. Eng. B* **2018**, *236–237*, 197–207.
(107) Esmaeili, N.; Pirbazari, A. E.; Khodaee, Z. Visible-Light Active and Magnetically Recyclable Ag-Coated Fe3o4/Tio2 Nanocomposites for Efficient Photocatalytic Oxidation of 2,4-Dichlorophenol. *Desalin. Water Treat.* **2018**, *114*, 251–264.
(108) Ubolchonlakate, K.; Sikong, L.; Tontai, T. Formaldehyde Degradation by Photocatalytic Ag-Doped TiO2 Film of Glass Fiber Roving. *J. Nanosci. Nanotechnol.* **2010**, *10*, 7522–7525.
(109) Obuchi, E.; Sakamoto, T.; Nakano, K. Photocatalytic Decomposition of Acetaldehyde over TiO2/SiO2 Catalyst. *Chem. Eng. Sci.* **1999**, *54*, 1525–1530.
(110) Sauer, M. L.; Ollis, D. F. Photocatalyzed Oxidation of Ethanol and Acetaldehyde in Humidified Air. *J. Catal.* **1996**, *158* (0055), 570–582.
(111) Muggli, D. S.; McCue, J. T.; Falconer, J. L. Mechanism of the Photocatalytic Oxidation of Ethanol on TiO2. *J. Catal.* **1998**, *173*, 470–483.
(112) Piera, E.; Ayllón, J.; Doménech, X.; Peral, J. TiO2 Deactivation during Gas-Phase Photocatalytic Oxidation of Ethanol. *Catal. Today* **2002**, *76*, 259–270.
(113) Ohko, Y.; Tryk, D. A.; Hashimoto, K.; Fujishima, A. Autoxidation of Acetaldehyde Initiated by TiO2 Photocatalysis under Weak UV Illumination. *J. Phys. Chem. B* **1998**, *102* (15), 2699–2704.
(114) Sopyan, I.; Watanabe, M.; Murasawa, S.; Hashimoto, K.; Fujishima, A. An Efficient TiO2 Thin-Film Photocatalyst: Photocatalytic Properties in Gas-Phase Acetaldehyde Degradation. *J. Photochem. Photobiol. A Chem.* **1996**, *98*, 79–86.

(115) Hai, H.; Wen-jun, X.; Jian, Y.; Jim-wei, S.; Ming-xia, C.; Wen-feng, S. G. Preparations of TiO2 Film Coated on Foam Nickel Substrate by Sol-Gel Processes and Its Photocatalytic Activity for Degradation of Acetaldehyde. *J. Environ. Sci.* **2007**, *19*, 80–85.
(116) Xu, J.; Shiraishi, F. Photocatalytic Decomposition of Acetaldehyde in Air over Titanium Dioxide. *J. Chem. Technol. Biotechnol.* **1999**, *74*, 1096–1100.
(117) Falconer, J. L.; Magrini-bair, K. A. Photocatalytic and Thermal Catalytic Oxidation of Acetaldehyde on Pt/TiO2. *J. Catal.* **1998**, *179* (CA982215), 171–178.
(118) Iguchi, Y.; Ichiura, H.; Kitaoka, T.; Tanaka, H. Preparation and Characteristics of High Performance Paper Containing Titanium Dioxide Photocatalyst Supported on Inorganic Fiber Matrix. *Chemosphere* **2003**, *53*, 1193–1199.
(119) Hwang, S. J.; Raftery, D. In Situ Solid-State NMR Studies of Ethanol Photocatalysis: Characterization of Surface Sites and Their Reactivities. *Catal. Today* **1999**, *49*, 353–361.
(120) Vorontsov, A. V.; Savinov, E. N.; Barannik, G. B.; Troitsky, V. N.; Parmon, V. N. Quantitative Studies on the Heterogeneous Gas-Phase Photooxidation of CO and Simple VOCs by Air over TiO2. *Catal. Today* **1997**, *39*, 207–218.
(121) Nimlos, M. R.; Wolfrum, E. J.; Brewer, M. L.; Fennell, J. A.; Bintner, G. Gas-Phase Heterogeneous Photocatalytic Oxidation of Ethanol: Pathways and Kinetic Modeling. *Environ. Sci. Technol.* **1996**, *30* (10), 3102–3110.
(122) Melchers, S.; Schneider, J.; Emeline, A. V.; Bahnemann, D. W. Effect of H2O and O2 on the Adsorption and Degradation of Acetaldehyde on Anatase Surfaces - An In Situ ATR-FTIR Study. *Catalysts* **2018**, *8* (417), 1–12.
(123) Verbruggen, S. W.; Masschaele, K.; Moortgat, E.; Korany, T. E.; Hauchecorne, B.; Martens, A.; Lenaerts, S. Factors Driving the Activity of Commercial Titanium Dioxide Powders towards Gas Phase Photocatalytic Oxidation of Acetaldehyde. *Catal. Sci. Technol.* **2012**, *2*, 2311–2318.
(124) Sun, S.; Zhang, F. Insights into the Mechanism of Photocatalytic Degradation of Volatile Organic Compounds on TiO2 by Using In-Situ DRIFTS. In *Semiconductor Photocatalysis - Materials, Mechanisms and Applications*; 2016; pp 186–206.
(125) Coronado, J. M.; Kataoka, S.; Tejedor-Tejedor, I.; Anderson, M. A. Dynamic Phenomena during the Photocatalytic Oxidation of Ethanol and Acetone over Nanocrystalline TiO2: Simultaneous FTIR Analysis of Gas and Surface Species. *J. Catal.* **2003**, *219* (1), 219–230.
(126) Parashar, M.; Shukla, V. K.; Singh, R. Metal Oxides Nanoparticles via Sol–Gel Method: A Review on Synthesis, Characterization and Applications. *J. Mater. Sci. Mater. Electron.* **2020**, *31* (5), 3729–3749.
(127) Rathore, N.; Shukla, R. K.; Dubey, K. C.; Kulshreshtha, A. Synthesis of Undoped and Fe Doped Nanoparticles of TiO2via Co-Precipitation Technique and Their Characterizations. *Mater. Today Proc.* **2019**, *29*, 861–865.
(128) Morales, A. E.; Mora, E. S.; Pal, U. Use of Diffuse Reflectance Spectroscopy for Optical Characterization of Un-Supported Nanostructures. *Rev. Mex. física* **2007**, *53* (5), 18–22.

(129) Zoppi, A.; Lofrumento, C.; Castellucci, E. M.; Sciau, P. Al-for-Fe Substitution in Hematite: The Effect of Low Al Concentrations in the Raman Spectrum of Fe2O3. *J. Raman Spectrosc.* **2008**, *39*, 40–46.
(130) J. Kiss, J. R. Adsorption and Surface Reactions of Acetaldehyde on TiO2, CeO2 and Al2O3. *Appl. Catal. A Gen.* **2005**, *287*, 252–260.
(131) Rekoske, J. E.; Barteau, M. A. Competition between Acetaldehyde and Crotonaldehyde during Adsorption and Reaction on Anatase and Rutile Titanium Dioxide. *Langmuir* **1999**, *15*, 2061–2070.
(132) Singh, M.; Zhou, N.; Paul, D. K.; Klabunde, K. J. IR Spectral Evidence of Aldol Condensation: Acetaldehyde Adsorption over TiO2 Surface. *J. Catal.* **2008**, *260*, 371–379.
(133) Wu, W.; Yang, S.; Ho, C.; Lin, Y.; Liao, L.; Lin, J. Crotonaldehyde Formation from Decomposition of ICH2CH2OH on Powdered TiO2. *J. Phys. Chem. B* **2006**, *110*, 9627–9631.
(134) Tryba, B.; Rychtowski, P.; Srenscek-Nazzal, J.; Przepiorski, J. The Inflence of TiO2 Structure on the Complete Decomposition of Acetaldehyde Gas. *Mater. Res. Bull.* **2020**, *126* (110816), 1–10.
(135) Henych, J.; Stengl, V.; Mattsson, A.; Osterlund, L. In Situ FTIR Spectroscopy Study of the Photodegradation of Acetaldehyde and Azo Dye Photobleaching on Bismuth-Modified TiO2. *Photochem. Photobiol.* **2015**, *91*, 48–58.
(136) Sauce, S.; Vega-González, A.; Jia, Z.; Touchard, S.; Hassouni, K.; Kanaev, A.; Duten, X. New Insights in Understanding Plasma-Catalysis Reaction Pathways: Study of the Catalytic Ozonation of an Acetaldehyde Saturated Ag/TiO2/SiO2 Catalyst. *EPJ Appl. Phys.* **2015**, *71* (20805), 1–9.
(137) Shirai, K.; Fazio, G.; Sugimoto, T.; Selli, D.; Ferraro, L.; Watanabe, K.; Haruta, M.; Ohtani, B.; Kurata, H.; Di Valentin, C.; et al. Water-Assisted Hole Trapping at the Highly Curved Surface of Nano-TiO2 Photocatalyst. *J. Am. Chem. Soc.* **2018**, *140*, 1415–1422.
(138) Takeuchi, M.; Deguchi, J.; Sakai, S.; Anpo, M. Effect of H2O Vapor Addition on the Photocatalytic Oxidation of Ethanol, Acetaldehyde and Acetic Acid in the Gas Phase on TiO2 Semiconductor Powders. *Appl. Catal. B Environ.* **2010**, *96*, 218–223.

BIBLIOGRAPHY

Abidi, M.; Assadi, A. A.; Bouzaza, A.; Hajjaji, A.; Bessais, B.; Rtimi, S. Photocatalytic Indoor/Outdoor Air Treatment and Bacterial Inactivation on CuxO/TiO2 Prepared by HiPIMS on Polyester Cloth under Low Intensity Visible Light. Appl. Catal. B Environ. 2019, 259 (118074), 1–8.

Assadi, A. A.; Bouzaza, A.; Vallet, C.; Wolbert, D. Use of DBD Plasma, Photocatalysis, and Combined DBD Plasma/Photocatalysis in a Continuous Annular Reactor for Isovaleraldehyde Elimination – Synergetic Effect and Byproducts Identification. Chem. Eng. J. 2014, 254, 124–132.

Aymen Amine, A.; Bouzaza, A.; Soutrel, I.; Petit, P.; Medimagh, K.; Wolbert, D. A Study of Pollution Removal in Exhaust Gases from Animal Quartering Centers by Combining Photocatalysis with Surface Discharge Plasma: From Pilot to Industrial Scale. Chem. Eng. Process. Process Intensif. 2017, 111, 1–6.

Bae, E.; Choi, W.; Park, J.; Shin, H. S.; Kim, S. Bin; Lee, J. S. Effects of Surface Anchoring Groups (Carboxylate vs Phosphonate) in Ruthenium-Complex-Sensitized TiO2 on Visible Light Reactivity in Aqueous Suspensions. J. Phys. Chem. B 2004, 108 (37), 14093–14101.

Balbuena, J.; Carraro, G.; Cruz, M.; Gasparotto, A.; Maccato, C.; Pastor, A.; Sada, C.; Barreca, D.; Sanchez, L. Advances in Photocatalytic NOx Abatement through the Use of Fe2O3/TiO2 Nanocomposites. RSC Adv. 2016, 6, 74878–74885.

Bandara, J.; Mielczarski, J. A.; Kiwi, J. 1. Molecular Mechanism of Surface Recognition. Azo Dyes Degradation on Fe, Ti, and Al Oxides through Metal Sulfonate Complexes. Langmuir 1999, 15 (22), 7670–7679.

Bansal, P.; Verma, A. Applications of Sunlight Responsive Fe-Ag-TiO2 Composite Incorporating in-Situ Dual Effect for the Degradation of Pentoxifylline. Mater. Sci. Eng. B 2018, 236–237, 197–207.

Bauer, C.; Jacques, P.; Kalt, A. Investigation of the Interaction between a Sulfonated Azo Dye (AO7) and a TiO2 Surface. Chem. Phys. Lett. 1999, 307 (5–6), 397–406.

Benavides, J. A.; Trudeau, C. P.; Gerlein, L. F.; Cloutier, S. G. Laser Selective Photoactivation of Amorphous " 2 Films to Anatase and/or Rutile Crystalline Phases. ACS Appl. Energy Mater. 2018, 1 (8), 3607–3613.

Benniston, A. C.; Matousek, P.; McCulloch, I. E.; Parker, A. W.; Towrie, M. Detailed Picosecond Kerr-Gated Time-Resolved Resonance Raman Spectroscopy and Time-Resolved Emission Studies of Merocyanine 540 in Various Solvents. J. Phys. Chem. A 2003, 107 (22), 4347–4353.

Boeniger, M. F. Use of Ozone Generating Devices to Improve Indoor Air Quality. Am. Ind. Hyg. Assoc. J. 1995, 56 (6), 590–598.

Bourikas, K.; Stylidi, M.; Kondarides, D. I.; Verykios, X. E. Adsorption of Acid Orange 7 on the Surface of Titanium Dioxide. Langmuir 2005, 21 (20), 9222–9230.

Byrne, C.; Moran, L.; Hermosilla, D.; Merayo, N.; Blanco, Á.; Rhatigan, S.; Hinder, S.; Ganguly, P.; Nolan, M.; Pillai, S. C. Effect of Cu Doping on the Anatase-to-Rutile Phase Transition in TiO2 Photocatalysts: Theory and Experiments. Appl. Catal. B Environ. 2019, 246 (December 2018), 266–276.

Camacho-López, M. A.; Vargas, S.; Arroyo, R.; Haro-Poniatowski, E.; Rodríguez, R. Raman Studies on Laser Induced Crystallization of Co(II) Doped Titania; Effect of the Dopant Concentration. Opt. Mater. (Amst). 2002, 20 (1), 43–50.

Chatterjee, A.; Wu, S. B.; Chou, P. W.; Wong, M. S.; Cheng, C. L. Observation of Carbon-Facilitated Phase Transformation of Titanium Dioxide Forming Mixed-Phase Titania by Confocal Raman Microscopy. J. Raman Spectrosc. 2011, 42 (5), 1075–1080.

Clegg, I. M.; Everall, N. J.; King, B.; Melvin, H.; Norton, C. On-Line Analysis Using Raman Spectroscopy for Process Control during the Manufacture of Titanium Dioxide. Appl. Spectrosc. 2001, 55 (9), 1138–1150.

Coronado, J. M.; Kataoka, S.; Tejedor-Tejedor, I.; Anderson, M. A. Dynamic Phenomena during the Photocatalytic Oxidation of Ethanol and Acetone over Nanocrystalline TiO2: Simultaneous FTIR Analysis of Gas and Surface Species. J. Catal. 2003, 219 (1), 219–230.

Davamani, V.; Deepasri, M.; Parameswari, E.; Arulmani, S.; Sebastian, S. P.; Ilakia, T. Chemistry of Indoor Pollutants and Their Impacts on Human Health. Int. Res. J. Pure Appl. Chem. 2020, 21 (9), 40–61.

De Angelis, F.; Fantacci, S.; Mosconi, E.; Nazeeruddin, M. K.; Grätzel, M. Absorption Spectra and Excited State Energy Levels of the N719 Dye on TiO2 in Dye-Sensitized Solar Cell Models. J. Phys. Chem. C 2011, 115 (17), 8825–8831.

Escobedo, S.; Lasa, H. de. Photocatalysis for Air Treatment Processes: Current Technologies and Future Applications for the Removal of Organic Pollutants and Viruses. Catalysts 2020, 10 (9), 1–38.

Esmaeili, N.; Pirbazari, A. E.; Khodaee, Z. Visible-Light Active and Magnetically Recyclable Ag-Coated Fe3o4/Tio2 Nanocomposites for Efficient Photocatalytic Oxidation of 2,4-Dichlorophenol. Desalin. Water Treat. 2018, 114, 251–264.

Fakis, M.; Stathatos, E.; Tsigaridas, G.; Giannetas, V.; Persephonis, P. Femtosecond Decay and Electron Transfer Dynamics of the Organic Sensitizer D149 and Photovoltaic Performance in Quasi-Solid-State Dye-Sensitized Solar Cells. J. Phys. Chem. C 2011, 115 (27), 13429–13437.

Falconer, J. L.; Magrini-bair, K. A. Photocatalytic and Thermal Catalytic Oxidation of Acetaldehyde on Pt/TiO2. J. Catal. 1998, 179 (CA982215), 171–178.

Fujishima, A.; Zhang, X.; Tryk, D. A. TiO2 Photocatalysis and Related Surface Phenomena. Surf. Sci. Rep. 2008, 63 (12), 515–582.

Gaur, L. K.; Kumar, P.; Kushavah, D.; Khiangte, K. R.; Mathpal, M. C.; Agrahari, V.; Gairola, S. P.; Soler, M. A. G.; Swart, H. C.; Agarwal, A. Laser Induced Phase Transformation Influenced by Co Doping in TiO2 Nanoparticles. J. Alloys Compd. 2019, 780, 25–34.

Gierszewski, M.; Glinka, A.; Grądzka, I.; Gierczyk, B.; Ziółek, M. Testing New Concepts in Solar Cells Sensitized with Indoline Dyes - Alkoxysilyl Anchoring Group, Molecular Capping, and Cobalt-Based Electrolyte. J. Phys. Chem. C 2018, 122 (45), 25764–25775.

Gong, J.; Liang, J.; Sumathy, K. Review on Dye-Sensitized Solar Cells (DSSCs): Fundamental Concepts and Novel Materials. Renew. Sustain. Energy Rev. 2012, 16 (8), 5848–5860.

Gouadec, G.; Colomban, P. Raman Spectroscopy of Nanomaterials: How Spectra Relate to Disorder, Particle Size and Mechanical Properties. Prog. Cryst. Growth Charact. Mater. 2007, 53 (1), 1–56.
Grätzel, M. Solar Energy Conversion by Dye-Sensitized Photovoltaic Cells. Inorg. Chem. 2005, 44 (20), 6841–6851.
Greijer, H.; Lindgren, J.; Hagfeldt, A. Resonance Raman Scattering of a Dye-Sensitized Solar Cell: Mechanism of Thiocyanato Ligand Exchange. J. Phys. Chem. B 2001, 105 (27), 6314–6320.
Guo, Q.; Ma, Z.; Zhou, C.; Ren, Z.; Yang, X. Single Molecule Photocatalysis on TiO2 Surfaces. Chem. Rev. 2019, 119 (20), 11020–11041.
Guo, Q.; Zhou, C.; Ma, Z.; Yang, X. Fundamentals of TiO2 Photocatalysis: Concepts, Mechanisms, and Challenges. Adv. Mater. 2019, 31 (50), 1–26.
Hagfeldt, A.; Boschloo, G.; Sun, L.; Kloo, L.; Pettersson, H. Dye-Sensitized Solar Cells. Chem. Rev. 2010, 110 (11), 6595–6663.
Hai, H.; Wen-jun, X.; Jian, Y.; Jim-wei, S.; Ming-xia, C.; Wen-feng, S. G. Preparations of TiO2 Film Coated on Foam Nickel Substrate by Sol-Gel Processes and Its Photocatalytic Activity for Degradation of Acetaldehyde. J. Environ. Sci. 2007, 19, 80–85.
Hanaor, D. A. H.; Sorrell, C. C. Review of the Anatase to Rutile Phase Transformation. J. Mater. Sci. 2011, 46 (4), 855–874.
Hauchecorne, B.; Lenaerts, S. Unravelling the Mysteries of Gas Phase Photocatalytic Reaction Pathways by Studying the Catalyst Surface : A Literature Review of Different Fourier Transform Infrared Spectroscopic Reac. J. Photochem. Photobiol. C Photochem. Rev. 2013, 14, 72–85.
Hauchecorne, B.; Terrens, D.; Verbruggen, S.; Martens, J. A.; Langenhove, H. Van; Demeestere, K.; Lenaerts, S. Elucidating the Photocatalytic Degradation Pathway of Acetaldehyde: An FTIR in Situ Study under Atmospheric Conditions. Appl. Catal. B Environ. 2011, 106, 630–638.
Henderson, M. A. A Surface Science Perspective on TiO2 Photocatalysis. Surf. Sci. Rep. 2011, 66 (6–7), 185–297.
Henych, J.; Stengl, V.; Mattsson, A.; Osterlund, L. In Situ FTIR Spectroscopy Study of the Photodegradation of Acetaldehyde and Azo Dye Photobleaching on Bismuth-Modified TiO2. Photochem. Photobiol. 2015, 91, 48–58.
Hernández-Alonso, M. D.; Fresno, F.; Suárez, S.; Coronado, J. M. Development of Alternative Photocatalysts to TiO2: Challenges and Opportunities. Energy Environ. Sci. 2009, 2 (12), 1231–1257.
Hwang, S. J.; Raftery, D. In Situ Solid-State NMR Studies of Ethanol Photocatalysis: Characterization of Surface Sites and Their Reactivities. Catal. Today 1999, 49, 353–361.
Iguchi, Y.; Ichiura, H.; Kitaoka, T.; Tanaka, H. Preparation and Characteristics of High Performance Paper Containing Titanium Dioxide Photocatalyst Supported on Inorganic Fiber Matrix. Chemosphere 2003, 53, 1193–1199.
J. Kiss, J. R. Adsorption and Surface Reactions of Acetaldehyde on TiO2, CeO2 and Al2O3. Appl. Catal. A Gen. 2005, 287, 252–260.

Jiang, X.; Xu, W.; Yu, L. Photocatalytic Decomposition of Gaseous HCHO over Ag Modified TiO2 Nanosheets at Ambient Temperature. Nanomaterials 2019, 9 (338), 1–14.

Kafizas, A.; Carmalt, C. J.; Parkin, I. P. Does a Photocatalytic Synergy in an Anatase-Rutile TiO2 Composite Thin-Film Exist? Chem. - A Eur. J. 2012, 18 (41), 13048–13058.

Kapilashrami, M.; Zhang, Y.; Liu, Y. S.; Hagfeldt, A.; Guo, J. Probing the Optical Property and Electronic Structure of TiO2 Nanomaterials for Renewable Energy Applications. Chem. Rev. 2014, 114 (19), 9662–9707.

Kapilashrami, M.; Zhang, Y.; Liu, Y. S.; Hagfeldt, A.; Guo, J. Probing the Optical Property and Electronic Structure of TiO2nanomaterials for Renewable Energy Applications. Chem. Rev. 2014, 114 (19), 9662–9707.

Khazraji, A. C.; Hotchandani, S.; Das, S.; Kamat, P. V. Controlling Dye (Merocyanine-540) Aggregation on Nanostructured TiO2 Films. An Organized Assembly Approach for Enhancing the Efficiency of Photosensitization. J. Phys. Chem. B 1999, 103 (22), 4693–4700.

Kipreos, M. D.; Foster, M. Water Interactions on the Surface of 50 Nm Rutile TiO2 Nanoparticles Using in Situ DRIFTS. Surf. Sci. 2018, 677, 1–7.

Labadini, D.; Hafiz, S. S.; Huttunen, P. K.; Wolff, E. P.; Vasilakis, C.; Foster, M. Visualization and Quantification of the Laser-Induced ART of TiO2 by Photoexcitation of Adsorbed Dyes. Langmuir 2020, 36, 1651–1661.

Lee, H. Y.; Lan, W. L.; Tseng, T. Y.; Hsu, D.; Chang, Y. M.; Lin, J. G. Optical Control of Phase Transformation in Fe-Doped TiO2 Nanoparticles. Nanotechnology 2009, 20 (31), 1–5.

Lee, K. E.; Gomez, M. A.; Elouatik, S.; Demopoulos, G. P. Further Understanding of the Adsorption Mechanism of N719 Sensitizer on Anatase TiO2 Films for DSSC Applications Using Vibrational Spectroscopy and Confocal Raman Imaging. Langmuir 2010, 26 (12), 9575–9583.

Lin, H.; Ye, Q.; Deng, C.; Zhang, X. Field Analysis of Acetaldehyde in Mainstream Tobacco Smoke Using Solid-Phase Microextraction and a Portable Gas Chromatograph. J. Chromatogr. A 2008, 1198–1199, 34–37.

Liu, C.; Tong, R.; Xu, Z.; Kuang, Q.; Xie, Z.; Zheng, L. Efficiently Enhancing the Photocatalytic Activity of Faceted TiO2 Nanocrystals by Selectively Loading A-Fe2O3 and Pt Co-Catalysts†. RSC Adv. 2016, 6 (35), 29794–29801.

Liu, Y.; Xu, G.; Lv, H. Ag Modified Fe-Doping TiO2 Nanoparticles and Nanowires with Enhanced Photocatalytic Activities for Hydrogen Production and Volatile Organic Pollutant Degradation. J. Mater. Sci. Mater. Electron. 2018, 29, 10504–10516.

Long, H.; Yang, G.; Chen, A.; Li, Y.; Lu, P. Growth and Characteristics of Laser Deposited Anatase and Rutile TiO2 Films on Si Substrates. Thin Solid Films 2008, 517 (2), 745–749.

Luna, M. D. G. De; Laciste, M. T.; Tolosa, N. C.; Lu, M. Effect of Catalyst Calcination Temperature in the Visible Light Photocatalytic Oxidation of Gaseous Formaldehyde by Multi-Element Doped Titanium Dioxide. Environ. Sci. Pollut. Res. 2018, 25, 15216–15225.

Mamaghani, A. H.; Haghighat, F.; Lee, C. Photocatalytic Oxidation Technology for Indoor Environment Air Purification: The State-of-the-Art. Appl. Catal. B Environ. 2017, 203, 247–269.
Mathpal, M. C.; Tripathi, A. K.; Kumar, P.; Balasubramaniyan, R.; Singh, M. K.; Chung, J. S.; Hur, S. H.; Agarwal, A. Polymorphic Transformations and Optical Properties of Graphene-Based Ag-Doped Titania Nanostructures. Phys. Chem. Chem. Phys. 2014, 16 (43), 23874–23883.
Mathpal, M. C.; Tripathi, A. K.; Singh, M. K.; Gairola, S. P.; Pandey, S. N.; Agarwal, A. Effect of Annealing Temperature on Raman Spectra of TiO 2 Nanoparticles. Chem. Phys. Lett. 2013, 555, 182–186.
Matos, J.; Garcia, A.; Chovelon, J. M.; Ferronato, C. Combination of Adsorption on Activated Carbon and Oxidative Photocatalysis on TiO2 for Gaseous Toluene Remediation. Open Mater. Sci. J. 2010, 4, 23–25.
Maxime, G.; Amine, A. A.; Bouzaza, A.; Wolbert, D. Removal of Gas-Phase Ammonia and Hydrogen Sulfide Using Photocatalysis, Nonthermal Plasma, and Combined Plasma and Photocatalysis at Pilot Scale. Environ. Sci. Pollut. Res. 2014, 21, 13127–13137.
Mazza, T.; Barborini, E.; Piseri, P.; Milani, P.; Cattaneo, D.; Li Bassi, A.; Bottani, C. E.; Ducati, C. Raman Spectroscopy Characterization of TiO2 Rutile Nanocrystals. Phys. Rev. B - Condens. Matter Mater. Phys. 2007, 75 (4), 1–5.
Mbonyiryivuze, A. Titanium Dioxide Nanoparticles Biosynthesis for Dye Sensitized Solar Cells Application: Review. Phys. Mater. Chem. 2015, 3 (1).
Melchers, S.; Schneider, J.; Emeline, A. V.; Bahnemann, D. W. Effect of H2O and O2 on the Adsorption and Degradation of Acetaldehyde on Anatase Surfaces - An In Situ ATR-FTIR Study. Catalysts 2018, 8 (417), 1–12.
Melvin, A. A.; Illath, K.; Das, T.; Raja, T.; Bhattacharyya, S.; Gopinath, C. S. M-Au/TiO2 (M = Ag, Pd, and Pt) Nanophotocatalyst for Overall Solar Water Splitting: Role of Interfaces. Nanoscale 2015, 7 (32), 13477–13488.
Meng, A.; Zhang, L.; Cheng, B.; Yu, J. Dual Cocatalysts in TiO2 Photocatalysis. Adv. Mater. 2019, 31 (1807660), 1–31.
Merle, P.; Pascual, J.; Camassel, J.; Mathieu, H. Uniaxial-Stress Dependence of the First-Order Raman Spectrum of Rutile. I. Experiments. Phys. Rev. B 1980, 21 (4), 1617–1626.
Meroni, D.; Ardizzone, S.; Cappelletti, G.; Oliva, C.; Ceotto, M.; Poelman, D.; Poelman, H. Photocatalytic Removal of Ethanol and Acetaldehyde by N-Promoted TiO2 Films: The Role of the Different Nitrogen Sources. Catal. Today 2011, 161, 169–174.
Morales, A. E.; Mora, E. S.; Pal, U. Use of Diffuse Reflectance Spectroscopy for Optical Characterization of Un-Supported Nanostructures. Rev. Mex. física 2007, 53 (5), 18–22.
Mosquera, A. A.; Albella, J. M.; Navarro, V.; Bhattacharyya, D.; Endrino, J. L. Effect of Silver on the Phase Transition and Wettability of Titanium Oxide Films. Sci. Rep. 2016, 6 (July), 1–14.
Muggli, D. S.; McCue, J. T.; Falconer, J. L. Mechanism of the Photocatalytic Oxidation of Ethanol on TiO2. J. Catal. 1998, 173, 470–483.

Muñoz Tabares, J. A.; Anglada, M. J. Quantitative Analysis of Monoclinic Phase in 3Y-TZP by Raman Spectroscopy. J. Am. Ceram. Soc. 2010, 93 (6), 1790–1795.
Nakaruk, A.; Lin, C. Y.; Perera, D. S.; Sorrell, C. C. Effect of Annealing Temperature on Titania Thin Films Prepared by Spin Coating. J. Sol-Gel Sci. Technol. 2010, 55 (3), 328–334.
Nath, R. K.; Zain, M. F. M.; Jamil, M. An Environment-Friendly Solution for Indoor Air Puri Fi Cation by Using Renewable Photocatalysts in Concrete: A Review. Renew. Sustain. Energy Rev. 2016, 62, 1184–1194.
Nazeeruddin, M. K.; Humphry-Baker, R.; Liska, P.; Grätzel, M. Investigation of Sensitizer Adsorption and the Influence of Protons on Current and Voltage of a Dye-Sensitized Nanocrystalline TiO2 Solar Cell. J. Phys. Chem. B 2003, 107 (34), 8981–8987.
Nazeeruddin, M. K.; Zakeeruddin, S. M.; Humphry-Baker, R.; Jirousek, M.; Liska, P.; Vlachopoulos, N.; Shklover, V.; Fischer, C. H.; Grätzel, M. Acid-Base Equilibria of (2,2′-Bipyridyl-4,4′-Dicarboxylic Acid)Ruthenium(II) Complexes and the Effect of Protonation on Charge-Transfer Sensitization of Nanocrystalline Titania. Inorg. Chem. 1999, 38 (26), 6298–6305.
Ni, M.; Leung, M. K. H.; Leung, D. Y. C.; Sumathy, K. A Review and Recent Developments in Photocatalytic Water-Splitting Using TiO2 for Hydrogen Production. Renew. Sustain. Energy Rev. 2007, 11 (3), 401–425.
Nimlos, M. R.; Wolfrum, E. J.; Brewer, M. L.; Fennell, J. A.; Bintner, G. Gas-Phase Heterogeneous Photocatalytic Oxidation of Ethanol: Pathways and Kinetic Modeling. Environ. Sci. Technol. 1996, 30 (10), 3102–3110.
Novir, S. B.; Hashemianzadeh, S. M. Computational Study of New Azo Dyes with Different Anchoring Groups for Dye-Sensitised Solar Cells. Mol. Phys. 2016, 114 (5), 650–662.
O'Regan, B.; Grätzel, M. A Low-Cost, High-Efficiency Solar Cell Based on Dye-Sensitized Colloidal TiO2 Films. Nature 1991, 353, 737–739.
Obuchi, E.; Sakamoto, T.; Nakano, K. Photocatalytic Decomposition of Acetaldehyde over TiO2/SiO2 Catalyst. Chem. Eng. Sci. 1999, 54, 1525–1530.
Ohko, Y.; Tryk, D. A.; Hashimoto, K.; Fujishima, A. Autoxidation of Acetaldehyde Initiated by TiO2 Photocatalysis under Weak UV Illumination. J. Phys. Chem. B 1998, 102 (15), 2699–2704.
Ohtani, B. Photocatalysis A to Z-What We Know and What We Do Not Know in a Scientific Sense. J. Photochem. Photobiol. C Photochem. Rev. 2010, 11 (4), 157–178.
Oum, K.; Lohse, P. W.; Flender, O.; Klein, J. R.; Scholz, M.; Lenzer, T.; Du, J.; Oekermann, T. Ultrafast Dynamics of the Indoline Dye D149 on Electrodeposited ZnO and Sintered ZrO2 and TiO2 Thin Films. Phys. Chem. Chem. Phys. 2012, 14 (44), 15429–15437.
Parashar, M.; Shukla, V. K.; Singh, R. Metal Oxides Nanoparticles via Sol–Gel Method: A Review on Synthesis, Characterization and Applications. J. Mater. Sci. Mater. Electron. 2020, 31 (5), 3729–3749.
Parussulo, A. L. A.; Bonacin, J. A.; Toma, S. H.; Araki, K.; Toma, H. E. Unravelling the Chemical Morphology of a Mesoporous Titanium Dioxide Interface by Confocal Raman Microscopy: New Clues for Improving the Efficiency of Dye Solar Cells and Photocatalysts. Langmuir 2009, 25 (19), 11269–11271.

Parussulo, A. L. A.; Huila, M. F. G.; Araki, K.; Toma, H. E. N3-Dye-Induced Visible Laser Anatase-to-Rutile Phase Transition on Mesoporous TiO2 Films. Langmuir 2011, 27 (15), 9094–9099.
Pelaez, M.; Nolan, N. T.; Pillai, S. C.; Seery, M. K.; Falaras, P.; Kontos, A. G.; Dunlop, P. S. M.; Hamilton, J. W. J.; Byrne, J. A.; O'Shea, K.; et al. A Review on the Visible Light Active Titanium Dioxide Photocatalysts for Environmental Applications. Appl. Catal. B Environ. 2012, 125, 331–349.
Pérez León, C.; Kador, L.; Peng, B.; Thelakkat, M. Characterization of the Adsorption of Ru-Bpy Dyes on Mesoporous TiO2 Films with UV-Vis, Raman, and FTIR Spectroscopies. J. Phys. Chem. B 2006, 110 (17), 8723–8730.
Piera, E.; Ayllón, J.; Doménech, X.; Peral, J. TiO2 Deactivation during Gas-Phase Photocatalytic Oxidation of Ethanol. Catal. Today 2002, 76, 259–270.
Rathore, N.; Shukla, R. K.; Dubey, K. C.; Kulshreshtha, A. Synthesis of Undoped and Fe Doped Nanoparticles of TiO2via Co-Precipitation Technique and Their Characterizations. Mater. Today Proc. 2019, 29, 861–865.
Rekoske, J. E.; Barteau, M. A. Competition between Acetaldehyde and Crotonaldehyde during Adsorption and Reaction on Anatase and Rutile Titanium Dioxide. Langmuir 1999, 15, 2061–2070.
Ricci, P. C.; Carbonaro, C. M.; Stagi, L.; Salis, M.; Casu, A.; Enzo, S.; Delogu, F. Anatase-to-Rutile Phase Transition in TiO2 Nanoparticles Irradiated by Visible Light. J. Phys. Chem. C 2013, 117 (15), 7850–7857.
Ricci, P. C.; Casu, A.; Salis, M.; Corpino, R.; Anedda, A. Optically Controlled Phase Variation of TiO2 Nanoparticles. J. Phys. Chem. C 2010, 114 (34), 14441–14445.
Robertson, N. Optimizing Dyes for Dye-Sensitized Solar Cells. Angew. Chemie - Int. Ed. 2006, 45 (15), 2338–2345.
Sang, L.; Zhao, Y.; Burda, C. TiO 2 Nanoparticles as Functional Building Blocks. 2014.
Saqlain, S.; Cha, B. J.; Kim, S. Y.; Ahn, T. K.; Park, C.; Oh, J.-M.; Jeong, E. C.; Seo, H. O.; Kim, Y. D. Visible Light-Responsive Fe-Loaded TiO2 Photocatalysts for Total Oxidation of Acetaldehyde: Fundamental Studies towards Large-Scale Production and Applications. Appl. Surf. Sci. 2020, 505 (144160), 1–9.
Sauce, S.; Vega-González, A.; Jia, Z.; Touchard, S.; Hassouni, K.; Kanaev, A.; Duten, X. New Insights in Understanding Plasma-Catalysis Reaction Pathways: Study of the Catalytic Ozonation of an Acetaldehyde Saturated Ag/TiO2/SiO2 Catalyst. EPJ Appl. Phys. 2015, 71 (20805), 1–9.
Sauer, M. L.; Ollis, D. F. Photocatalyzed Oxidation of Ethanol and Acetaldehyde in Humidified Air. J. Catal. 1996, 158 (0055), 570–582.
Schneider, J.; Matsuoka, M.; Takeuchi, M.; Zhang, J.; Horiuchi, Y.; Anpo, M.; Bahnemann, D. W. Understanding TiO2 Photocatalysis : Mechanisms and Materials. Chem. Rev. 2014, 114 (2014 Titanium Dioxide Nanomaterials), 9919–9986.
Schneider, J.; Matsuoka, M.; Takeuchi, M.; Zhang, J.; Horiuchi, Y.; Anpo, M.; Bahnemann, D. W. Understanding TiO2photocatalysis: Mechanisms and Materials. Chem. Rev. 2014, 114 (19), 9919–9986.

Shirai, K.; Fazio, G.; Sugimoto, T.; Selli, D.; Ferraro, L.; Watanabe, K.; Haruta, M.; Ohtani, B.; Kurata, H.; Di Valentin, C.; et al. Water-Assisted Hole Trapping at the Highly Curved Surface of Nano-TiO2 Photocatalyst. J. Am. Chem. Soc. 2018, 140, 1415–1422.

Shuang, S.; Lv, R.; Xie, Z.; Zhang, Z. Surface Plasmon Enhanced Photocatalysis of Au/Pt-Decorated TiO2 Nanopillar Arrays. Sci. Rep. 2016, 6 (May), 1–8.

Singh, M.; Zhou, N.; Paul, D. K.; Klabunde, K. J. IR Spectral Evidence of Aldol Condensation: Acetaldehyde Adsorption over TiO2 Surface. J. Catal. 2008, 260, 371–379.

Sopyan, I.; Watanabe, M.; Murasawa, S.; Hashimoto, K.; Fujishima, A. An Efficient TiO2 Thin-Film Photocatalyst: Photocatalytic Properties in Gas-Phase Acetaldehyde Degradation. J. Photochem. Photobiol. A Chem. 1996, 98, 79–86.

Stagi, L.; Carbonaro, C. M.; Corpino, R.; Chiriu, D.; Ricci, P. C. Light Induced TiO2 Phase Transformation: Correlation with Luminescent Surface Defects. Phys. Status Solidi Basic Res. 2015, 252 (1), 124–129.

Stergiopoulos, T.; Bernard, M. C.; Hugot-Le Goff, A.; Falaras, P. Resonance Micro-Raman Spectrophotoelectrochemistry on Nanocrystalline TiO2 Thin Film Electrodes Sensitized by Ru(II) Complexes. Coord. Chem. Rev. 2004, 248 (13–14), 1407–1420.

Stylidi, M.; Kondarides, D. I.; Verykios, X. E. Pathways of Solar Light-Induced Photocatalytic Degradation of Azo Dyes in Aqueous TiO2 Suspensions. Appl. Catal. B Environ. 2003, 40 (4), 271–286.

Sun, S.; Zhang, F. Insights into the Mechanism of Photocatalytic Degradation of Volatile Organic Compounds on TiO2 by Using In-Situ DRIFTS. In Semiconductor Photocatalysis - Materials, Mechanisms and Applications; 2016; pp 186–206.

Sundius, T. Computer Fitting of Voigt Profiles to Raman Lines. Journal of Raman Spectroscopy. 1973, pp 471–488.

Suto, K.; Konno, A.; Kawata, Y.; Tasaka, S.; Sugita, A. Adsorption Dynamics of the N719 Dye on Nanoporous Titanium Oxides Studied by Resonance Raman Scattering and Fourier Transform Infrared Spectroscopy. Chem. Phys. Lett. 2012, 536, 45–49.

Tai, X. H.; Lai, C. W.; Juan, J. C.; Lee, K. M. Nano-Photocatalyst in Photocatalytic Oxidation Processes; 2020.

Takeuchi, M.; Deguchi, J.; Sakai, S.; Anpo, M. Effect of H2O Vapor Addition on the Photocatalytic Oxidation of Ethanol, Acetaldehyde and Acetic Acid in the Gas Phase on TiO2 Semiconductor Powders. Appl. Catal. B Environ. 2010, 96, 218–223.

Tanaka, A.; Nishino, Y.; Sakaguchi, S.; Yoshikawa, T.; Imamura, K.; Hashimoto, K.; Kominami, H. Functionalization of a Plasmonic Au/TiO2 Photocatalyst with an Ag Co-Catalyst for Quantitative Reduction of Nitrobenzene to Aniline in 2-Propanol Suspensions under Irradiation of Visible Light. Chem. Commun. 2013, 49 (25), 2551–2553.

Thomas, S.; Mamour Sakho, E. H.; Kalarikkal, N.; Oluwafemi, O. S.; Wu, J. Nanomaterials for Solar Cell Applications; Elsevier: San Diego, UNITED STATES, 2019.

Thompson, T. L.; Yates, J. T. Surface Science Studies of the Photoactivation of TiO2 - New Photochemical Processes. Chem. Rev. 2006, 106 (10), 4428–4453.

Tripathi, A. K.; Singh, M. K.; Mathpal, M. C.; Mishra, S. K.; Agarwal, A. Study of Structural Transformation in TiO2 Nanoparticles and Its Optical Properties. J. Alloys Compd. 2013, 549, 114–120.

Tryba, B.; Rychtowski, P.; Srenscek-Nazzal, J.; Przepiorski, J. The Inflence of TiO2 Structure on the Complete Decomposition of Acetaldehyde Gas. Mater. Res. Bull. 2020, 126 (110816), 1–10.

Ubolchonlakate, K.; Sikong, L.; Tontai, T. Formaldehyde Degradation by Photocatalytic Ag-Doped TiO2 Film of Glass Fiber Roving. J. Nanosci. Nanotechnol. 2010, 10, 7522–7525.

Vásquez, G. C.; Peche-Herrero, M. A.; Maestre, D.; Gianoncelli, A.; Ramírez-Castellanos, J.; Cremades, A.; González-Calbet, J. M.; Piqueras, J. Laser-Induced Anatase-to-Rutile Transition in TiO2 Nanoparticles: Promotion and Inhibition Effects by Fe and Al Doping and Achievement of Micropatterning. J. Phys. Chem. C 2015, 119 (21), 11965–11974.

Verbruggen, S. W.; Masschaele, K.; Moortgat, E.; Korany, T. E.; Hauchecorne, B.; Martens, A.; Lenaerts, S. Factors Driving the Activity of Commercial Titanium Dioxide Powders towards Gas Phase Photocatalytic Oxidation of Acetaldehyde. Catal. Sci. Technol. 2012, 2, 2311–2318.

Vorontsov, A. V.; Savinov, E. N.; Barannik, G. B.; Troitsky, V. N.; Parmon, V. N. Quantitative Studies on the Heterogeneous Gas-Phase Photooxidation of CO and Simple VOCs by Air over TiO2. Catal. Today 1997, 39, 207–218.

Wang, F.; Jiang, Y.; Lawes, D. J.; Ball, G. E.; Zhou, C.; Liu, Z.; Amal, R. Analysis of the Promoted Activity and Molecular Mechanism of Hydrogen Production over Fine Au-Pt Alloyed TiO2 Photocatalysts. ACS Catalysis. 2015, pp 3924–3931.

Wang, M.; Lawal, A.; Stephenson, P.; Sidders, J.; Ramshaw, C. Post-Combustion CO2 Capture with Chemical Absorption: A State-of-the-Art Review. Chem. Eng. Res. Des. 2011, 89, 1609–1624.

Wen, J.; Li, X.; Liu, W.; Fang, Y.; Xie, J.; Xu, Y. Photocatalysis Fundamentals and Surface Modification of TiO 2 Nanomaterials. Chinese J. Catal. 2015, 36 (12), 2049–2070.

Weon, S.; He, F.; Choi, W. Status and Challenges in Photocatalytic Nanotechnology for Cleaning Air Polluted with Volatile Organic Compounds: Visible Light Utilization and Catalyst Deactivation. Environ. Sci. Nano 2019, 6 (11), 3185–3214.

Wu, W.; Yang, S.; Ho, C.; Lin, Y.; Liao, L.; Lin, J. Crotonaldehyde Formation from Decomposition of ICH2CH2OH on Powdered TiO2. J. Phys. Chem. B 2006, 110, 9627–9631.

Xu, J.; Shiraishi, F. Photocatalytic Decomposition of Acetaldehyde in Air over Titanium Dioxide. J. Chem. Technol. Biotechnol. 1999, 74, 1096–1100.

Zanatta, A. R. A Fast-Reliable Methodology to Estimate the Concentration of Rutile or Anatase Phases of TiO2. AIP Adv. 2017, 7 (7).

Zhang, J.; Li, M.; Feng, Z.; Chen, J.; Li, C. UV Raman Spectroscopic Study on TiO2. I. Phase Transformation at the Surface and in the Bulk. J. Phys. Chem. B 2006, 110 (2), 927–935.

Zhang, W. F.; He, Y. L.; Zhang, M. S.; Yin, Z.; Chen, Q. Raman Scattering Study on Anatase TiO2 Nanocrystals. J. Phys. D. Appl. Phys. 2000, 33 (8), 912–916.

Zhang, Y.; Harris, C. X.; Wallenmeyer, P.; Murowchick, J.; Chen, X. Asymmetric Lattice Vibrational Characteristics of Rutile TiO2 as Revealed by Laser Power Dependent Raman Spectroscopy. J. Phys. Chem. C 2013, 117 (45), 24015–24022.
Zhang, Y.; Wu, W.; Zhang, K.; Liu, C.; Yu, A.; Peng, M.; Zhai, J. Raman Study of 2D Anatase TiO2 Nanosheets. Phys. Chem. Chem. Phys. 2016, 18 (47), 32178–32184.
Zhao, H. C.; Harney, J. P.; Huang, Y.-T.; Yum, J.-H.; Nazeeruddin, M. K.; Grätzel, M.; Tsai, M.-K.; Rochford, J. Evaluation of a Ruthenium Oxyquinolate Architecture for Dye-Sensitized Solar Cells. Inorg. Chem. 2012, 51 (1), 1–3.
Zhao, L.; Han, M.; Lian, J. Photocatalytic Activity of TiO2 Films with Mixed Anatase and Rutile Structures Prepared by Pulsed Laser Deposition. Thin Solid Films 2008, 516 (10), 3394–3398.
Zhao, Y.; Tao, C.; Xiao, G.; Wei, G.; Li, L.; Liu, C.; Su, H. Controlled Synthesis and Photocatalysis of Sea Urchin-like Fe3O4@TiO2@Ag Nanocomposites. Nanoscale 2016, 8 (9), 5313–5326.
Zoppi, A.; Lofrumento, C.; Castellucci, E. M.; Sciau, P. Al-for-Fe Substitution in Hematite: The Effect of Low Al Concentrations in the Raman Spectrum of Fe2O3. J. Raman Spectrosc. 2008, 39, 40–46.